Development of processing conditions for organic photovoltaic devices

A thesis for the degree of

Doctor of Philosophy

at the University of Warwick

by

Natalie Kate Unsworth

Supervised by Prof. Tim S. Jones

Department of Chemistry

University of Warwick, Coventry

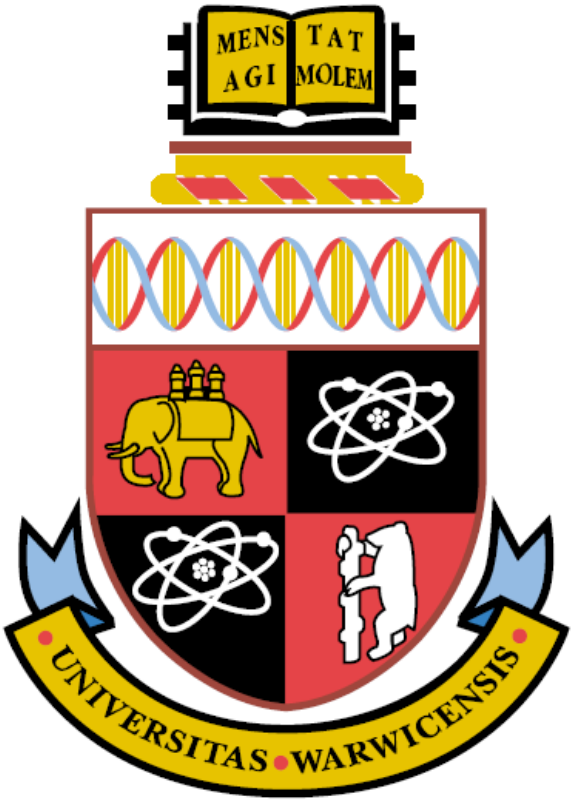

May 2015

Abstract

Organic photovoltaic (OPV) devices are attracting significant attention as an alternative renewable energy source. Recent advancements have led to an increase in device efficiency and stability; however a greater focus on reducing material and processing costs is needed. This thesis sets out to consider these issues.

Indium-tin oxide (ITO) is widely believed to be a major contributor towards the material cost of the device. Highly conductive poly(3,4-ethylenedioxythiophene):poly(styrenesulfonate) (PEDOT:PSS) was investigated as an alternative and inexpensive transparent conducting electrode (TCE). The intrinsic conductivity of the PEDOT:PSS films was improved by dimethyl sulfoxide (DMSO) treatments. Ultra-violet absorption spectroscopy (UV-Vis), X-ray photoelectron spectroscopy (XPS) and conductive atomic force microscopy (CAFM) were used to gain understanding as to how the different treatments improved the film conductivity and how this influenced OPV device performance. This study highlighted the possibility of using PEDOT:PSS as an alternative electrode and emphasised the importance of optimising and tailoring the electrode to the specific photoactive layer.

Careful control over processing conditions has widely contributed to the development of OPV devices. However, although inert atmospheres and casting from halogenated solvents results in high efficiencies, they also further add to the processing costs. A method to process the poly(3-hexylthiophene):phenyl-C61-butyric acid methyl ester (P3HT:PCBM) photoactive layer under ambient conditions was developed, which was found to be applicable on both ITO and PEDOT:PSS electrodes. This methodology was then used to process inverted P3HT:PCBM devices spin cast out of non-halogenated solvents which gave comparable overall device performance to those cast out of dichlorobenzene (DCB). This indicates the potential of producing low-cost OPV devices processed using more environmentally friendly solvents and under an ambient environment which can be more easily incorporated in a roll-to-roll process.

Table of contents

Declaration

This thesis is submitted to the University of Warwick in support of my application for the degree of Doctor of Philosophy. It has been composed by myself and has not been submitted in any previous application for any degree.

The work presented here was carried out by the author except for the XPS measurements that were obtained by Dr Marc Walker in the Department of Physics, The University of Warwick. The sample preparation, analysis and interpretation were performed by the author.

Acknowledgements

Firstly, I would like to thank my supervisor Professor Tim Jones for giving me the opportunity to carry out research in the field of organic photovoltaic devices and the chance to present my work internationally. I would also like to thank all the members of staff in the Department of Chemistry at the University of Warwick for all their assistance. Also, I would like to thank the Engineering and Physical Sciences Research Council (EPSRC) and Paintbox Limited for the project funding. Special thanks go to James Sharp and Bob Lilley for the informative and insightful discussions throughout my PhD.

I would like to acknowledge all members of the Tim Jones group, past and present, who have made the last four years a hugely memorable time. So my thanks go to Mark, Paul, Edd, Jay, Ian, Tom, Nicola, Luke, Dawn, Raff, Tomasz, Stefan and Ricky (you will be missed) for all the help and advice you have given me no matter how big or small it may have seemed to you. I would especially like to thank Ian and Paul for reading through my thesis. A special mention goes to Chloe and Gavin. Four years is a long time, but it seems like only yesterday we started our PhDs together. Thank you for sharing this (at times trying!) journey with me. I wish you luck in your new careers.

My thanks go to all my friends both during my Undergrad, Tasmania and PhD. Special thanks, Chloe, Nic, Sam and Jon for keeping me (semi) sane and (reasonably) calm the over the last four years. Chloe – thank you for all the patience you have shown me, listening to me and attempting to teach me to cook, just to

mention a few reasons. Nic – thank you for putting up with me all these years and letting me take over your house far too often. To my Cov family – thank you for keeping me together, eating far too many chocolate Bourbons and watching rubbish TV with me, I will definitely miss you when I leave.

Finally I thank my family for all their love and support over the years. To my parents who have sat and listened to me while having absolutely no idea what I am going on about! Suzie – again thank you for listening to me and also for giving me a project to plan and look forward to each year. Even though you then have to deal with me over obsessively preparing for it. We need to start sorting the next one out!

List of publications

Publications:

- **N. K. Unsworth**, I. Hancox, C. Argent Dearden, T. Howells, P. Sullivan, R.S. Lilley, J. Sharp and T.S. Jones, Applied Physics Letters, 2013, 103, 173304, *Highly conductive spray deposited poly(3,4-ethylenedioxythiophene):poly (styrenesulfonate) electrodes for indium tin oxide-free small molecule organic photovoltaic devices*.
- C. Argent Dearden, M. Walker, N. Beaumont, I. Hancox, **N. K. Unsworth**, P. Sullivan, C. F. McConville, T. S. Jones, *Phys. Chem. Chem. Phys.*, 2014, 16**,** 18926-18932, *High Voltage Hybrid Organic Photovoltaics using a Zinc Oxide Acceptor.*
- **N. K. Unsworth**, I. Hancox, C. Argent Dearden, P. Sullivan, M. Walker, R. S. Lilley, J. Sharp, T.S. Jones. Organic Electronics 15, 2014, 2624 – 2631, *Comparison of dimethyl sulfoxide treated highly conductive poly(3,4-ethylenedioxythiophene):poly(styrenesulfonate) electrodes for use in indium tin oxide-free organic electronic photovoltaic devices*

Presentations:

- *Paintbox Industrial Sponsor Meetings*, University of Warwick and Banbury, UK, 2010 – 2014 (presentations)
- *Frontiers in Organic, Dye-sensitized and Hybrid Solar Cells*, Krutyn, Poland, June 2011 (poster)
- *Organext 'Photovoltaics at the nanoscale'*, Hasselt University, Belgium, October 2011 (poster)
- *Postgraduate Symposium*, University of Warwick, UK, May 2012 (poster)
- *The MRS Fall Meeting and Exhibit*, Boston, USA, November 2012 (poster)
- *Monash-Warwick Symposium*, University of Warwick, UK, February 2013 (presentation)
- *Postgraduate Symposium*, University of Warwick, UK, May 2013 (presentation)
- *Next-Generation Organic Photovoltaics*, Groningen, The Netherlands, June 2013, (poster)
- *11th International Conference on Materials Chemistry*, University of Warwick, UK, July 2013 (Poster)

Abbreviations

General Abbreviations

AFM	Atomic force microscopy
AM	Air mass
AO	Atomic orbital
BE	Binding energy
BHJ	Bulk heterojunction
CAFM	Conductive atomic force microscopy
CB	Conduction band
CPD	Contact potential difference
CT	Charge transfer
D/A	Donor/acceptor
DSSC	Dye-sensitised solar cell
EEL	Electron extracting layer
EQE	External quantum efficiency
HOMO	Highest occupied molecular orbital
HTL	Hole transport layer
ICP	Intrinsically conducting polymer
ICT	Integer Charge Transfer
ITO	Indium-tin oxide
KP	Kelvin Probe
LUMO	Lowest unoccupied molecular orbital
MO	Molecular orbital
OLED	Organic light emitting diodes

OMBD	Organic molecular beam deposition
OPV	Organic photovoltaics
OSC	Organic semiconductor
PCE	Power conversion efficiency
PV	Photovoltaic
QCM	Quartz crystal microbalance
RMS	Rough mean squared
SAM	Self Assembled Monolayer
TCE	Transparent conductive electrode
TMO	Transition metal oxide
TW	Terawatts
UV	Ultra-violet
VB	Valence band
XPS	X-ray photoelectron spectroscopy

Symbols/Notations

Φ	Work function
A	Absorbance
α	Absorption coefficient
b	Path length
BE	Binding energy
c	Concentration
D	Diffusion coefficient
ε	Dielectric constant
ε_λ	Molar extinction coefficient

E_b	External backing potential
E (λ,T)	Irradience
E_{EA}	Electron affinity
E_b	Incident electron beam
E_F	Fermi level energy
E_g	Energy gap
E_{IP}	Ionisation potential
E_{KB}	Kinetic energy of electron
E_{Vac}	Vacuum level
ΔE	Energy gap
FF	Fill factor
γ_{lv}	liquid-vapour interfacial tension
γ_{sl}	solid-liquid interfacial free energy
γ_{sv}	solid-vapour interfacial free energy
h	Planck's constant
I	Attenuated light
I_b	Electron beam current
I_0	Incident light intensity
I_g	Interface gap
J-V	Current density-voltage
k	Extinction coefficient
k	Boltzmann's constant
l	Film thickness

L_D	Exciton diffusion length
n	Refractive index
J_{SC}	Short circuit current density
P_{inc}	Incident optical power density
P_m	Maximum power point
q	Electron charge
R_L	Load resistance
R_s	Series resistance
R_{sh}	Shunt resistance
rr	Regio-regular
τ	Exciton lifetime
T	Temperature
ν	Frequency of radiation (Hz)
V_{OC}	Open circuit voltage
λ	Wavelength
Ω sq^{-1}	Ohms per square
θ	Angle of incidence
η	Efficiency
η_A	Quantum efficiency of Absorption of Incident Photon
η_{ED}	Quantum efficiency of Exciton Diffusion
η_{CT}	Quantum efficiency of Exciton Dissociation
η_{CC}	Quantum efficiency of Charge Collection

Chemical Compounds

Ag	Silver
Al	Aluminium
BCP	Bathocuproine
C_{60}	Buckminster-Fullerene
CdTe	Cadmium telluride
CN-PPV	cyano-polyphenylene vinylene
CuPc	Copper phthalocyanine
GaAs	Gallium arsenide
H_2	Hydrogen
H_2Pc	Metal free phthalocyanine
H_2SO_4	Sulfuric acid
InO	Indium oxide
IPA	Isopropyl alcohol
ITO	Indium tin oxide
MDMO-PPV	Poly[2-methoxu-5-(3'7'-dimethyloctyloxy)-1,4-phenylene-vinylene)
MEH-PPV	Poly(2-methoxy-5-(2'-ethyl-hexyloxy)-1,4-phenylene vinylene
MoO_x	Molybdenum oxide
N_2	Nitrgoen
P3HT	Poly(3-hexylthiophene)
PCBM	Phenyl-C61-butyric acid methyl ester
Pcs	Phthalocyanine
PCPDTBT	poly[2,6-(4,4-bis-(2-ethylhexyl)-4*H*-cyclopenta [2,1-*b*;3,4-*b'*]dithiophene)-*alt*-4,7(2,1,3-benzothiadiazole)]

PEDOT:PPS	Poly(3,4-ethylenedioxythiophene):poly(styrenesulfonate)
PEI	Branched polyethylenimine
PTCBI	3,4,9,10-perylenetetracarboxylic bis-benzimidazole
SubPc	Boron Subphthalocyanine
ZnO	Zinc oxide

Chapter 1. Introduction

This chapter presents an overview of the increased global energy demand and the need for alternative energies to fossil fuels. The benefits of photovoltaic (PV) devices are described before a brief review of the history of organic photovoltaics (OPV) devices is given. A significant part of this thesis focuses on processing bulk heterojuction (BHJ) devices and so particular emphasis is given to the development of these devices and the factors that affect the device performance. Next follows a section on semiconductor theory, followed by the principles of device operation and then the materials used in this work are discussed. Since major part of this thesis concentrates on using poly(3,4-ethylenedioxythiophene):poly(styrenesulfonate) (PEDOT:PSS) as an alternative electrode to indium tin-oxide (ITO), a review on the development of the polymer is included. This section concludes with an outline of the other chapters in this thesis.

1.1 Overview

1.1.1 The need for renewable energy

Global energy consumption is forecast to rise by 41 % between 2012 and 2035 due to the predicted expansion in global population and increased demand from emerging economies, particularly China, India and the Middle East. Currently fossil fuels are almost entirely responsible for meeting the global energy demand as shown in **Figure 1.1**.[1] There are, however, several issues with using fossil fuels. They are a finite resource with uneven distribution across the globe is unbalanced which leads to concerns over energy security. The impact fossil fuels have on the environment is also a major concern. Burning fossil fuels is accompanied by the release of carbon dioxide (CO_2) and other greenhouse gases which are thought to contribute towards global warming. Despite numerous climate change mitigation policies, annual greenhouse gas emissions increased by 2.2 % per year from 2000 – 2010 compared to 1.3 % from 1970 – 2000.[2] The global mean surface temperature is expected to keep increasing unless significant further efforts are made to reduce greenhouse gas emissions. It is now becoming increasing unlikely that efforts to keep the temperature rise to below 2 ^{o}C relative to pre-industrial levels will be effective.

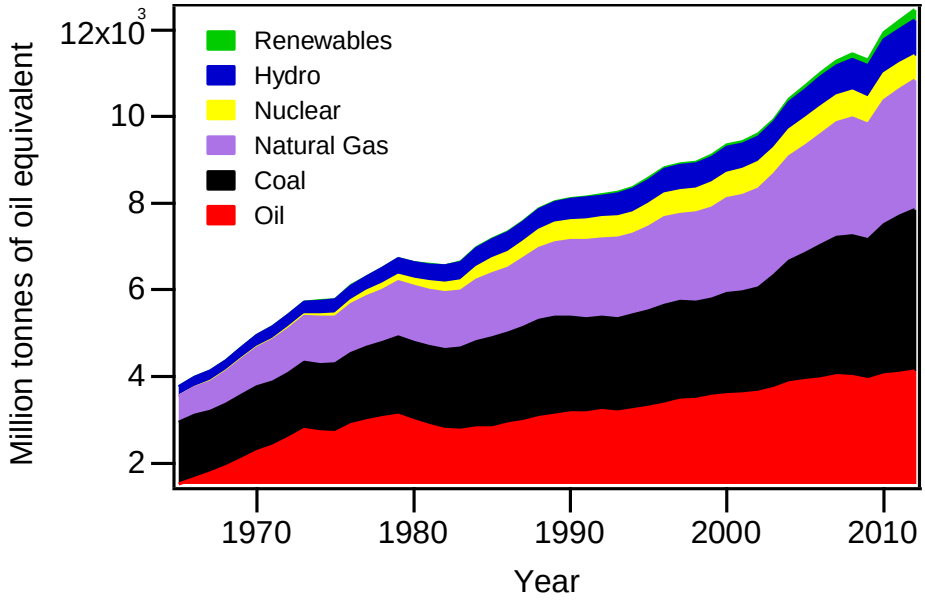

Figure 1.1 – World primary energy consumption of million tonnes of oil equivalent per year. Data taken from BP statistical review of World Energy 2013.[3]

There is a need to find cleaner energy sources that can be implemented on both a local and global scale so that the predicted demand for more energy is met while also taking the environmental concerns into consideration. Renewable energy technologies have great potential, but like all major energy sources they also have various drawbacks. Many renewable energy sources such as wind and solar are variable and intermittent and therefore are difficult to integrate into an electrical grid at any reasonable scale. There are also financial concerns as to whether renewable energy sources will continue to be viable once subsidies become restricted.[4] Despite these concerns renewable energies are expected to contribute to nearly half the increase in global power generation up to 2035 with wind and solar photovoltaics (PV) are expected to contributing 45 % to this expansion.[5] Solar is a particularly attractive energy source; more energy from the sun reaches the earth in one hour than

the energy consumed on the entire planet in 2001.[6] PV devices have the ability to be used in off grid areas, and to be incorporated into new and exsisting buildings. However, PV technology still has some way to go before becoming recognised as a sustainable power source. Currently in the US, PV devices only contribute to 0.3 % of the total energy generated.[7] The situation is slightly better in Germany where PV devices contribute to over 5 % of the gross electric consumption in Germany.[8] The main challenge facing PV technology is considerably reducing the cost per watt to compete with fossil fuel alternatives. Solar energy is diffuse, so in order to make this technology economically viable material costs must be extremely low.

1.1.2 History of photovoltaic devices

Despite Becquerel discovering the photovoltaic effect in 1839,[9] it was not until much later in the 1940s that the modern PV device was first developed by Ohl.[10] The progress of PV devices were further advanced due to extensive work by the Bell labs in the 1950s and it was not long before p-n doped highly crystalline devices were used in satellites.[11, 12] Today, monocrystalline silicon PV devices have reached efficiencies of over 25 %. However, they are not ideal for general commercial applications due to the high energy demands and the large fabrication costs involved in producing defect free crystals.[13] Polycrystalline and amorphous silicon PV devices are less expensive but also have lower efficiencies of around 10 %.[13]

Other inorganic PV devices are based on thin films consisting of a combination of group III and V elements. GaAs and CdTe devices have reached efficiencies of over 28 % and 19 % respectively.[13] Careful control over growth conditions enables

tailoring to different parts of the solar spectrum. A multijunction PV can be tuned to the wavelength of light it collects which results in efficiencies that are higher than single junction devices.[14] The highest efficiencies for multijunction devices are now above 37 %.[13] There are several drawbacks to this type of PV device including the low abundance and concerns over toxicity over some of the elements used.[15]

Organic semiconductors (OSCs) are attracting increased interest as a result of their synthetic variability, cheaper production, and the potential to producing light weight, flexible and easily manufactured PV devices. There are several categories of these devices including dye-sensitised solar cells (DSSC), hybrid organic-inorganic, small molecule and polymer PV devices. The efficiencies of these types of devices are lower than for a conventional silicon device but their low temperature processing and hence low manufacturing costs are hoped to counteract this. The rest of this section will focus solely on small molecule and polymer PV devices and these will be referred to as OPV devices. **Figure 1.2** shows a summary of the different PV device types mentioned and their accredited efficiencies since 1976.

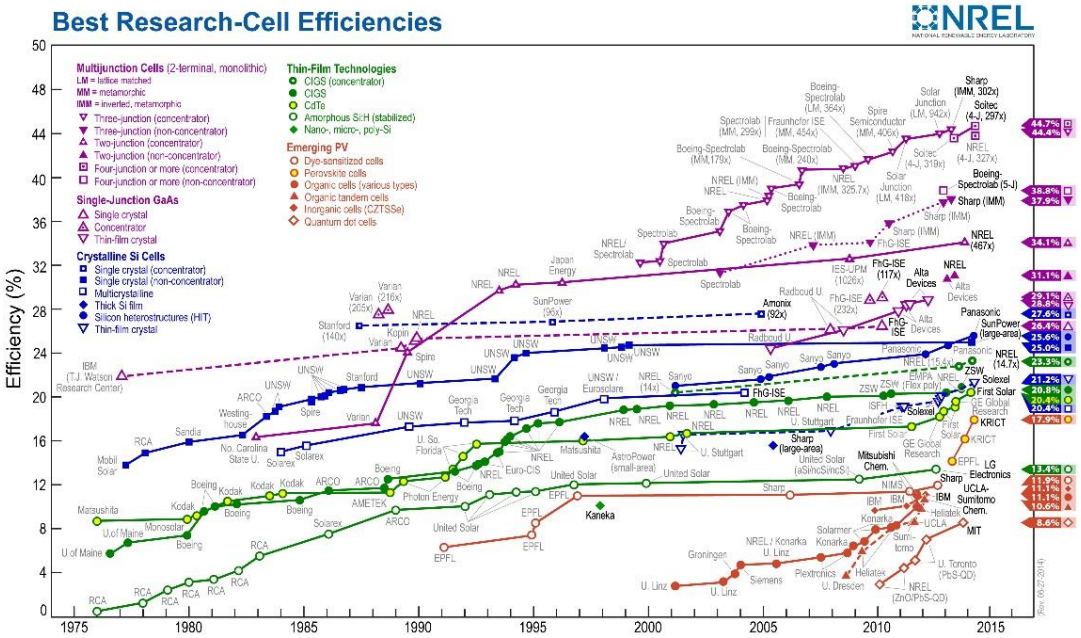

Figure 1.2 – Development of different types of PV devices from 1976 to 2014.[16]

1.1.3 History of organic photovoltaic devices

The first OPV devices were made in 1959 and comprised of a single photoactive layer of anthracene.[17] For the next few decades OPV devices consisted of a single organic layer sandwich between two electrodes of different work functions. Exciton dissociation mainly occurred in the depletion region close to electrode or at trap sites within the organic layer. This poor dissociation, alongside high recombination rates of holes and electrons, resulted in low efficiencies of ~ 0.1 %.[18]

It was not until 1986 that there was a significant breakthrough, when Tang developed a donor/acceptor (D/A) bilayer OPV device.[19] The novel device comprised two thermally evaporated semiconductors - copper phthalocyanine (CuPc) as the electron donating material and 3,4,9,10-perylenetetracarboxylic bis-benzimidazole (PTCBI)

as the electron acceptor material – which achieved a power conversion efficiency (PCE) of ~ 1 %. The interface offset between the donor and acceptor materials allowed for more effective exciton dissociation, improved charge transport and therefore decreased recombination. This concept of donor/acceptor devices has been widely exploited ever since.

A notable improvement for bilayer devices came with the use of C_{60}, discovered in 1985,[20] as an electron acceptor. The longer diffusion length of C_{60} was attributed to devices achieving a PCE of 3.6 %.[21] While C_{60} is mainly used as the electron accepting material (although efforts are being made to replace it),[22] many different materials have been used as the electron donating material including other phthalocyanines and oligoacenes.[23-25]

The bilayer OPV device structure is still widely employed but this architecture has some disadvantages. Exciton dissociation is most effective at the D/A interface. The exciton, therefore, should ideally be formed within an exciton diffusion length (L_D) of the interface. Generally, for OSC the L_D is in the 10 nm range. However, in order to absorb enough light the film thickness for most OSC needs to be over 100 nm, therefore only a small amount of excitons generated are able to reach the interface and dissociate. Several device architectures have been introduced to improve exciton dissociation and absorption.

Tandem devices were first introduced in 1990 by Hiramoto.[26] In this device structure two or more devices, separated by a thin recombination layer, are stacked on top of each other. The tandem device is usually designed so that the individual devices absorb in different parts of the solar spectrum and the thickness of the OSC

is matched to the L_D of the material. This allows for higher efficiencies due to the greater absorption. Additionally, the device open circuit voltage (V_{oc}) is a summation of the individual devices which further improves the PCE. In 2013 Heliatek announced a tandem device with a certified efficiency of ~ 12 %.[27]

Another way to enhance exciton dissociation and maintain a thick enough film for high absorption is to codeposit (thermally evaporated small molecules) or blend (solution processed polymers) donor and acceptor materials to produce an intermixed D/A film. This intermixing results in a larger donor and acceptor material interface so that the exciton is more likely to be with in a L_D of the heterojunction. Initial work on small molecule codeposited device structures was carried out in the early 1990s by Hiramoto.[28, 29] Soon after, in 1995, the first solution processed polymer:fullerene bulk heterojunction (BHJ) devices were reported.[30, 31] The device was comprised of a poly(2-methoxy-5-(2'-ethyl-hexyloxy)-(1,4-phenylene vinylene (MEH-PPV) donor and a soluble C_{60} derivative phenyl-C_{61}-butyric acid methyl ester (PCBM) or cyano-polyphenylene vinylene (CN-PPV) acceptor. The donor and acceptor were blended together and spin coated on to an indium-tin oxide (ITO) electrode. The rest of this section will focus on polymer:fullerene BHJ devices. **Figure 1.3** shows the structures for bilayer, tandem and BHJ devices.

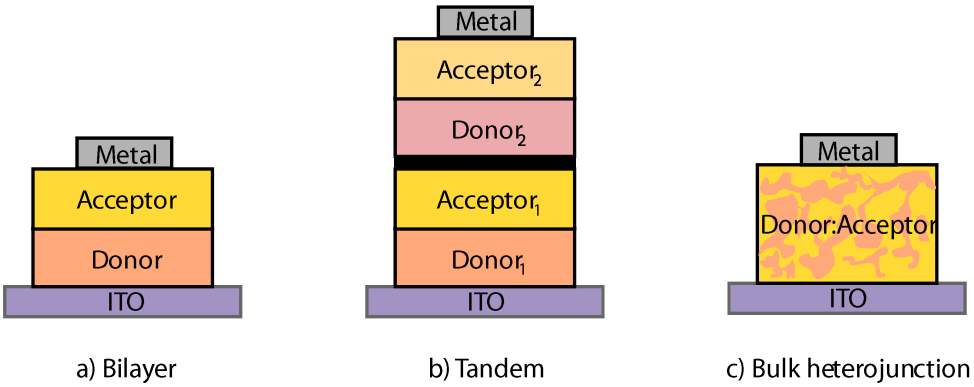

Figure 1.3 – Schematics of a) a bilayer, b) tandem and c) BHJ device.

Significant developments in the understanding of BHJ have led to a huge improvement in the PCE, some of which now have now exceeded 11 %.[32, 33] The performance of BHJ devices is heavily reliant on the morphology of the polymer donor:acceptor photoactive layer. Ideally, the morphology should be a bi-continuous interpenetrating network of polymer and acceptor components. The interfacial area should be maximised so that domains of each component are within an L_D to allow maximum excitions to dissociate efficiently. Additionally, there needs to be continuous polymer and acceptor pathways to the respective electrodes to ensure efficient charge transport of holes and electrons. A non-optimised microstructure, as shown in **Figure 1.4**, has a severe negative impact the device performance.

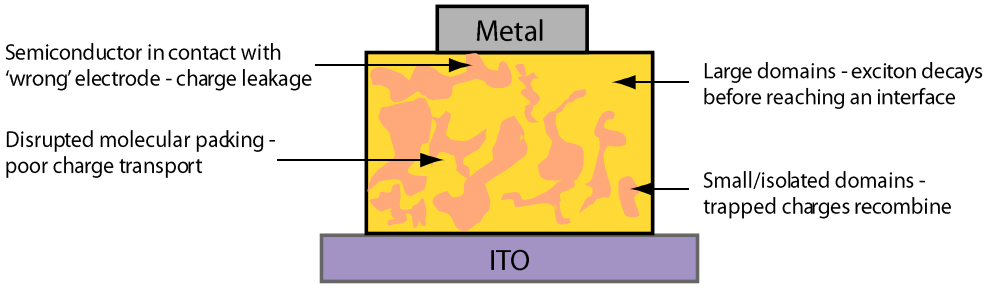

Figure 1.4 – Schematic of the microstructure of a BHJ device illustrating how non-optimum microstructure can affect the device performance. Adapted from [34].

Preferably, the polymer:acceptor composite film should spontaneously self-assemble into the most favourable morphology during deposition, but this is often not the case. The morphology of the BHJ photoactive layer depends on a wide number of intrinsic and extrinsic factors. Intrinsic factors are inherent to the photoactive materials used and their interaction with each other; they include physical properties of the individual materials such as hydrophobicity, molecular weight, surface energy, regioregularity and relative miscibility etc. Extrinsic factors include external factors such as solvent choice, substrate surface energy, D/A ratio, deposition technique and post-deposition annealing etc. A brief review of some of the notable steps in BHJ development is now given touching on some of the extrinsic factors mentioned. A more thorough review of the factors that influence BHJ device morphology can be found in references [34-36].

The first morphological study was carried out on MEH-PPV:C_{60} composite films using 1,2-dichlorobenzene (DCB) as the solvent.[37] Crystallites of C_{60} (~ 10 nm in diameter) were found embedded in amorphous MEH-PPV as a result of phase segregation. A fine bicontinuous network was observed when a 1:1 (by weight)

blend composition was used. Additionally, the low solubility of C_{60} in organic solvents prevented its use in high concentrations because it has a tendency to crystallise. Exchanging C_{60} for PCBM, a soluble derivative, circumvented this limitation.[30, 38]

Work by Shaheen *et. al*. on poly(2-methoxy-5-(3',7'-dimethyoctloxy)-p-phenylene vinylene) (MDMO-PPV), one of the early successful polymers, and PCBM (MDMO-PPV:PCBM) showed the important role played by the organic solvent.[39] Changing the solvent from toluene to chlorobenzene (CB) resulted in an increase in device PCE from 0.9 % to 2.5 %. The improvement in device performance was mainly due to an increase in short current density (J_{sc}). This improvement was explained by an increase in charge carrier mobility, attributed to the better solubility of PCBM in CB. From then on, CB and DCB became the most popular solvents to use in BHJ device development.

The importance of morphology on device performance was seen even more keenly when using regioregular poly (3-alkylthiophene), particularly poly(3-hexylthiophene) (P3HT). Compared to the earlier PPV polymers, P3AT polymers had a high regioregularity which allowed for an increased crystallinity. Due to the increased absorption and higher mobility, devices incorporating P3HT were expected to produce high efficiencies, but to begin with this did not happen. Pandinger *et.al*. demonstrated that annealing P3HT:PCBM devices increased the PCE from 0.4 % to 2.5 %.[40] Ma *et. al*. further demonstrated how vital thermal annealing is, achieving device efficiencies of 5 %.[41] When PCBM was blended with P3HT, the fullerene component was found to disrupt the intermolecular packing of the P3HT chains.[42]

Thermal annealing is thought to redistribute the P3HT and PCBM within the film which enables the ordering of P3HT to partially recover. This allows for higher mobilities and improved absorption.[43, 44]

Li *et.al*. reported that the degree of self-organisation could be varied by controlling the film growth rate.[45] Solvent annealing causes the wet film to dry slower. This allows the P3HT to reorganise and possess a higher degree of ordering, resulting in improved absorption and more balanced charge transport. The use of additives has also been shown to influence the solvent evaporation rate and therefore device performance. Additives have a higher boiling point than the primary solvent and so reduce the evaporation rate during deposition. They also selectively alter the relative solubility of a blend components. This approach is particularly effective for devices fabricated from low-bandgap polymers where thermal annealing does not often increase device efficiency.[46-48] Peet *et. al.* found incorporating a small amount of alkanedithiols into the poly[2,6-(4,4-bis-(2-ethylhexyl)-4*H*-cyclopenta [2,1-*b*;3,4-*b'*]dithiophene)-*alt*-4,7(2,1,3-benzothiadiazole)] (PCPDTBT):PCBM solution doubled the PCE as a result of changes in morphology.[46]

Since Tang's pioneering device in 1986 there has been significant progress in the understanding of OPV device physics, but there is still some way to go before OPV devices are developed into a mature technology. Device efficiencies are now above 10 % as a result of new photoactive materials and careful device design, however these record breaking devices are typically made in a lab on small areas using expensive materials and rigid substrates. In order for the full potential of OPV devices as a viable energy source to be achieved, development towards scalable processing on large areas with economical materials and flexible substrates need to

be seriously considered. In principle, BHJ devices do offer the opportunity to be volume produced by roll-to-roll compatible techniques, most likely through spray deposition or printing, and steps are being taken to find alternative and less costly materials.

1.2 Semiconductor theory

Atomic nuclei and electrons are the most basic building blocks of matter. In an atom (N = 1), electrons orbit around the nucleus which is made up of protons and neutrons. The number of electrons depends on the element. For the simplest case – hydrogen – one electron orbits around one proton. Each electron can be ascribed to an individual orbit known as the atomic orbital (AO) which has a discrete energy level. When an AO from one atom overlaps with the AO from another atom (N = 2) two molecular orbitals (MOs) are formed and the electrons are delocalised over both atoms. One of the MOs is bonding and this has a lower energy than that of the original AO. The other MO is anti-bonding and has an energy that is higher than the initial AO. **Figure 1.5** shows the energy level diagram for a H_2 molecule. The formation of a H_2 molecule involves the overlap of two single 1s orbitals, one from each atom. The Pauli exclusion principle limits the number or electrons that can occupy a MO to two and requires that the two electrons must be paired. For H_2 both electrons, one from each H, occupy the bonding (σ) orbital.

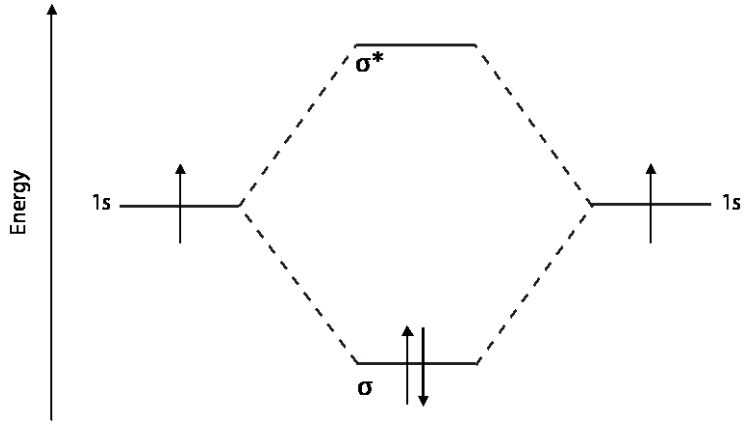

Figure 1.5 – The MO energy level diagram for a H_2 molecule. σ denotes the bonding and σ* the anti-bonding MO.

For three atoms there are three orbitals; one bonding and one antibonding with a nonbonding orbital in between. As more atoms are added, each one contributes one more AO and hence one more MO is formed. For *N* atoms in a line there are *N* MOs. The orbital with the highest energy is the most antibonding and the orbital with the lowest energy in the most bonding. The remainder of the orbitals are spread between the two extremes. The total width of the band remains finite as *N* approaches infinity and so there can only be a finite spread of orbital energies, regardless of *N*. As *N* approaches infinity the separation between neighbouring orbitals approaches zero. The discrete energy levels of the orbitals merge to form a band of near continuum energy levels for conductors. **Figure 1.6** shows the build-up of MO for a metal.[49]

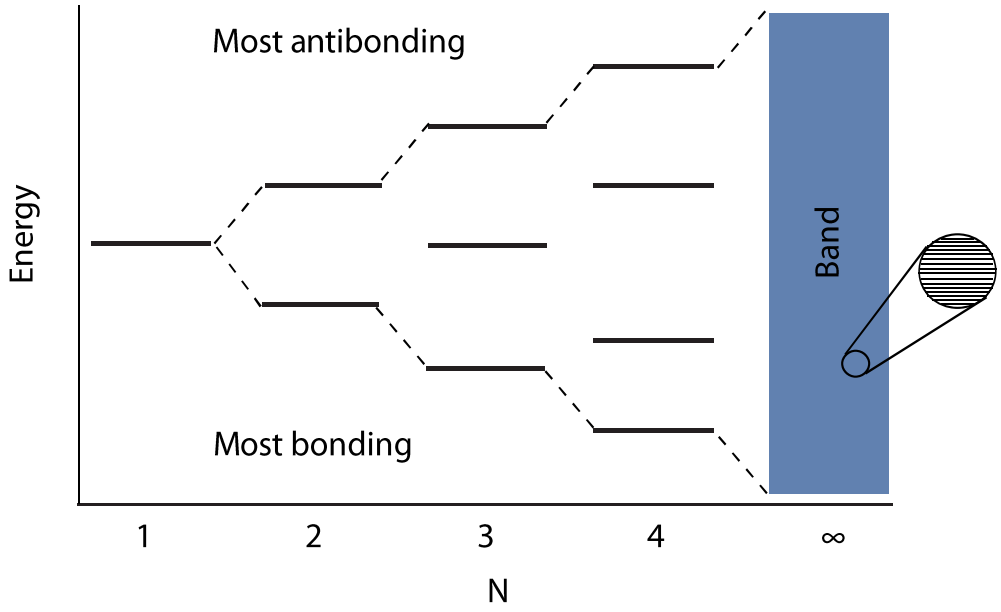

Figure 1.6 – The MO energy levels for N atoms for a metal. Adapted from [49].

For conductors the bonding and antibonding orbitals are not separated by an energy gap, as shown in **Figure 1.6**. In the case of non-metals such as insulators and semiconductors two bands are formed, the valence band (VB) and the conduction band (CB). The VB and CB are separated by an energy gap known as the band gap (E_g). This is due to the conjugated system undergoing geometrical distortion from a structure with equal band length to one with alternating long and short bonds. The geometrical distortion leads to the opening up of a band gap. This is known as Peirels Distortion.

The VB is normally fully occupied and the CB is generally unoccupied at 0 K. A schematic depicting the difference between metals (conductors), semiconductors and insulators is shown in **Figure 1.7**. Insulators have a large E_g, typically > 4 eV. At room temperature the electrons do not have enough energy to move from the VB to

the CB. On the other extreme, the electrons in conductors can be excited at room temperature are essentially free because there is no E_g. Semiconductors fall between the two. They have an E_g of ~ 1 – 4 eV; at sufficiently low temperatures the CB is completely empty and the VB is fully occupied. However, the E_g is sufficiently small that the electrons have the potential to reach the CB upon the appropriate input of energy.

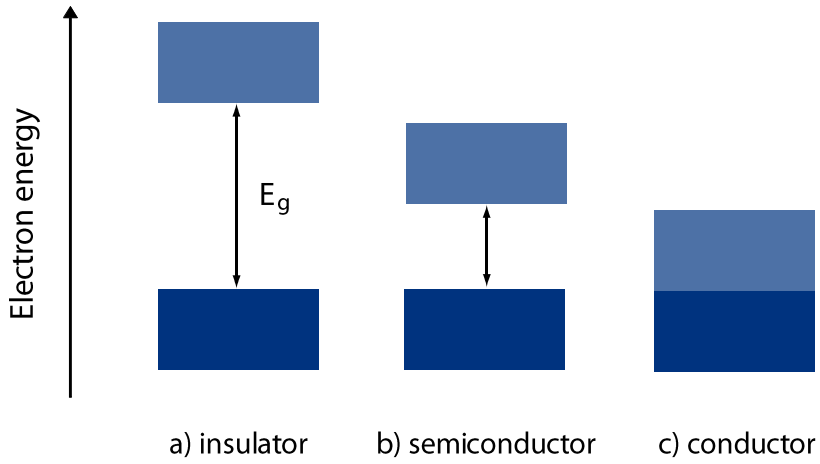

Figure 1.7 – The energy level diagrams of a) an insulator, b) semiconductor and c) conductor.

The Fermi-Dirac distribution (**Equation 1.1)** defines the probability of an electron existing at a particular energy level,

$$f(E) = \frac{1}{e^{\frac{E-E_f}{KT}}+1} \qquad \textbf{Equation 1.1}$$

where K is Boltzmann's constant, E_f is the Fermi level energy and T is the temperature. E_f is defined as the theoretical energy level where the population probability of an electron is ½. The work function (Φ) is the energy required to

remove an electron from the Fermi level to the vacuum level (E_{Vac}). The ionisation potential (E_{IP}) is the amount of energy required to remove an electron from the edge of the VB to the E_{Vac} and the electron affinity (E_{EA}) is the energy from the CB to the E_{Vac}. These are indicated in **Figure 1.8**.

The conductivity of semiconductors can be altered by doping. Doping is where a few atoms (< 0.1 %) of the original element are replaced by atoms having either more or less electrons. An *n*-type semiconductor is where the added (donor) atoms have more electrons in the valence shell than the host atom. If the donor atoms are spread out from each other, their electrons will be localised and a thin donor band will form. The donor atoms energy levels lie at a higher energy than the valence electrons of the host lattice, usually just below the empty CB of the lattice. Some of the electrons from the donor band can be promoted to the CB which are then able to move throughout the lattice. If the added atoms have fewer electrons than the host, positive holes are added and the semiconductor is said to be *p*-type. The dopant atoms form a thin, empty acceptor band that lies just above the full VB of the host lattice. Small amounts of energy can promote electrons from the VB to the acceptor band generating holes in the host VB which allows the remaining electrons to become mobile.

The number of electrons that can be promoted depends on the temperature and the energy gap between the bands. The Fermi level in an intrinsic semiconductor is likely to be near the middle of the band gap. For *n*-type semiconductors the Fermi levels rise to an energy level near the middle of the new donor band and the CB band of the host. The Fermi level drops to a point near the middle of new acceptor band

and valence band of the host for *p*-type semiconductors. **Figure 1.8** shows the band structure of intrinsic, *n*- and *p*-type semiconductors.

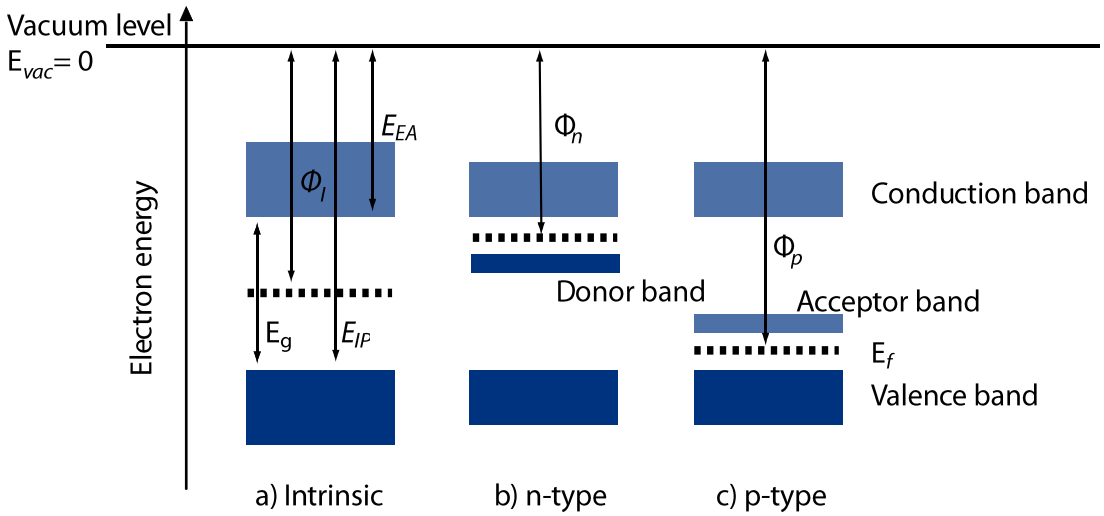

Figure 1.8 – Energy level diagram for a) an intrinsic, b) n-type and c) p-type semiconductors with the Φ, E_{IP} and E_{EA} labelled.

The terms CB and VB are typically used for inorganic materials. Organic semiconductors are made up of molecules rather than atoms and it is the MO that defines the energy structure. So instead of referring to the VB and CB, highest occupied molecular orbital (HOMO) and lowest unoccupied molecular orbital (LUMO) are used instead. Generally, the π-bonding orbitals combine to form the HOMO and the π-antibonding orbitals form the LUMO with the energy gap between the two defining the E_g.

1.3 Principles of device operation

An OPV device typically consists of photoactive material(s) and interfacial layers sandwiched between two electrodes, with a total device thickness of only a few hundred nanometers. This section discusses the principles of OPV device operation, using a regular bilayer device as an example. The processes can also be applied to BHJ devices.

Four major processes are involved in the conversion of solar energy to electrical energy. Firstly, light is absorbed and an exciton is formed within the photoactive layer (η_A). The exciton then randomly diffuses through the layer to a D/A interface (η_{ED}), here the exciton can dissociate into free carriers (η_{CT}). The free carriers are transported to their respective electrodes and collected (η_{CC}). These are shown for the donor material in **Figure 1.9**, the reverse situation with absorption in by the acceptor occurs by an analogous mechanism.

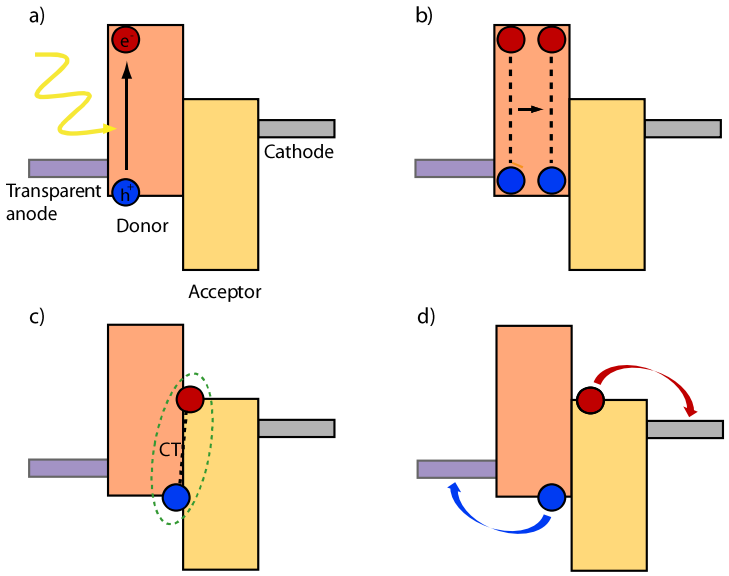

Figure 1.9 – The principles of OPV device operation under open circuit conditions: a) light absorption and exciton formation (η_A), b) exciton diffusion (η_{ED}), c) exciton dissociation (η_{CT}) and d) free carrier transport and collection (η_{CC}).

The overall external quantum efficiency (*EQE*) is defined as the number of charges extracted per incident photon and can be expressed as the product of the quantum efficiencies for the four processes (**Figure 1.2**)

$$EQE = \eta_A \eta_{ED} \eta_{CT} \eta_{cc} \qquad \textbf{Equation 1.2}$$

1.3.1 Absorption and exciton formation

When a photon of light that has an energy equal to or larger than the band gap of the OSC and is an allowed transition, it is absorbed by the photoactive layer. An electron is promoted from the HOMO to the LUMO of the material. A positive vacancy known as a hole is left behind. This excited state relaxes to form a coulombically bound electron-hole pair known as an exciton. The binding strength

between the hole and electron depends on the properties of the material. Organic materials have weaker intermolecular forces and low dielectric constants ($\varepsilon \sim 3$) and so strongly bound Frenkel excitons are formed. These excitons have a binding energy in the order of a few hundred meV which results in localised excitons forming on a single molecule. In contrast, the dielectric constant of inorganic semiconductors have large dielectric constants ($\varepsilon > 10$) and so weakly bound Mott-Wannier excitons are formed where the charge carriers are delocalised. Mott-Wannier excitons can be split into the separate charge carriers at room temperature (~ 26 meV). Unlike inorganic materials, the excitons generated upon light absorption in OPV devices require an additional step to separate them in to free charge carriers. The third type of exciton that can also form is known as a charge-transfer exciton. Here, the hole and electron are localised on neighbouring molecules but are still coulombically bound. The three different types of excitons are shown in **Figure 1.10**.

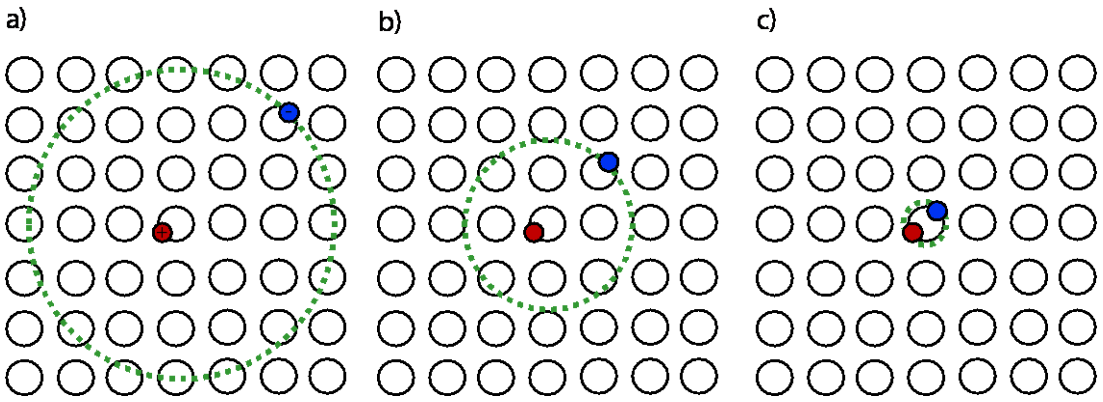

Figure 1.10 – Schematic of the three different types of exciton a) Wannier-Mott, b) charge-transfer and c) Frenkel exciton.

1.3.2 Exciton diffusion

Excitons are neutrally charged species and so their movement is not influenced by electric fields. Instead they diffuse by a random hopping motion between molecules or domains until they decay back to the ground state or reach a D/A interface and separate into free charges. The exction diffusion length (**Equation 1.3)** represents the average distance an exciton can travel before it decays and is material specific,

$$L_D = \sqrt{D\tau} \qquad \textbf{Equation 1 3}$$

where D is the diffusion coefficient and τ is the exciton lifetime usually in the order of nanoseconds. The L_D for OSC is typically in the order of a few to tens of nanometres.[50-52] The diffusion process is limited by grain boundaries and trap sites which cause recombination and competes with charge carrier recombination.

Due to the small exciton diffusion length the effective active region of a bilayer device is restricted to a narrow region near to the D/A interface. This limits the use of thick layers to improve light absorption. To avoid this problem the donor and acceptor are often mixed to create a BHJ device. With careful control of the morphology, excitons can be created within a L_D of a D/A interface. BHJ devices, however, suffer from decreased charge mobility due to a lack of continuous transport pathways to the electrodes which results in an increase in generation.

1.3.3 Exciton dissociation

Once at the D/A interface the exciton can dissociate into free carriers. In order to do so, the binding energy of the exciton must be overcome. The large stabilisation

energy of Frenkel excitons means that they cannot be split by thermal excitation. Instead, the binding energy can be overcome by the favourable energy offsets at the D/A interface. In the case where the exciton is formed in the donor material, the energy offset between the LUMO of the donor and LUMO of the acceptor must be larger than the exciton binding energy for effective dissociation to occur. The electron is then transferred to the LUMO of the acceptor and the hole remains in the HOMO of the donor. Likewise, the energy offsets between the HOMO of the acceptor and HOMO of the donor must also be large enough. The separation of an exciton at the interface into a hole and electron is known as the charge transfer (CT) state. Mobile free holes and electrons are formed from this state.

The energy offsets between the donor and acceptor energy levels directly impacts the V_{oc} of the device. The maximum obtainable V_{oc} is determined by the interface gap which is defined as the energy difference between the donor HOMO and acceptor LUMO. Ideally, the energy offsets need to be just large enough to allow efficient exciton dissociation, but small enough so that the V_{oc} is maximised. If the energy offsets are too small the exciton can recombine which limits charge separation. This type of recombination is known as geminate pair recombination (**Figure 1.11**). The electron-hole pair recombine at the D/A interface by transfer of the electron back from the LUMO of the acceptor to the HOMO of the donor. In BHJ devices this is a particular problem when the microstructure consists of large domains.

1.3.4 Free carrier transport and collection

After exciton dissociation, the separated charges drift and diffuse from the D/A interface to their respective electrode to produce the photocurrent. Charge carrier movement occurs through intermolecular hopping, the efficiency of which is dependent on the mobility of the organic material and is sensitive to the microstructure of the device. For bilayer devices, charges are generated at a single D/A interface and so there are large carrier concentration gradients present between the interface and electrodes. This results in strong diffusion currents in addition to drift currents.[53] Recombination is less likely because charges move through either pure donor or acceptor layer. For BHJ devices, however, there are multiple D/A interfaces. Charge generation is therefore distributed throughout the layer and the drift current dominates. BHJ devices often contain dead-ends and an intricate pathway of each component to the relevant electrode that hinder charge transport. In this case, bimolecular recombination (**Figure 1.11**) is more likely than for bilayer devices and competes with the charge separation and collection process. In bimolecular recombination the dissociated free charge carriers recombine before reaching the appropriate electrodes. Careful optimisation is needed for BHJ devices to maximise direct transport pathways to the electrodes.

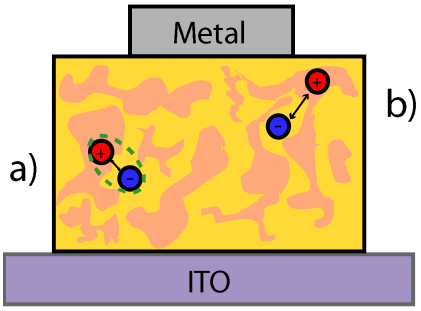

Figure 1.11 – Schematic of a) geminate pair and b) bimolecular recombination in a BHJ device.

Once at the electrode the charges need to be extracted with minimal losses. Ideally, the electrode work function should align with the HOMO (LUMO) of the organic material for efficient anode (cathode) injection. Poor alignment of the energy levels can result in injection barriers which are formed by band bending when the Fermi levels of the semiconductor and electrode align. It is possible to modify the electrode work function to improve the semiconductor/electrode contact. Materials such as self-assembled monolayers (SAMs), transition metal oxides and conductive polymers have been used to great effect.[54-56]

1.4 Material properties

Throughout this thesis several different photoactive layer combinations, interface layers and electrodes are used. This section outlines the general properties for each material used. A significant part of this thesis is concerned with using PEDOT:PSS as an electrode material. In this materials section, PEDOT:PSS is discussed with regards to its role as an interfacial layer. **Section 1.5** goes into more detail about the development of PEDOT:PSS and deals more fully the with the use of PEDOT:PSS as an electrode.

1.4.1 Poly(3-hexylthiophene)

Conjugated polymeric semiconductors are composed of aromatic repeat units that are directly coupled together with delocalised π electron conjugation along the backbone. Attaching aliphatic side chains to the polymer backbone results in the polymer becoming soluble so it can be more easily processed. Thiophene based polymers have been comprehensively studied in relation to OPV devices due to their spectral sensitivity in the long wavelength part of the solar spectrum and good charge carrier mobilities. Regioregular P3HT is the most studied polythiophene as it can be easily made on a multi-gram scale and can be simply processed from solution.

P3HT is non-symmetrical and so there are three possible orientations when the two thiophene rings are coupled in the 2- and 5-postions. These are 2,5’ or head-to-tail coupling (HT), 5,-5’ or tail-to-tail coupling (TT) and 2,2’ or head-to-head coupling. This results in a mixture of four chemically distinct regioisomers when 3-substituted

thiophene monomers are present (**Figure 1.12**, for the general poly(3-alkythiophene (P3AT) case).[35, 57] The degree of regioregularity refers to the percentage of HT couplings along the polymer backbone. There are several synthetic polymerisation processes which produce P3HT with high regioregularities.[58] A high RR percentage of P3HT allows the polymer backbone to obtain a near planar conformation facilitating intermolecular π stacking. Highly ordered π-stacked lamella type structures are formed in the solid state resulting in a red shift in thin film absorption, an increase in the solid-state absorption coefficient and increased charge carrier mobility (~ 10^{-1} cm^2 V^{-1} s^{-1}).[59-62]

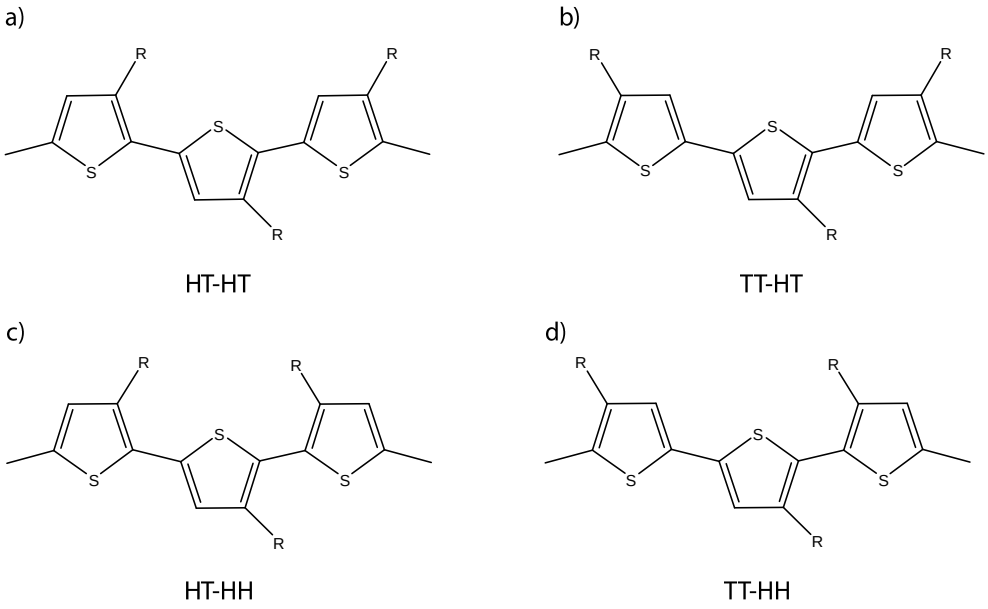

Figure 1.12 – Regioisomers of 2,4' linked P3AT a) HT-HT, b) HT-HH, c) TT-HT and d) TT-HT. R represents the alkyl group. Adapted from [35, 57].

P3HT shows high miscibility with PCBM (see **Section 1.4.5**) which allows a high ratio (1:1) of the polymer to be used in composite (P3HT:PCBM) films which increases light absorption and charge transport.[41] Earlier polymer:fullerene blends

required a much higher concentration of fullerene for optimum device performance.[39, 63] The HOMO and LUMO of P3HT are 4.6 – 5.0 eV and 2.7 – 3.0 eV respectively which when blended with PCBM allows for a favourable energy offset for efficient exciton dissociation.[64, 65] The structure of P3HT is shown in **Figure 1 13**.

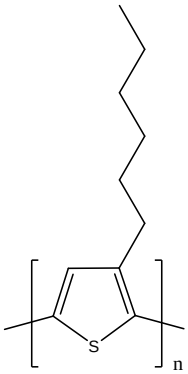

Figure 1 13 – Chemical structure of P3HT.

1.4.2 Copper phthalocyanine

Phthalocyanines (Pcs) were first discovered by chemists working at Scottish Dyes Ltd in 1928 and their structure was later elucidated in 1934.[66] Pcs are planar 18 π-electron macroheterocycles where four isoindole subunits are linked together by nitrogen atoms. Their extensively conjugated system generates an intense absorption spectrum which has resulted in Pcs being used in dyes and pigments as well as in organic electronics.[67] The two hydrogen atoms in the central metal cavity can be replaced by up to 70 individual different metal atoms which allows the physical and optical properties to be tailored. The thermal and environmental stability of Pcs make them popular materials for organic electronic applications.

CuPc was used as a donor material in the first bilayer OPV device.[19] It is planar and adopts a herringbone structure. The crystal arrangement and morphology depends on several factors including thermal treatment and type of substrate.[68, 69] Thermally evaporated CuPc thin films have a HOMO between 5.0 – 5.2 eV, a LUMO of 3.5 - 3.5 eV and a hole mobility of ~ 10^{-4} cm^2 V^{-1} s^{-1}.[70-72] **Figure 1.14.a** shows the chemical structure of CuPc.

1.4.3 Boron subphthalocyanine chloride

Subphthalocyanines (SubPcs) were first made in 1972 by Meller *et. al.* when trying to synthesize boronphthalocyanine.[73] SubPcs are a 14 π-electron aromatic non planar system. They consist of three diiminoisoindole rings surrounding a boron core.[74] The smaller size of this macrocyle means that only boron can be used as the cation in this system. The cone-shape of SuPcs leads to amorphous films with a hole mobility of ~ 10^{-5} cm^2 V^{-1} s^{-1}.[53] SubPc has a HOMO and LUMO of 5.6 eV and 3.6 eV respectively.[70] One of the advantages of using SubPc as a donor material instead of CuPc is its lower lying HOMO level. This results in a larger effective band gap and therefore larger V_{oc} when combined with C_{60} in bilayer devices.[70] The chemical structure of SubPc is shown in **Figure 1.14.b**.

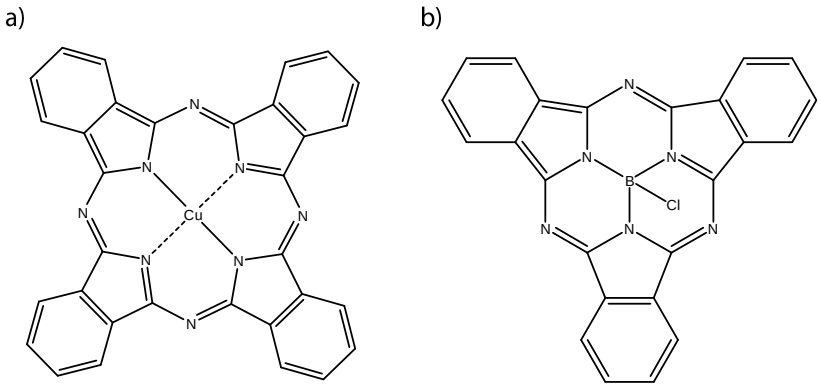

Figure 1.14 – Chemical structures of a) CuPc and b) SubPc

1.4.4 C_{60}

Fullerene based materials have been widely investigated as electroactive materials since their discovery in 1985.[20] C_{60} consists of 60 sp^2 hybridised carbon atoms that form 12 pentagons and 20 hexagons in a spherical structure. Due to the ring strain, the sp^2 carbons have a more tetragonal structure similar to sp^3 hybridisation rather than the preferred trigonal planar structure. This makes C_{60} susceptible to reactions with oxygen which leads to a decrease in conductivity.[75]

The extended conjugated π system enables C_{60} to accept between 6 and 12 electrons, which combined with a high electron mobility of ~ 10^{-2} cm^2 V^{-1} s^{-1}, has resulted in the extensive use of C_{60} in OPV devices as the electron acceptor.[72] C_{60} has a strong absorption below 500 nm, a HOMO energy level of 6.2 eV and a LUMO of 4.5 eV which makes it a suitable acceptor material for many electron donor materials.[76] The structure of C_{60} is displayed in **Figure 1.15.a**.

1.4.5 PCBM

C_{60} displays very low solubility in most common organic solvents which has led to the synthesis of a variety of functionalised derivatives with the aim of improving the solubility and further tuning the electronic properties.[38] PCBM has since become one of the most successful soluble fullerene derivatives that is used as an electron acceptor in OPV devices. Like C_{60}, PCBM crystallises into well-defined structures which depend on the processing solvent.[77] When compared to C_{60}, the absorption profile of PCBM is enhanced with increased absorption at longer wavelengths. PCBM has a HOMO and LUMO of 6.1 eV and 4.3 eV respectively, which allows for efficient exciton dissociation when blended with P3HT.[78] **Figure 1.15.b** shows the chemical structure of PCBM.

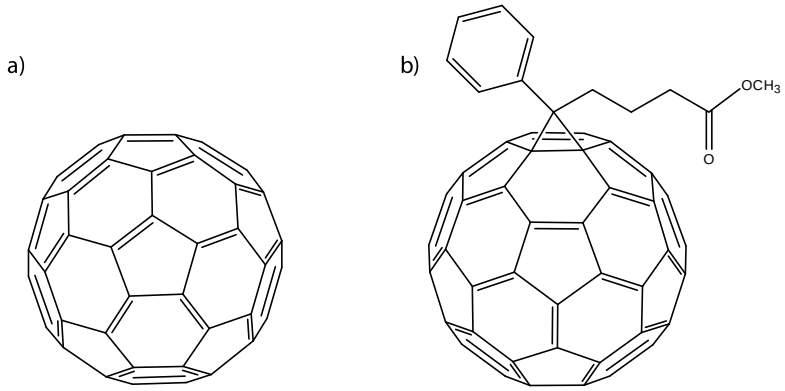

Figure 1.15 – Chemical structures of a) C_{60} and b) PCBM

1.4.6 Electrode materials

OPV devices typically use indium tin oxide (ITO) as the transparent conducting electrode (TCE). ITO is generally used as the TCE due to its low sheet resistance (R_{sheet}) and high optical transparency; these favourable properties make it the choice

electrode for many different optoelectronic devices. ITO is made up of indium oxide and tin in a typical 9:1 ratio. The limited availability and high demand for indium, alongside the energy intensive vacuum sputtering process required to produce ITO results in the ITO electrode contributing 38 – 51 % to the total cost of an OPV device.[79] This high cost along with limited energetic compatibility with frequently used OSCs, poor flexibility and tendency to crack and/or delaminate, has resulted in a strong interest to find an alternative material for use as the TCE. Several different materials have been investigated including graphene,[80] carbon nanotubes,[81] thin metal films,[82] metal grids,[83] nanowires,[84] and conducting polymers.[85] Poly(3,4-ethylenedioxythiophene):poly(styrenesulfonate) (PEDOT:PSS) is an intrinsically conducting polymer that has attracted increasing interest for this role. The use of PEDOT:PSS as an alternative electrode is discussed in **Section 1.5**.

Aluminium (Al) was used as the back electrode for all the OPV devices in this thesis. Al has a relatively low work function of ~ 4.2 eV. It is inexpensive, abundant and can be easily thermally evaporated into thin films.

1.4.7 Interfacial materials

Not only is the work function of ITO not compatible with several commonly used organic photoactive layers, but it is also sensitive to the state of the surface. A number of different factors, such as the composition, cleaning procedure and exposure to oxygen can modify the conductivity and work function of the ITO electrode.[86, 87]

The use of different interfacial layers such as conductive polymers, transition metal oxides and self-assembling monolayers (SAMs) can be used to tune the work function of the ITO electrode and smooth out conductive inhomogeneities. The conductive polymer PEDOT:PSS is the most commonly used solution processable hole transporting layer which is used to modify the ITO anode. PEDOT:PSS has a higher work function (5.0 – 5.2 eV) than ITO (typically 4.5 – 4.8 eV) resulting in a better energetic alignment with many commonly used photoactive donor materials.[56] A more detailed discussion of PEDOT:PSS is given in **Section 1.5**.

Transition metal oxides such as molybdenum oxide (MoO_x) have also been successfully used as hole extracting layer. MoO_x has a high optical transparency, reasonable conductivity and has favourable energetic alignment for hole extraction. The work function of MoO_x has been shown to vary from 5.3 eV (after exposure to oxygen) to 6.9 eV (freshly evaporated) depending on the environment the layer is processed in. MoO_x can also be deposited by solution processing on top of the ITO anode. Other advantages of using MoO_x is that it is easy to thermally evaporate before or after the photoactive layer so can be used in both regular and inverted device architectures and it has been shown to improve device stability.[55]

Bathocuproine (BCP) was used as an exciton blocking layer in regular device structures. BCP has a large band gap of ~ 3.5 eV and so prevents excitons reaching and therefore quenching at the Al electrode.[21] BCP also acts as a sacrificial layer, protecting the photoactive layer from damage due to electrode deposition.[88] The structure of BCP is displayed in **Figure 1. 16**.

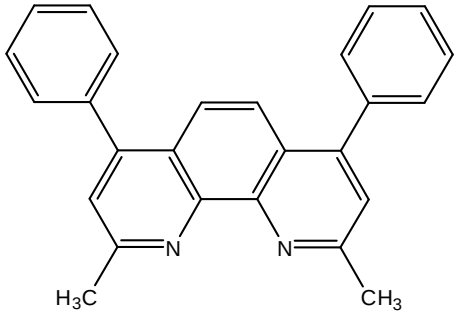

Figure 1. 16 – Chemical structure of BCP.

Thin layers of n-type transition metal oxide such as zinc oxide (ZnO) can be used to reverse the polarity of the OPV device. A sol-gel processed ZnO electron extracting layer can be used to modify the ITO electrode to selectively collect electrons. The ZnO layer is highly transparent and has a work function of 3.8 eV. In inverted structures MoO_X was used as the hole extracting layer between the photoactive layer and the Al top electrode.

1.5 The application of PEDOT:PSS in OPV devices

After the discovery that doped polyacetylene could achieve high conductivities in 1977, interest in intrinsic conductive polymers (ICPs) rose significantly.[89] Despite the high conductivity, the severe degradation in air and poor processability of polyacetylene prevented it from commercialisation. Many attempts were made to produce ICPs with the desired properties to make them commercially successful. The required properties included high conductivity, processability and long term stability while under application conditions. Some of the candidates considered were polyanilines, polypyrroles and polythiophenes. Unfortunately, polyanilines produce toxic products upon degradation, and polypyrroles and polythiophenes are insoluble in most solvents.[90] A breakthrough came in the late 1980s when scientists at Bayer AG research laboratories in Germany developed a new polythiophene derivative, poly(3,4-ethylenedioxythiophene) (PEDOT).[91]

1.5.1 Chemical and structural properties

Although PEDOT is insoluble and unstable in its neutral state, it exhibited several interesting properties. It had a high conductivity (~ 300 S cm^{-1}), thin oxidised films were nearly transparent and it showed very high stability in the oxidised state.[92-94] The solubility issue was resolved by using a water soluble electrolyte, poly(styrene sulfonic acid) (PSS). The PSS performs two important roles: it acts as a charge balancing counter ion during polymerisation to yield PEDOT:PSS and it allows the PEDOT segments to disperse in water.[95] The short PEDOT oligomers tightly attach to the higher molecular weight PSS chain. The chains then tangle together to form a

loosely crosslinked polymer gel network were the gel particles consist of ~ 95 % water (**Figure 1.17**)

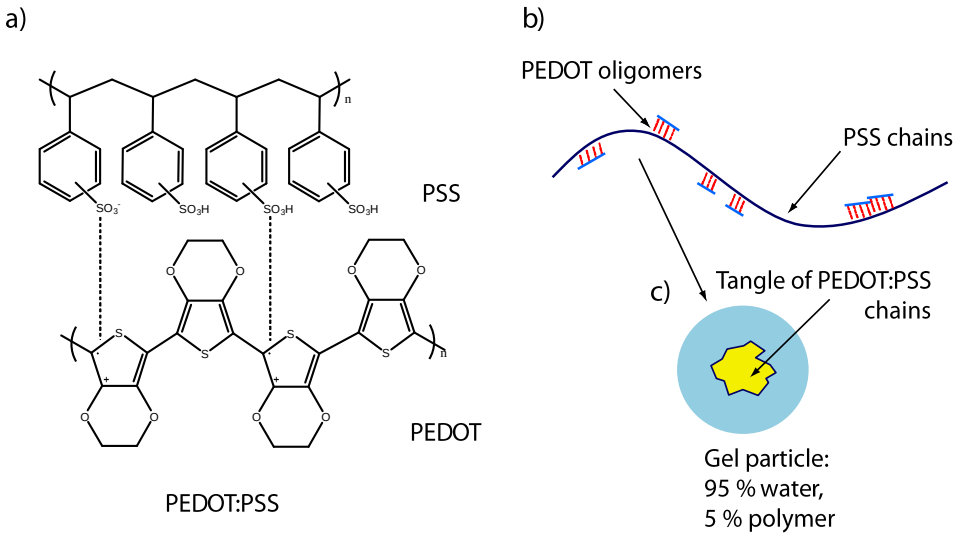

Figure 1.17 - Schematic of the a) chemical structure of PEDOT:PSS, b) the oligomeric PEDOT attached to the PSS and c) the gel particle, Adapted from [85].

The resulting PEDOT:PSS complex is not truly water soluble but it is still able to form a stable, dark blue microdispersion which is easily processed into amorphous thin films (**Figure 1.18**). The PEDOT:PSS films possess a high conductivity (~ 10 S cm^{-1}), high transparency in the visible region and good stability.

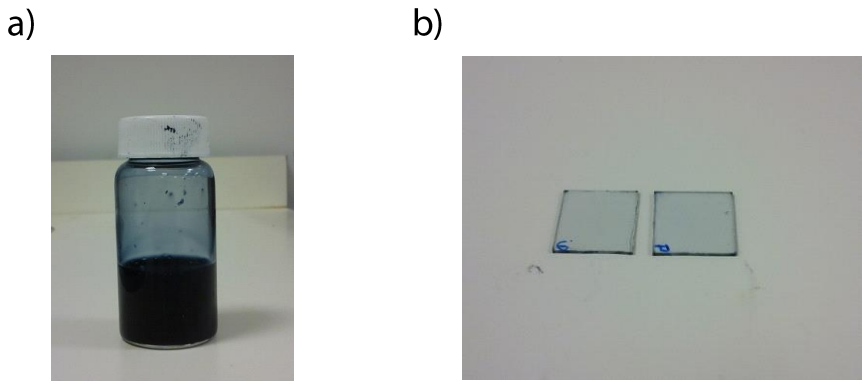

Figure 1.18 – Images of a) the dark blue dispersion and b) the resulting transparent thin film.

The processing and thin film properties of PEDOT:PSS can be altered by modifying the formulation. This has allowed PEDOT:PSS to be used in a wide range of organic electronic applications. It first found use as an antistatic coating in photographic film,[89] followed by widespread use as a transparent conductive layer in electroluminescent devices, capacitors, and transistors, and as a hole injection layer in organic light emitting diodes (OLEDS).[85] In OPV devices, PEDOT:PSS has been extensively used as a hole transport layer because it has a higher work function (~ 5.0 – 5.2 eV) than ITO (typically ~ 4.5 – 4.8 eV) which produces favourable energy level matching between the ITO electrode and organic layers. The lower work function of ITO often results in the formation of a charge injection barrier which hinders the performance of the OPV device. With PEDOT:PSS as an interfacial layer between the ITO electrode and organic donor, an ohmic contact forms resulting in improved hole collection.

It is widely agreed that spin coated PEDOT:PSS films consist of phase segregated PEDOT:PSS grains surrounded by a shell of excess PSS where the thickness of the

grain boundary is reported to be ~ 3 – 4 nm.[90, 91] The PEDOT-rich core of the PEDOT:PSS grains has a higher conductivity than the PEDOT-depleted grain boundary due to the insulating nature of the PSS. This means that charge is easily transported within the PEDOT:PSS-rich grain and the more insulating grain boundary is the main obstacle for charge transport and therefore limits the overall conductivity of the thin film.[92] Nardes *et. al*. observed 'pancake-shaped' PEDOT-rich grains separated by lamellas of PSS using cross-sectional AFM and scanning tunnelling microscopy (STM).[93] The typical diameter (*d*) of the PEDOT-rich grains was found to be ~ 20 – 25 nm and the height (*h*) was ~ 5 – 6 nm. **Figure 1.19** shows the schematic for the proposed morphological model for PEDOT:PSS thin films. This was used to explain why the vertical conductivity to is so much lower than the lateral conductivity of PEDOT:PSS films.

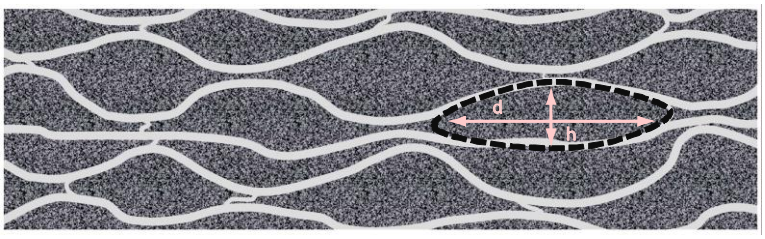

Figure 1.19 – Schematic of the morphological model for PEDOT:PSS derived from the STM and AFM measurements. Adapted from [93].

In addition to the insulating PSS, there are some other concerns with using PEDOT:PSS in organic electronic devices. The acidic nature of the PEDOT:PSS films causes indium to diffuse into the photoactive layer and the excess PSS makes the films hygroscopic leading to significant water uptake.[94, 95] Despite these concerns, the highly transparent, low cost, easily processable films with flexible

applications has led to PEDOT:PSS being investigated as a potential alternative to ITO in OPV devices.

1.5.2 Conductivity enhancement: pre-deposition

Even with the development of highly conductive PEDOT:PSS formulations, the conductivity of PEDOT:PSS thin films are still much lower than that of ITO. Many different methods to improve the conductivity of these films by 2 to 3 orders of magnitude have been reported. These include the addition of a small volume percentage (vol-%) of surfactants, ionic liquids, polyols and polar organic solvents to the PEDOT:PSS dispersion. How the conductivity is improved is still not clear and possible mechanisms continue to be widely discussed in literature. It is believed to depend on the chemicals and treatment process used.

Kim *et.al*. reported that the high dielectric constant of organic solvents like dimethyl sulfoxide (DMSO) and *N,N*-dimethyl formamide (DMF) resulted in screening effects between the PEDOT and PSS chains.[96] This thereby reduced the columbic charge between the components and improved the conductivity of the PEDOT:PSS film. Ouyang *et. al*. observed that polar solvents induced a change in the conformation of PEDOT chains in the film.[97] Treated films were said to have a less coiled and more linear structure resulting in increased conductivity due to better inter and intrachain carrier movement. Morphological changes to the film were shown upon addition of diethylene glycol (DEG) to the PEDOT:PSS dispersion.[98] The change in morphology was attributed to a change in the distribution of excess PSS within the film. Upon addition of DEG, the PSS became partially segregated leading to thinner

insulating barriers. This allowed for better conducting pathways and formation of a three-dimensional network of conducting PEDOT:PSS. Addition of DMSO was also shown to change the morphology of PEDOT:PSS films. Films were reported to have enlarged PEDOT-rich grains which were more uniformly distributed and thinner PSS barriers between conductive grains.[99] This led to better charge transport pathways in both vertical and lateral directions. Cruz-Cruz *et. al.* also reported that the thickness of the insulating PSS barrier is decreased and PEDOT-rich grains increase on addition of DMSO.[100] Adding a flurosurfactant along with DMSO to the PEDOT:PSS dispersion not only resulted in an improvement in conductivity but also made the films reversibly stretchable indicating PEDOT:PSS has a potential application in flexible OPV devices.[101, 102]

Sorbitol has also been used to improve the conductivity of PEDOT:PSS films with great effect. Pettersson *et.al*. determined that sorbitol acts as a plasticiser, which assisted with the reorientation of PEDOT:PSS chains when the films were heated.[103] The reorientation led to improved connections between the conducting PEDOT chains. The idea that sorbitol acted as a plasticiser was further supported by Nardes *et.al*., who proposed that the evaporation of water and sorbitol led to an increase in the free energy of the film.[104] The remaining mixture was then able to rearrange into a more relaxed and compacted morphology. A change in the morphology of the films was also reported by Jönsson *et. al*.[105] The improvement in conductivity was deemed to be due to better interconnecting pathways between the conducting PEDOT:PSS after excess PSS has been removed from the surface during film formation. Other reports also suggested that sorbitol leads to an increase in the size of PEDOT-rich grains,[106] and a decrease in the thickness of the insulating PSS

barrier between PEDOT-rich grains.[107] Ionic liquids, amphiphilic fluoro compounds and germinal diols have also been reported to improve the conductivity in a similar manner.[108-110]

1.5.3 Conductivity enhancement: post-deposition

Post-treating pre-formed PEDOT:PSS films can also enhance the thin film conductivity. Xia *et.al.* reported that dropping a cosolvent of water and common organic solvent such as methanol, ethanol and isopropanol (IPA) on to untreated PEDOT:PSS films improved the conductivity.[111] The conductivity enhancement was attributed to the preferential solvation of the PEDOT and PSS chains by the organic solvent and water respectively. This was said to induce phase segregation and a more linear PEDOT:PSS conformation. Methanol, used by itself, dropped on to the PEDOT:PSS film was also shown to improve the film conductivity.[112] When the methanol treated film was subsequently immersed in methanol a further improvement in conductivity was observed. The authors proposed that the initial methanol drop brought about a screening effect between the PEDOT and PSS chains which facilitated phase segregation and reorientation of the PEDOT:PSS chains into a more linear conformation. The following methanol immersion then removed any excess PSS from the film surface. Several other reports have also shown an increase in film conductivity through combination of pre and post-deposition treatment. Kim *et. al.* added EG to the PEDOT:PSS dispersion before deposition and then immersed the resulting films in EG.[113, 114] DMSO has also been added to the PEDOT:PSS dispersion and the film was then immersed in EG.[115] The improvement in

conductivity observed was attributed to the removal of excess PSS from the PEDOT:PSS film upon immersion in the solvent. The removal of PSS was thought to increase the intergrain coupling between PEDOT-rich grains.[115] Some of the highest PEDOT:PSS film conductivities have been reported using sulphuric acid (H_2SO_4).[116, 117] Xia *et. al*. dropped a small amount of the acid onto the pre-formed film and Kim *et. al*. immersed films in H_2SO_4. In both cases the removal of excess PSS and conformational change in the PEDOT:PSS chains were cited as reasons from the improved conductivity.

1.6 Thesis outline

Chapter 1 has introduced the requirement for renewable energy sources and focused on how solar energy is a viable energy source. A history of some of the notable achievements in OPV device progression was given with emphasis on BHJ devices followed by an overview of device operation. The materials used in this thesis were then introduced and particular emphasis was given to the development of PEDOT:PSS. The work presented in this thesis first focuses on using highly conductive PEDOT:PSS as an electrode material, to replace ITO, and then goes on to look at P3HT:PCBM BHJ device fabrication processes.

Chapter 2 covers the experimental and analysis techniques used to form and characterise thin films and OPV devices.

Chapter 3 is concerned with the characterisation and use of PEDOT:PSS thin films as electrodes in OPV devices. This chapter is spilt in to three sections. The first section directly compares two different treatments to enhance the conductivity of PEDOT:PSS thin films deposited by spin coating. 5 vol-% of DMSO was added to the PEDOT:PSS dispersion (PEDOT:PSS_{ADD}) or untreated films were immersed in DMSO for 30 minutes (PEDOT:PSS_{IMM}). The DMSO treated PEDOT:PSS electrodes are then directly compared to each other and untreated PEDOT:PSS (PEDOT:PSS_{UT}) as electrodes in P3HT:PCBM BHJ devices. The middle section compares PEDOT:PSS_{ADD} thin films deposited by two different deposition methods – spin coating and spray deposition – in CuPc/C_{60} bilayer devices. The third section considers the effect of increasing the active area size on the device performance when using PEDOT:PSS_{ADD} electrodes in SubPc/C_{60} bilayer devices.

Chapter 4 looks at the fabrication process for P3HT:PCBM BHJ devices and is split in to three sections. For optimum performance these devices are usually fabricated under inert atmospheres. The first section looks at how to achieve comparable device performance when the photoactive layer is deposited under an ambient atmosphere. The rest of the chapter looks at replacing DCB as the solvent for P3HT:PCBM photoactive layers with a non-halogenated solvent to make for a more environmentally friendly solution. The middle section discusses why toluene is a 'bad' solvent when used in regular device structures While the final section studies P3HT:PCBM dissolved in a tolunene:1-methylnahpthtalene mixture. The importance of selection the appropriate interfacial layer is addressed and both regular and inverted architectures are studied.

Chapter 5 makes some concluding remarks about the work carried out in this thesis.

Chapter 6 discusses some possible future directions to progress this work further.

Chapter 2. Experimental methods and analysis

This chapter firstly outlines the thin film and device preparation and fabrication process. The techniques that are used to characterise the thin films are then discussed. The section concludes with how devices were analysed.

2.1 Thin film and device fabrication

This section starts by describing the material, substrate and solution preparation involved in thin film and OPV device fabrication. The thin film fabrication techniques that were used are then introduced. They consist of two solution processing techniques, spin coating and spray deposition. In addition vacuum deposition is described.

2.1.1 Material purification

P3HT, PCBM and SubPc were used as received and not subjected to any further purification procedures. CuPc and C_{60} were further purified by thermal gradient sublimation. The suppliers and purities of the photoactive materials used are shown in **Table 2.1.**

Table 2.1- The suppliers and purities of the photoactive materials used.

Compound	*Supplier*	*Purity (%)*	*Sublimed*
P3HT	Rieke Metals	n/k	No
CuPc	Sigma-Aldrich	97	Yes
SubPc	Lumtec	99	No
PCBM	Solenne BV	99.5	No
C_{60}	Nano-C inc	99.5	Yes

Further purification is thought to reduce the batch-to-batch variation seen in OPV device performance. A schematic of the thermal gradient sublimation system is shown in **Figure 2.1**. It consisted of placing the unpurified material at the end of a disposable quartz tube. A small amount of glass wool was put in the open end of the tube to stop any organic material getting drawn into the vacuum pump. The tube was then placed inside a larger quartz tube. The tube was then placed into the furnace and connected to a turbo molecular pump. Purification was carried out at ~ 10^{-5} mbar. Once under vacuum the temperature was ramped at a rate of 0.1 – 1 ^{o}C min^{-1} until the sublimation temperature was reached (material dependent). The temperature was then kept constant for 10 – 15 hours. A temperature gradient was created from the end of the tube, located at the centre of the furnace, to the end which was outside. The unpurified material sublimed and condensed at a lower temperature further down the tube, separating the low temperature impurities from the pure material. The system was cooled back down to room temperature, the inner tube was removed and cut open. The band of pure material was the collected and stored under a nitrogen (N_2) atmosphere.

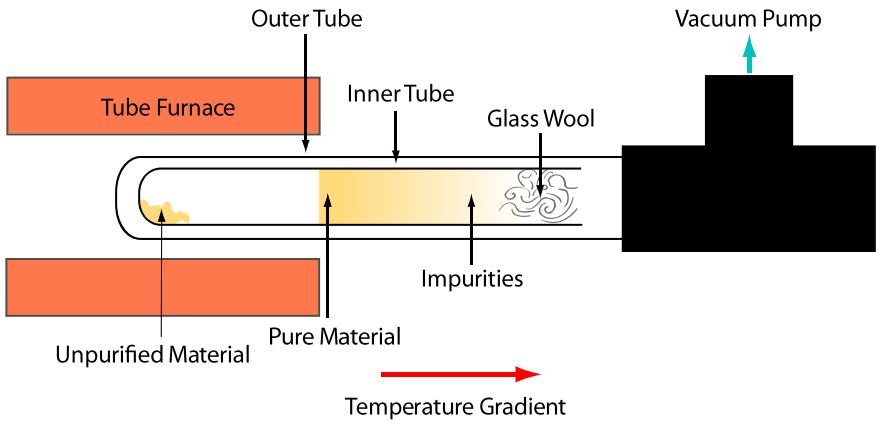

Figure 2.1 - Schematic of the thermal gradient sublimation system.

The compounds used for the interfacial layers and metal electrode were used as received.

2.1.2 Substrate preparation

All thin films were deposited on to ITO (Thin Film Devices, R_{sheet} < 15 Ω sq^{-1}), quartz or glass substrates. The ITO and quartz substrates were obtained pre-cut to 12 x 12 mm. The ITO coated glass substrates were pre-patterned with an 8 mm ITO strip down the centre leaving 2 nm uncoated on either side. The glass substrates were cut to size from a glass slide using a diamond scribe. Glass substrates were cut to 12 x 12 mm for devices with 0.06 cm^{-2} and 0.16 cm^{-2} active areas. For larger active areas of 0.30 cm^{-2} and 1.04 cm^{-2} glass substrates were cut to 18 x 18 mm and 26 x 30 mm.

The following cleaning procedure was used for all substrate types:

- Rinse with acetone
- Sonicate in acetone for 15 minutes
- Rinse with water
- Sonciate in water:decon mix (70:30) for 15 minutes
- Rinse with water
- Sonicate in water for 15 minutes
- Rinse with IPA
- Sonicate in IPA for 15 minutes

Substrates were then removed from the IPA and dried with a N_2 jet. The substrates then underwent UV/ozone treatment for 30 minutes to remove any residue organic contaminants from the surface.[118]

2.1.3 Preparation of the PEDOT:PSS thin films

All PEDOT:PSS dispersions were obtained from Heraeus Holding GmbH. A few ml of each stock dispersion was decanted into a glass vial before any modifications were made. The stock and modified dispersions were kept in a fridge when not being used. Before use, the relevant solution was removed from the fridge 30 minutes before use.

The Clevios PH1000 dispersion was used for all the three different PEDOT:PSS electrodes. The PEDOT:PSS_{ADD} solution was prepared by adding DMSO (5 vol-%) to the as-bought PEDOT:PSS dispersion. Untreated PEDOT:PSS (PEDOT:PSS_{UT}) and PEDOT:PSS_{IMM} electrodes were formed using as-bought PEDOT:PSS. Each solution was filtered (0.45 µm, PVDF) at room temperature before deposition by either spin coating or spray deposition. The electrodes were then annealed on a hot plate at 110 ^{o}C for 20 minutes in an ambient atmosphere. The PEDOT:PSS_{IMM} electrodes were then cooled to room temperature and immersed in DMSO for 30 minutes. The films were then placed on a hot plate at 110 ^{o}C until dry. All films were allowed to cool to room temperature before further procedures were carried out.

A less conductive PEDOT:PSS dispersion (Clevios P VP 4083) was used as a hole transporting layer (PEDOT:PSS_{HTL}) in combination with an ITO electrode. It was

used as-brought. The dispersion was filtered (0.45 μm, PVDF) and spin coated on top of the pre-cleaned ITO electrode and annealed as above.

Clevios HTL Solar was used as the hole transporting layer in inverted devices. This dispersion was used as-brought. The dispersion was filtered (0.45 μm, PVDF) and spin coated on top of the P3HT:PCBM photoactive layer and annealed as above.

Table 2.2 displays the differences between the different PEDOT:PSS formulations as given by the manufacture.[119]

Table 2.2 – The manufacturer given physical characteristics of the different PEDOT:PSS formulations used as taken from Ref [119].

Formulation	*Solid Content (%)*	*Conductivity (Scm^{-1})*	*Viscosity (MPas)*	*PEDOT:PSS ratio (by weight)*
PH1000	1.0 – 1.3	850*	15 -50	1:2.5
P VP 4083	1.3 – 1.7	0.002 - 0002	5 - 12	1:6
HTL Solar	1.0 – 1.2	0.1 – 1.0	8 -30	N/K

*After the addition of 5% DMSO. Measured on the dry coating.

All PEDOT:PSS film preparation steps were carried out in air.

2.1.4 Preparation of the P3HT:PCBM photoactive layer

The P3HT:PCBM photoactive layer was prepared by stirring 20 mg ml^{-1} of P3HT and PCBM in 1,2-dichlorobenzene (DCB) at 40 ^{o}C for 24 hours. The P3HT:PCBM solution was then filtered (0.2 μm, PTFE) and spin coated onto the relevant

electrode. The solutions were kept under N_2 unless otherwise stated. After P3HT:PCBM deposition the substrates were covered with a petri dish lid and allowed to dry. This was followed by an annealing step at 120 ^oC for 20 minutes under N_2 unless otherwise stated.

For the non-halogenated photoactive layers 13 mg ml^{-1} of P3HT:PCBM was stirred in toluene and a toluene:1-methylnaphthalene mix for 24 hours under a N_2 atmosphere. The relevant amounts (see text in **Section 4.3** and **4.4**) of 1-methylnaphthalene were added to the toluene solution in air and left to stir for a few hours. 15 mg ml^{-1} of both components were stirred in 1-methylnaphthalene for 24 hours.

2.1.5 Preparation of the ZnO sol-gel electron extracting layer

The ZnO sol-gel was prepared by dissolving zinc acetate (Aldrich. 99.99 %) in ethanol (0.25 M), which was stirred at 80 ^oC for 2 hours. The 2-amino-ethanol stabiliser (Aldrich, 99.5 %, 5 vol-%) was then added and the solution was left to stir at 60 ^oC overnight. The solution was allowed to cool to room temperature and filtered (0.22 μm, PVDF) before deposition. After deposition the films were allowed to stand at room temperature for 3 minutes before annealing at 150 ^oC for 1 hour. The ZnO layer preparation steps were carried out in air.

2.1.6 Solution processed thin films: spin coating

Spin coating is the most commonly used technique used for fabricating lab-scale solution processed OPV devices. This technique allows for the formation of highly reproducible and homogeneous films. The following spin coating procedure was used in this work: the required solution was dispensed onto the static pre-cleaned substrate. The substrate was then rapidly accelerated to a high angular velocity (spin speed). The centrifugal forces acting on the rotating liquid caused the solution to spread to and over the substrate edges. This combined with subsequent evaporation of the solvent results in the formation of a thin film (**Figure 2.2**).[120] The final film thickness, microstructure and surface topography are highly dependent of the spin speed and the solvent properties such as viscosity, concentration and volatility.[121] There are some drawbacks with spin coating. It is quite wasteful and substrates are usually treated individually, therefore it is not immediately applicable to scaling up device manufacture.

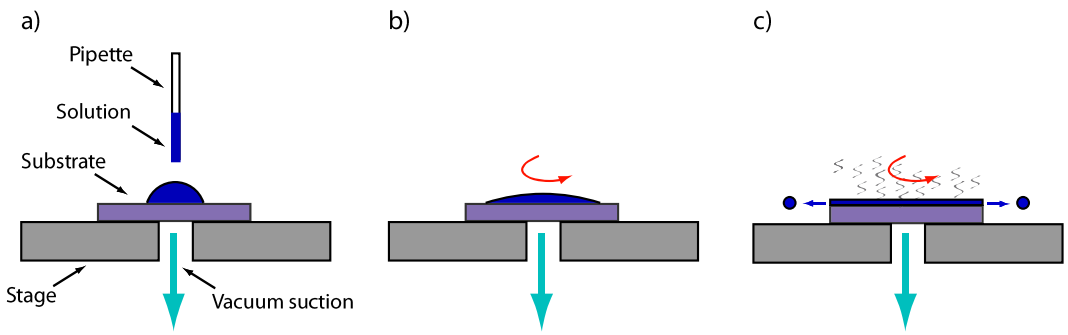

Figure 2.2 – Schematic of the spin coating process: a) solution dispensed onto the static substrate, b) substrate accelerated to a high angular velocity and c) spreading and evaporation of the solution to produce thin films.

All spin coated layers were fabricated using Laurell Technologies spin coaters under ambient and inert (N_2) conditions. **Table 2.3** lists the material, atmosphere and spin speed used to form each spin coated layer. All deposition times were for 60 seconds.

Table 2.3 – Details of the spin coated layers in this thesis. HTL stands for hole transport layer and EEL for electron extracting layer.

Material	*Role*	*Atmosphere*	*Spin speed (RPM)*	*Film thickness (RPM)*
PEDOT:PSS_{UT}	Electrode	Air	2000	90
PEDOT:PSS_{ADD}	Layer	Air	2000	86
PEDOT:PSS_{ADD}	Electrode	Air	3000	68
PEDOT:PSS_{IMM}	Electrode	Air	2000	58
PEDOT:PSS_{HTL}	HTL	Air	3000	37
PEDOT:PSS_{Solar}	HTL	Air	3000	n/k
ZnO	EEL	Air	3000	35
P3HT:PCBM	Active layer	N_2	800*	†
P3HT:PCBM	Active layer	Air	800*	†

* Unless otherwise state in text.

† P3HT:PCBM photoactive layer spin cast from DCB under N2 gave a film thickness of ~ 130 nm. The film thickness was not measured for films cast in air for this spin speed, but films cast under both N_2 and air gave a similar thickness when spin coated at a faster spin speed. The film thickness was not measured for photoactive layer spin cast out of non-halogenated solvents.

2.1.7 Solution processed thin films: spray deposition

Spray deposition is a well-established industrial technique that has attracted interest for OPV device fabrication due to its low cost, minimal material wastage, and diverse substrate compatibility.[122-125] Spray deposition, therefore, has the potential to meet the demands required for a commercially viable deposition technique, as evidenced by its present use in other industries.[126] The spray deposited electrodes were formed using a commercially available airbrush (Iwata Custom Micron CM-C Plus) as shown in **Figure 2.3**[127].

Figure 2.3 – Image of the Iwata Custom Micron CM-C Plus used to spray deposit PEDOT:PSS taken from Ref [127].

The airbrush has a 0.23 mm nozzle and a dual action trigger. The PEDOT:PSS_{ADD} solution was transported from a 9 ml gravity-feed cup along the needle to the nozzle and then onto the substrate by a carrier gas (house N_2 was used) where a micro-line to a 25 mm round spray pattern can be created[127].

Two different spray deposition techniques were employed in this work. In the first method, multiple heated (60 ^{o}C) glass substrates were consecutively passed once through the PEDOT:PSS flux at a controlled speed (**Figure 2.4.a**). The airbrush was kept at a constant height of 8 cm above the substrates. This technique was used in **Section 3.2**. The second method was used in **Section 3.3.** Here the heated (30 ^{o}C) glass substrates were held stationary under the PEDOT:PSS_{ADD} flux for a set time period at a set height of 20 cm (**Figure 2.4.b**).

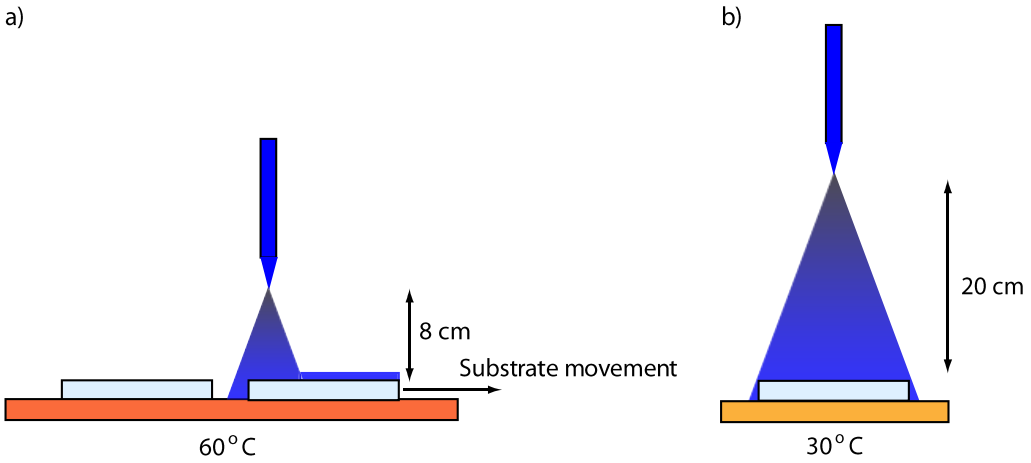

Figure 2.4 - Schematic of the different spray deposition methods a) a single pass of the substrates under the flux and b) substrates were held stationary under the flux for a set time period.

2.1.8 Vacuum deposited thin films

Organic molecular beam deposition (OMBD) is a deposition technique that is suitable for sublimable small molecule OSCs with low solubility. OMBD enables accurate control over the thin film thickness and deposition rates. The film growth was carried out under a high vacuum environment (~ 10^{-7} mbar), this assures a clean environment and reproducible conditions for thin film fabrication.

The organic material was placed in a boron nitride crucible which in turn is placed in a Knudsen cell (K-cell) (**Figure 2.5**) inside the chamber. The material in the crucible was heated (50 – 500 ^{o}C) with a resistive coil which was monitored by a thermocouple. Under growth conditions the crucible was heated to the sublimation point of the material. The resulting vapour pressure escaped through the K-cell opening as a molecular beam and the molecules are adsorbed onto the pre-cleaned substrate surface forming a layer of material.

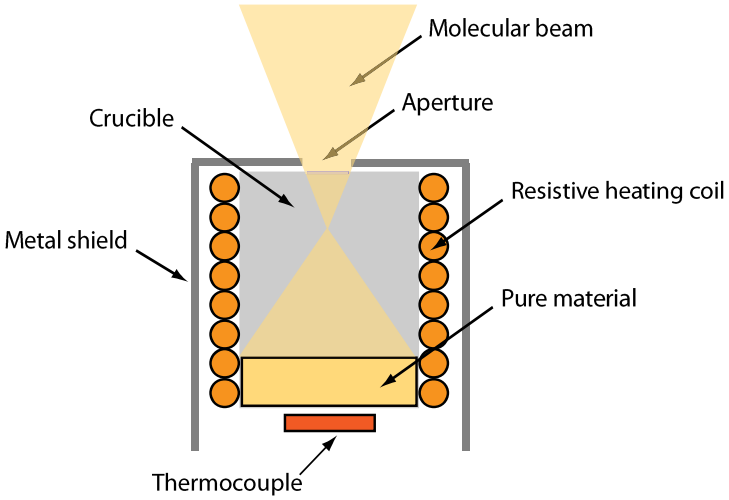

Figure 2.5 – Schematic of a K-cell.

The required pressure was obtained by a scroll pump (~ 10^{-1} mbar) followed by a cryogenic pump (< 10^{-7} mbar). The growth chamber contained three pairs of organic and three metal sources which were monitored by a total of four quartz crystal microbalances (QCMs). The temperature of each pair of K-cells was controlled using a Eurotherm 2408 with user input via a computer. The substrates sat in a substrate holder which was placed within a cassette stack. Any shadow masks required for the growth were also placed in the stack. In between layer growths the masks were manually moved using a transfer arm inside the sealed chamber. This allowed multiple device designs to be grown, including electrode deposition, without the need to break vacuum. The cassette stack was rotated during growth which allowed for homogeneous material deposition. A simplified schematic of the Kurt J. Lesker Spectros vacuum chamber is shown in **Figure 2.6**. After device or layer deposition the substrates were transferred directly into the attached nitrogen filled glove box. The oxygen and water levels were kept < 1 ppm.

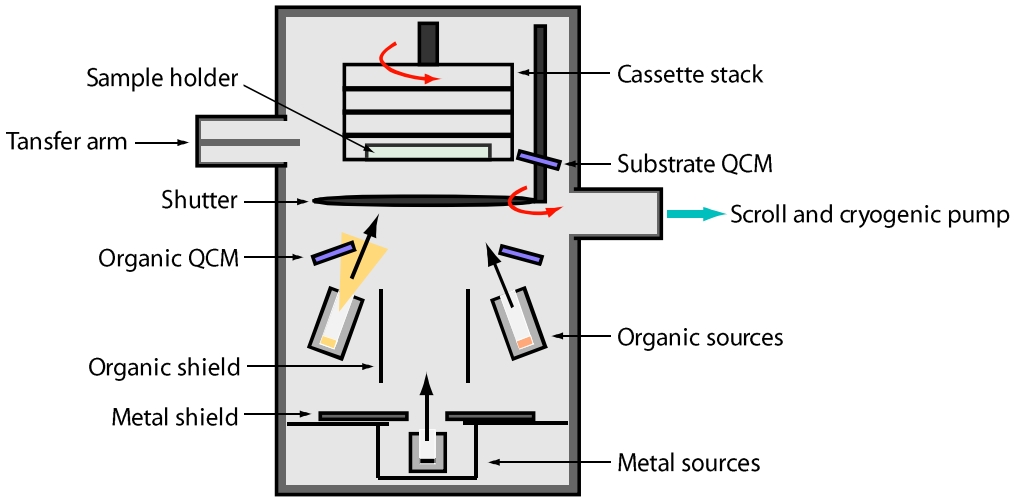

Figure 2.6 – Simplified schematic of the Kurt J. Lesker Spectros vacuum chamber.

The deposition rate was controlled by the source evaporation temperature and the film thickness was controlled by a shutter which turned the molecular beam on and off. The film thicknesses were monitored through a combination of the QCMs and *ex-situ* atomic force microscopy (AFM) (see **Section 2.2.4**) step edge measurements. Several different film thicknesses were grown and monitored by the QCMs. The samples were then taken out of the chamber and scratched multiple times with the tip of a needle through to the underlying substrate. Tapping mode AFM images were then obtained over both the substrate and organic layer as shown in **Figure 2.7**. Multiple measurements were taken at several different points on several samples for each film thickness. This was then related back to the original QCM measurement so film thickness could be monitored during film growth.

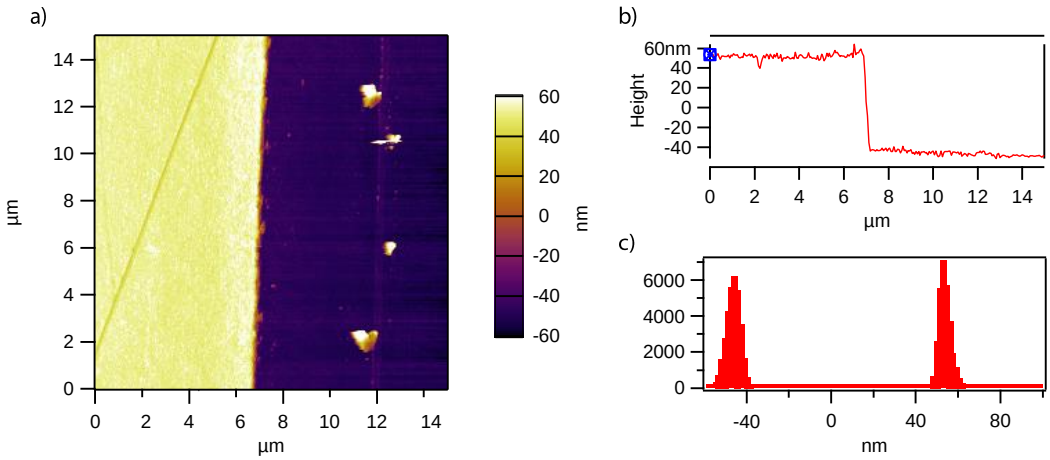

Figure 2.7 – a) AFM step edge image of a C_{60} film used to determine the actual layer thickness compared to the QCM measured thickness, b) cross-section height profile and c) histogram plot distribution of the entire image.

The metal oxide and metal electrode were deposited from high temperature metal sources. These sources consist of a heat shielded tantalum crucible heater which was resistively heated by passing high currents at low voltages. The first few nanometers of the metal layer were deposited at a slow rate to avoid the hot metal atoms damaging the underlying organic layer, the rate was then increased.

A Kurt J. Lesker Spectros vacuum chamber was used to grow all vacuum deposited layers in this work.

2.1.9 Device configuration

Four different device configurations were used in this thesis as shown in (**Figure 2.8**). The Al electrode was thermally evaporated through a custom designed shadow masks which, combined with the substrate size and the TCE pattern, determined the

active area. Silver paint was used to contact the individual pixels and TCE to a custom build J-V testing holder.

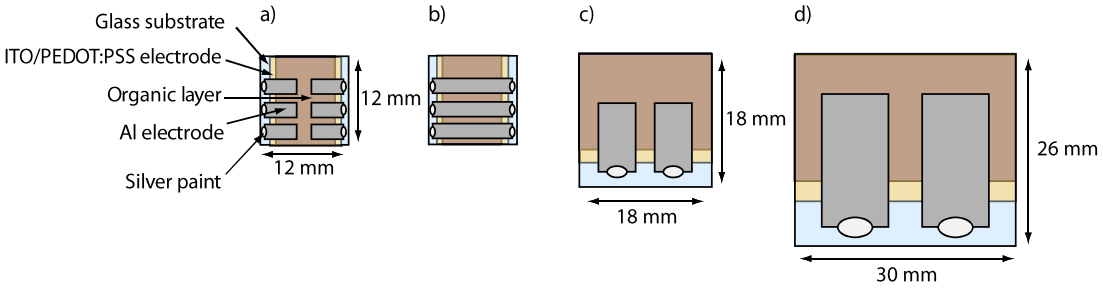

Figure 2.8 – Schematic of the different device active areas a) 0.06 cm^{-2}, b) 0.16 cm^{-2}, c) 0.30 cm^{-2} and d) 1.04 cm^{-2} used in this work.

2.2 Thin film analysis

This section briefly describes the techniques used to characterise the thin films. Details as to how specific measurements were carried out for this work are also given.

2.2.1 Sheet resistance

The sheet resistance (R_{sheet}) of the PEDOT:PSS electrodes was measured using the 4-point probe Van der Pauw method. The PEDOT:PSS solution was deposited on to 12 x 12 mm substrates and silver paint was dotted onto the four corners to provide an ohmic contact. If the contacts are labelled 1 to 4 in a clock-wise direction, as shown in **Figure 2.9**, a set current of 1 mA was applied between contacts 1 and 2 and the voltage was measured between 3 and 4. This was repeated so that the current was applied between 2 and 3 and the voltage measure across 4 and 1.

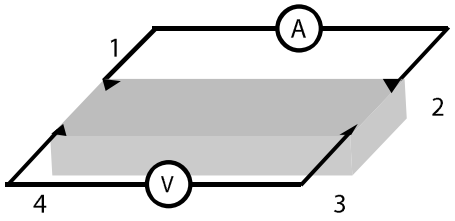

Figure 2.9 – Schematic showing the sheet resistance measurements

The R_{sheet} was calculated as shown in **Equation 2.1**:

$$R_{sheet} = \frac{\pi R}{ln2}$$ **Equation 2.1**

where *R* is the resistance determined using Ohm's law. A Keithley 2400 sourcemeter was used as the current source and a Fluke 179 True RMS multimeter was used to record the voltage.

2.2.2 Ultra-violet visible absorption spectroscopy

Ultra-violet visible absorption spectroscopy (UV-Vis) measures the absorption intensity of photons through a sample at a specific wavelength forming a spectra by measuring across a range of wavelengths. Different OSCs absorb in different parts of the UV-Vis spectrum, this technique allows the absorption to be determined. This then enables donor and acceptor materials with complementary absorption profiles to be chosen. UV-Vis technique also allows the transmittance of electrodes and interfacial layers to be determined.

The Beer-Lambert law allows the absorbance (*A*) of a material to be calculated by measuring the incident light intensity (I_0) and the reduced transmitted light intensity (*I*) (**Equation 2.2**):

$$A = log\frac{I_0}{I} = \varepsilon lc$$ **Equation 2.2**

where ε is the molar extinction coefficient of the solution, *l* is the path length and *c* is the concentration in solution. For solids the concentration is related to the molecular mass and density. A modified Beer-lambert Law can be used to measure the absorption profile for thin films, as shown in **Equation 2.3**:

$$A = log\frac{I_0}{I} = \alpha l \qquad \textbf{Equation 2.3}$$

where α is the absorption coefficient of the material which defines the molecular extinction coefficient and concentration and l is the film thickness.

All UV-Vis absorption and transmittance measurements were carried out using a Perkin-Elmer Lambda 25 Spectrometer. Whether ITO, glass or quartz were used as substrates is noted in the text for each particular section.

2.2.3 X-ray photoelectron spectroscopy

X-ray photoemission spectroscopy (XPS) is used to determine the elemental composition, the empirical formula and the chemical or electronic states of the elements making up the solid surface. XPS involves irradiating a sample with an X-ray photon of energy *hv*. If the energy is sufficient, it will result in the emission of an electron from a core level. The kinetic energy (*KE*) of the emitted electron can be measured (**Equation 2.4**) and a spectrum of intensity (expressed as counts) versus kinetic energy is obtaine,

$$KE = hv - BE - \varphi_s \qquad \textbf{Equation 2 4}$$

where *BE* is the binding energy of the atomic orbital from which the electron originates and φ_s is the spectrometer work function. The *KE, hv* and φ_s are known or are measured, therefore the *BE* can be calculated. The *BE* can be regarded as the difference in energy between the initial and final states of the electron once it has left the atom. Each element has its own unique set of binding energies which

specifically identifies the electron, both in terms of its parent element and its atomic energy level. A schematic of the process is shown in **Figure 2.10** for a model atom.

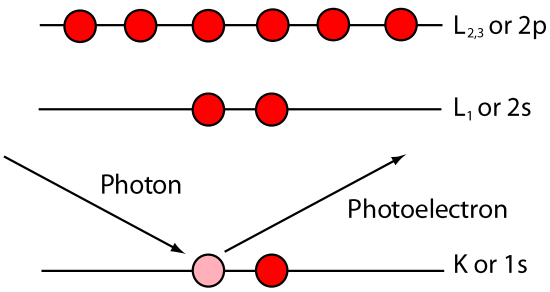

Figure 2.10 – Schematic of the XPS emission process for a model atom.

The possible relaxation processes after photoemission are Auger electron emission and fluorescent x-ray photoemission, as shown in **Figure 2.11**. In the Auger process, an outer electron relaxes into the inner vacancy leading to the emission of a secondary electron carrying off the excess energy. Fluorescent decay is the minor process, the excess energy is emitted in the form of x-ray photon.

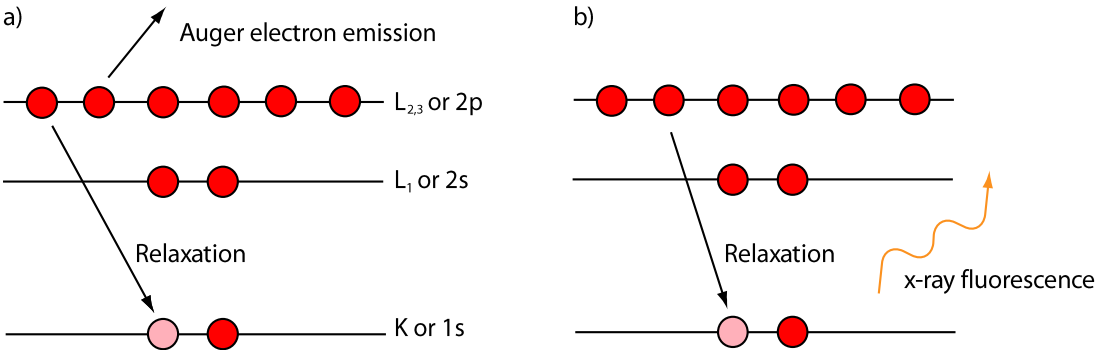

Figure 2.11 – Schematic illustration a) Auger emission and b) x-ray fluorescence.

The irradiating photons have a penetrating depth of < 10 μm which is larger than the electron escape depth (typically ~ 10 nm). Only electrons that originate within this escape depth can leave the surface without suffering any energy loss. These are the electrons that are most useful for XPS analysis. Deeper lying electrons undergo inelastic collisions and make up the background of the scan.

XPS was used to determine the surface composition of PEDOT:PSS thin films that were subjected to different DMSO treatments. All XPS measurements were taken by Dr. M. Walker using a monochromated x-ray Al K_α source (Omicron XM 1000, $h\upsilon$ = 1486.6 eV) and the photoelectrons were detected with an Omicron Sphera electron analyser in an ultra-high vacuum system with a base pressure of ~ 2×10^{-11} mbar. All XPS spectra were referenced to the C-(C,H) peak observed in the C 1s region at 284.6 eV, and fitted in CasaXPS using a Shirley background and mixed Gaussian-Lorentizan lineshapes for oxygen and sulphur. Asymmetric lineshapes were required for the PEDOT components in the S 2p region,[90] which were achieved via the use of Gaussian-Lorentzian lineshapes modified by an exponential blend on the high binding energy tail.

2.2.4 Atomic force microscopy

Atomic force microscopy (AFM) is a versatile technique that is used to probe a wide range of surface properties of many different sample types on the nanometer scale. The technique involves the interaction of intermolecular forces as the tip is brought into close proximity with the sample surface. Tips can be specially modified depending on the specific interaction of interest.

The AFM tip is attached to a cantilever which acts as a spring. When close to the sample surface the probing tip can experience attractive and repulsive forces depending on the tip-sample distance. As the tip is brought towards the surface long range attractive forces such as van der Waals interactions and electrostatic forces dominate. These forces result in the tip snapping towards the surface, bending the cantilever towards the sample. Once closer to the surface, short range repulsive forces such as hard sphere and electrostatic repulsion are dominant. These forces bend the cantilever away from the sample surface. A laser beam is reflected off the back of the cantilever and detected by a photo-detector. The amount the cantilever is deflected affects the position of the beam on the detector. A feedback loop adjusts z-piezo, which controls the position of the cantilever, to maintain a constant deflection during the scan. This is known as contact mode. Piezos also move the sample in the x and y dimensions which builds a three dimensional topographical image of the sample surface. **Figure 2.12** shows a schematic of this technique.

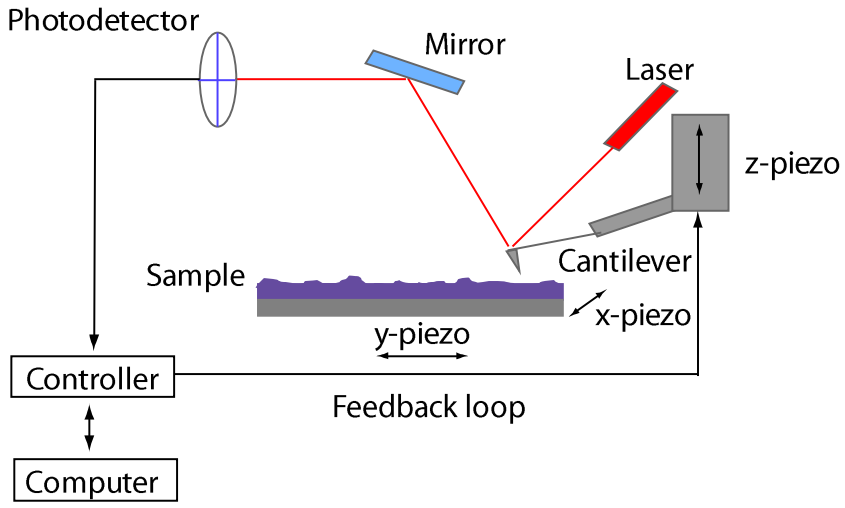

Figure 2.12 – Schematic of the AFM technique.

The second main mode of AFM operation is known as alternating contact (AC) or tapping mode. The major advantage of AC mode is that the tip only spends a small amount of time on the sample surface. This reduces the amount of damage done to the surface and is well suited to the soft polymers used in OPV devices. The tip does not apply the same frictional forces to the surface as it does in contact mode which damages the surface. In AC mode, the cantilever is oscillated close to its resonant frequency which gives a free air amplitude oscillation. As the tip is scanned over the sample, the interactions between the tip and the surface lead to a damping of the oscillation. A feedback loop controlling the z-piezo maintains the oscillation amplitude to a constant set point.

AC mode was used to take surface topography images of the PEDOT:PSS electrodes, P3HT:PCBM photoactive layer and the MoO_x and ZnO interfacial layers. It was also used in the step edge measurements used to determine the film thicknesses. All images were obtained using an Asylum Research MFP-3D (Santa Barbara, USA). Olympus AC240-TS Si cantilevers with a resonant frequency of 70 kHz and a tip radius of 9 nm were used. Asylum Research software was used for data acquisition and analysis.

Contact mode was used for all conductive AFM (CAFM) imaging. Since contact mode can be quite destructive, especially when imaging soft sample, all CAFM of the PEDOT:PSS electrodes were performed using a flexible cantilever in attractive contact mode.[128] This helped to minimise damage to the surface and keep the tip in contact with the surface. The MFP-3D was fitted with an ORCA integrated tip-holder and current preamplifier (20 nA) for CAFM measurements. For CAFM measurements, a sample bias was applied to a silver contact which was painted on

the corner of the PEDOT:PSS film via a wire from the ORCA holder. The Au/Cr coated cantilever (Olympus TR400PB, tip radius < 40 nm, spring constant 0.02 N m^{-1} acted as a nanoelectrode and formed the top contact. A 500 MΩ resistor was used to limit the current to under 20 nA. The tip was then either kept at a specific point on the surface and the current as a function of the applied bias was recorded or scanned at a set bias (given in the text) to give both topography and current distribution images. Since the PEDOT:PSS is spin coated onto an insulating substrate the flow of charge carriers is within the plane of the film and not vertical. This means that the lateral conductive pathways near to the surface of the film are probed. The same software package was used for data capture and analysis.

2.2.5 Kelvin probe

Kelvin probe is a non-contact and non-destructive technique that is used to measure the work function of a surface. This technique consists of a vibrating metal probe with a known Fermi level in close proximity to the sample. When two materials of different work functions (i.e. the sample and the metal tip) are brought together, the electrons flow from the lower φ material to the higher φ material. This creates equal and opposite surface charges within the capacitor and the Fermi levels of the two materials align. The voltage developed is known as the contact potential (V_{CPD}) and can be measured by applying an external backing potential (E_b) to one electrode with respect to the other until the charges disappear. At this point V_b equalsV_{CPD}. **Figure 2.13** shows a schematic of the technique.

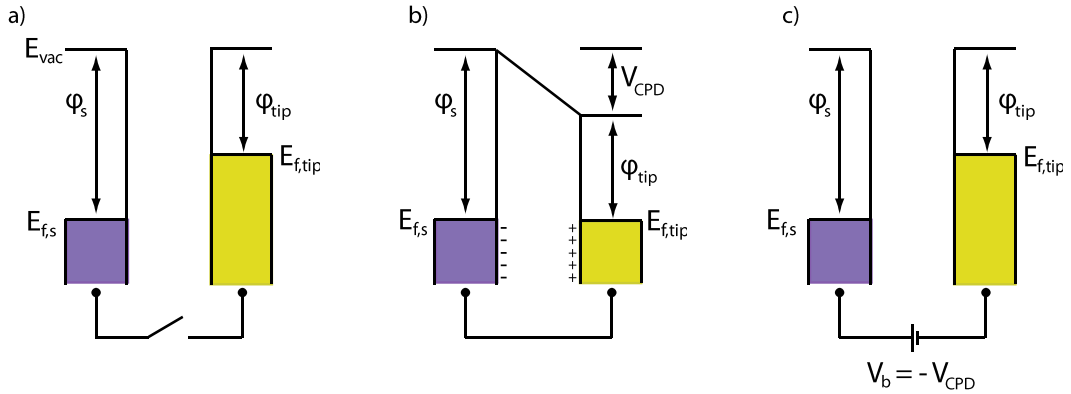

Figure 2.13 – Schematic of the Kelvin probe technique where a) two materials of different work functions are not electrically connected, b) when the materials are in electrical connection and c) when the backing potential is applied to equal the contact potential.

Oscillating one of the metal plates with respect to the other allows continuous measurements to be taken. Oscillating the probe above the sample causes the capacitance to vary and an AC current to flow through the circuit. The V_b can be adjusted so that there is no current flowing between the probe and the sample. This occurs when V_b is equal to the V_{CPD}, so the voltage across the capacitor equals zero and the electric field between the plates disappears. The work function difference between the sample and the probe are equal and opposite to the dc-potential required to nullify the voltage across the capacitor. This allows the work function to be calculated once calibrated to a known reference.

Surface work function measurements were obtained using a Kelvin probe under a N_2 atmosphere and the signal was monitored on an oscilloscope. This is a relative technique and was calibrated against a freshly cleaved highly ordered pyrolytic graphite reference, which has a known φ of 4.48 eV.

2.2.6 Contact angle

The wettability of a film surface can influence how the subsequently deposited organic layer assembles. Wetting is the capability of a liquid to maintain contact with a solid surface as a result of the intermolecular interactions when the two are brought into contact.[129] Wettability studies involve the measurement of contact angles as the primary data. The contact angle is defined as the angle (θ) which forms between the liquid-vapour, solid-vapour and liquid-solid interfaces at a three phase contact line **Figure 2.14**) and is expressed in **Equation 2.5**,

$$\gamma_{sv} = \gamma_{sl} + \gamma_{lv}\cos(\theta) \qquad \textbf{Equation 2.5}$$

where γ_{sv} is the solid-vapour interfacial free energy, γ_{sl} is the solid-liquid interfacial free energy, and γ_{lv} is the liquid-vapour interfacial tension which is often referred to as the surface tension.

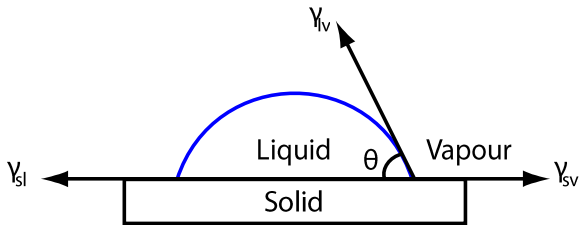

Figure 2.14 – Schematic of a sessile drop of liquid on a solid sample indicating the three-phase boundary.

Unlike the surface tension of liquids, the surface energy of solids cannot be directly measured and many semi-empirical analytical models have been developed to relate contact angle data to the solid surface free energy.[130-132] Contact angle measurements were therefore used to give an indication of any surface energy

differences between the PEDOT:PSS thin film surfaces. A Krüss drop shape analyser system DSA100 with tilting table was used to carry out contact angle measurements under an ambient atmosphere. The measurements consisted of dropping ~ 10 μl of water from a computer controlled syringe on to the film surface and a camera captured an image of the drop. The resulting angle between the tangent to the drop surface at the point of contact with the solid and the horizontal sample surface was measured to give the static contact angle (**Figure 2.14**). The angles were measured using software that was integrated with the contact angle system. Several samples of each PEDOT:PSS dispersion were spin coated and multiple measurements were carried out on each sample.

2.3 Device analysis

This section describes how the OPV devices were characterised through analysis of the current density - voltage (J-V) characteristics under dark conditions and while under simulated solar illumination. External quantum efficiency (EQE) measurements were used to measure the wavelength dependent photocurrent generation which allowed further insight into current generation.

2.3.1 The solar spectrum

A standardised light source is needed to reliably compare the performance of OPV devices fabricated both within and between research groups. It is impractical to use direct sunlight due to continually varying changes in the weather conditions and light intensity. Instead, solar simulators are used within the laboratory which allows for consentient OPV device testing at all times.

Blackbody radiation (**Equation 2.6**) is the best way to describe the energy radiating from the sun. A blackbody is an ideal radiation absorber and at high temperatures it emits radiation with a spectral shape that is dependent on temperature,

$$E\,(\lambda, \mathrm{T}) = \frac{2\pi hc^2}{\lambda^5(\exp\left(\frac{hc}{k\lambda \mathrm{T}}\right)-1)} \qquad \textbf{Equation 2 6}$$

where E (λ,T) is the irradiance, λ is the wavelength, h *is* Planck's constant, k is Boltzman's constant, c is the speed of light and T is the blackbody temperature. The solar spectrum can be best modelled by a blackbody at 6000 K (**Figure 2.15**). The

spectral features originate from the absorption and scattering of photons as they pass through the Earth's atmosphere.

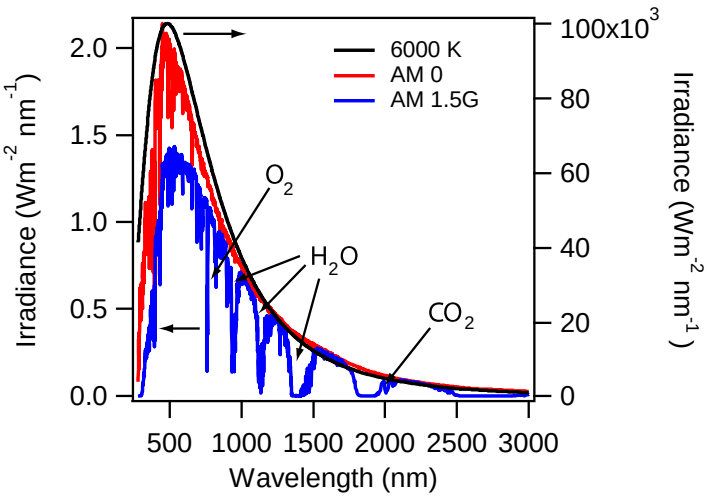

Figure 2.15 – Comparison of blackbody emission at 6000 K and the spectral profile of AM 0 and AM 1.5G solar spectrum with the main atmospheric absorption regions labelled.

The path length of the solar radiation through the atmosphere is defined as an air mass (AM) and is expressed in **Equation 2.7**:

$$AM = \frac{1}{cos\varphi} \qquad \textbf{Equation 2.7}$$

where φ is the incident angle. The extra-terrestrial spectra is defined as AM 0. AM 0 has a light intensity of 135 mW cm^{-2} and because the radiation does not pass through the atmosphere there are no spectral features. The shortest path length through the atmosphere is at AM 1, when the sun is directly overheard and φ = 0 °. AM 1.5 and AM 2 have incident angles of 48.2 ° and 60.1 ° respectively and have paths that are 1.5 and 2 times the length of AM 1, as shown in **Figure 2.16**. AM 1.5G has a light intensity of 100 mW cm^{-2} and is the accepted PV device testing

standard. 'G' represents the global spectra which is a combination of diffuse and direct radiation which includes scattering from atmospheric molecules.

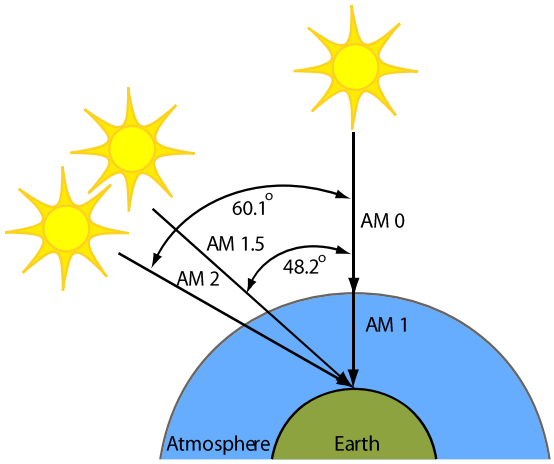

Figure 2.16 – Schematic of the AM dependence on the angle of the sun to a single point of the Earth's surface.

All OPV devices in this thesis were measured using the AM 1.5G spectra which was simulated using a Newport Oriel solar simulator with a xenon lamp light source with an AM 1.5G filter. The output was calibrated to 1 sun intensity (100 mW cm^{-2}) using a calibrated Fraunhofer calibrated PVM 482 photodiode with KG-5 filter.

2.3.2 J-V characteristics

OPV devices were characterised by measuring the J-V behaviour in the dark and under simulated solar illumination. The measurements involved sweeping an applied bias across the operational range and measuring the current density produced. Under dark conditions an ideal device should show diode-like behaviour, where no current is produced under negative bias followed by an exponential

increase under positive bias. When the device is illuminated, the resulting curve is a combination of the dark curve and an offset from the photocurrent generated in the device. Typical J-V dark (dashed lines) and light (solid lines) curves for a regular OPV device are shown in **Figure 2.17.a**. The key device parameters, open circuit voltage (V_{oc}), short circuit current density (J_{sc}) and fill factor (FF), are found in the fourth quadrant of the J-V plot. These are shown in **Figure 2.17.b.** The voltage (V_m) and current density (J_m) measured at the maximum power point (P_m) are also labelled. These parameters are found in the second quadrant for inverted devices.

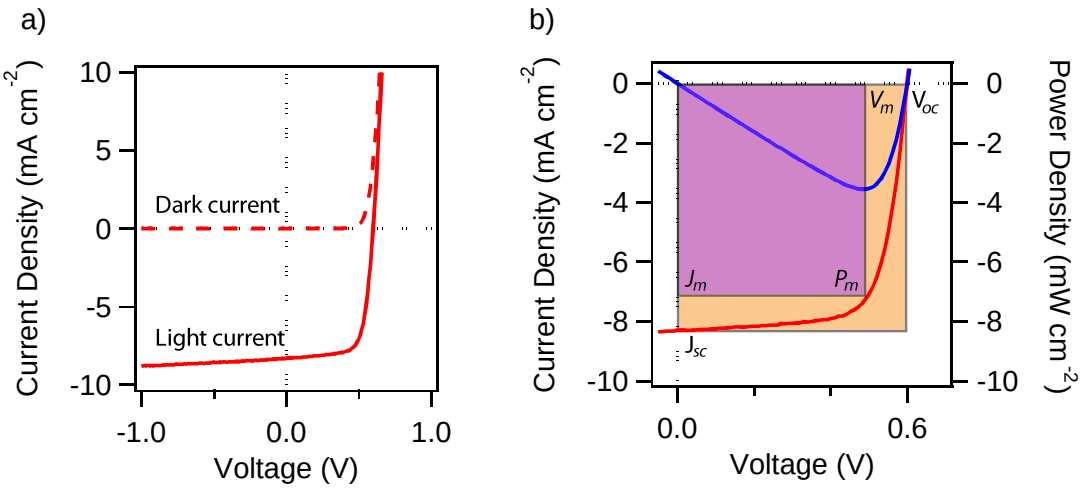

Figure 2.17 – a) Typical J-V plots in the dark (dashed lines) and light (solid lines) for a regular OPV device and b) the fourth quadrant showing the key device parameters and the device power density.

The equivalent electric circuit diagram of a device is shown in **Figure 2.18**. The device is represented by a current source (I_L) in parallel with an ideal diode (D) and the parasitic resistances the series and shunt resistances are represented by R_s and R_{sh} respectively. The load resistance is denoted as R_l.

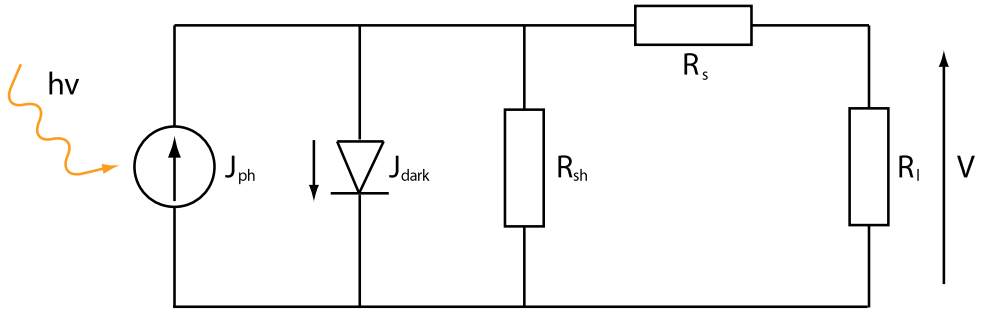

Figure 2.18 – The equivalent circuit diagram for an OPV device.

As shown in **Figure 2.17**, many parameters can be extracted from the J-V plots which allow device comparison. The J_{sc} is the photocurrent density at zero applied bias (V = 0) and is the equivalent of when R_l = 0 Ω. It is a measure of the photocurrent collected at the electrodes and so is dependent on the absorption, excition dissociation, charge transport and collection in the device. The V_{oc} is the voltage generated across the device when the load resistance is infinitely high, R_l = ∞. It occurs at the bias when the photocurrent is equal to the current flow in the opposing direction which results in no net current flow. The V_{oc} is thought to be dependent on the energy level difference between the HOMO of the donor and the LUMO of the acceptor when there are ohmic contacts with the electrodes.

The P_m is the maximum power output and is the maximum product of the current density (J_m) and voltage (V_m) of the device. These parameters are used to define the *FF* which is the ideality factor for the shape of J-V curve. The *FF* is determined by the ratio between the operational maximum power output and the theoretical maximum power output which is obtained by the product of the V_{oc} and J_{sc}. This is shown in **Equation 2.8** and graphically as the ratio between the boxes in **Figure**

2.17.b. The *FF* affects the shape of the J-V curve, the higher the *FF* the more 'square' the curves are.

$$FF = \frac{J_m V_m}{J_{sc} V_{oc}} \qquad \textbf{Equation 2 8}$$

The PCE is the overall efficiency of light conversion into energy. It is defined as the ratio of the maximum power output to the incident radiation power intensity (P_{imc}) as shown in **Equation 2.9**:

$$PCE = \frac{P_m}{P_{inc}} = \frac{V_m J_m}{P_{inc}} = \frac{V_{oc} J_{sc} FF}{P_{inc}} \qquad \textbf{Equation 2.9}$$

The R_s and R_{sh} are parasitic resistances which decrease the FF and therefore decrease the overall PCE. The R_s can be considered as a resistance in series between the current source and the load. It is composite of the photoactive layer, interfacial layer, the electrode, and any contact and interconnecting resistances.[133] Ideally the $R_s = 0\ \Omega$ and any increase in resistance leads to a decrease in the slope under positive bias and therefore a loss in FF (**Figure 2.19**.**a**) The R_{sh} can be considered as a resistance parallel to the load. It represents device leakages such as pinholes which allow parasitic current to move directly from one electrode to the other and recombination of charges.[134] In an ideal device $R_{sh} = \infty\ \Omega$ and any decrease leads to an increase in the slope under negative bias and a loss in *FF* (**Figure 2.19**.**b**).

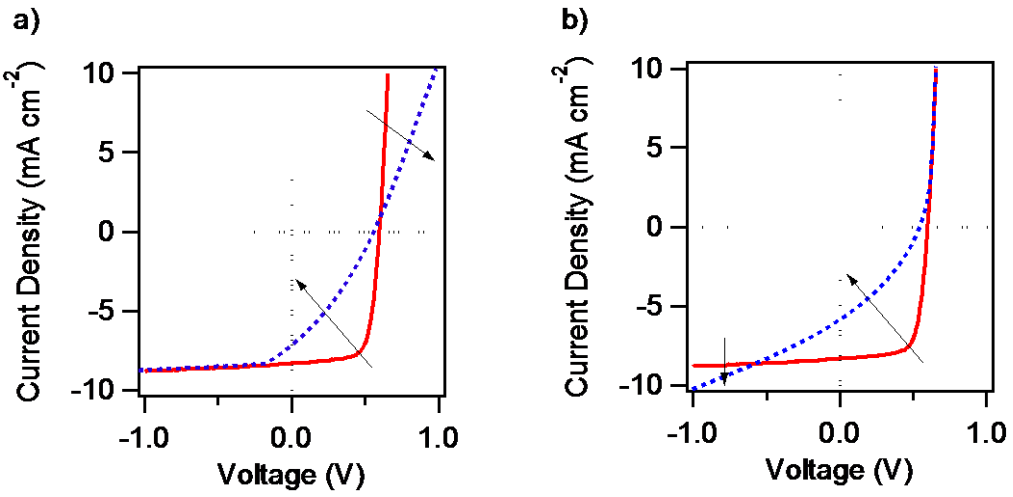

Figure 2.19 – The effect of a) increasing R_s and b) decreasing R_{sh} on the J-V curve. The arrows indicate the reduction on *FF*.

All J-V measurements were performed using a computer controlled Keithley 2400 sourcemeter running a custom LabView program written by Dr. P. Sullivan. The devices with 0.06 cm^{-2} and 0.16 cm^{-2} were loaded into a custom built device test holder which was placed in the centre of the calibrated simulated light beam. The larger area devices were connected using crocodile clips.

2.3.3 External quantum efficiency

External quantum efficiency (EQE) measurements are used to gain further understanding of how the individual photoactive components contribute to the photocurrent. It indicates how much each material contributes to the J_{sc} obtained for the device. The EQE is the ratio of the charge generated by the device for each incoming photon at a specific wavelength (λ) as shown by **Equation 2.10**:

$$EQE\ (\lambda) = \frac{J_{sc}(\lambda)}{qN(\lambda)} \qquad \textbf{Equation 2.10}$$

where q is the elementary charge and $N(\lambda)$ is the monochromatic incident photon flux density. Experimentally, the device EQE (EQE_{OPV}) is calculated by comparing the J_{sc} of the device ($J_{sc}(\lambda)_{\mathrm{OPV}}$) with a silicon diode that has a known EQE response (EQE_{OPV}) using **Equation 2.11**:

$$EQE_{OPV} = \frac{EQE_{ref} \times J_{sc}(\lambda)_{OPV}}{J_{sc}(\lambda)_{ref}} \qquad \textbf{Equation 2.11}$$

Where ($J_{sc}(\lambda)_{ref}$) is the current generated by the reference diode.

In this work, a Sciencetech solar simulator with a xenon arc lamp with a PTI monochromator was used as the white light source. The monochromatic light was chopped at 510 Hz and calibrated using a Newport 818-UV Si photodiode. The current was measured using a current-voltage amplifier (Femto DHPCA-100) and a lock-in amplifier (Stanford Research SR 830 DSP) connected to a computer. Data collection was controlled by a LabView program written by Dr. P. Sullivan.

Chapter 3. PEDOT:PSS as an alternative electrode to ITO

OPV devices are attracting increasing interest as a promising renewable energy source. The ability to solution process the photoactive layers is a major advantage, providing the potential for high-throughput, low-cost processing on large-area and flexible substrates. Spin coating, the most common solution processing technique used to fabricate OPV devices, is not well-suited to the commercial scale up of devices. Spray deposition, however, is drawing attention as a low cost method of OPV fabrication and is already a well established industrial technique.[126]

In addition to reducing the energy requirements needed for production, the cost of materials used in OPV devices also needs to be considered. A recent study by Azzopardi *et. al*. attributed 38 – 51 % of the total cost of a flexible OPV device to the TCE, ITO.[79] This high cost, combined with the limited energetic compatibility with frequently used organic materials, poor flexibility and tendency to crack and/or delaminate, has resulted in a strong interest to find an alternative material for use as the TCE.

This chapter starts by considering the use of highly conductive Clevios PH1000 PEDOT:PSS as a possible alternative to ITO as the TCE. Two different DMSO treatments to improve the conductivity of spin coated PEDOT:PSS thin films were characterised. The DMSO was either added to the PEDOT:PSS solution (PEDOT:PSS_{ADD}) or the pre-formed PEDOT:PSS film was immersed in DMSO for a predetermined time (PEDOT:PSS_{IMM}). The DMSO treated PEDOT:PSS electrodes

were directly compared when used in P3HT:PCBM OPV devices. PEDOT:PSS_{ADD} electrodes were then used to compare spin coating to spray deposition, a technique that more readily lends itself to roll-to-roll processing. Both techniques were utilised in a CuPc/C_{60} small molecule OPV device in order to investigate whether spray deposition is a viable technique to fabricate PEDOT:PSS_{ADD} electrodes. Finally, larger area spray deposited PEDOT:PSS electrodes were used in the small molecule SubPc/C_{60} OPV device structure.

3.1 Comparison of spin coated DMSO treated PEDOT:PSS electrodes

Despite being considered conductive, the conductivity of PH1000 PEDOT:PSS is much lower than that of ITO and many different methods to improve it have been reported in literature. The use of high boiling point organic solvents such as DMSO have been shown to reliably increase the conductivity of PEDOT:PSS thin films.[96, 99, 100, 113, 115] These solvents can be used in a number of different ways. This section focuses on directly comparing two of these preparation methods - (i) DMSO (5 vol-%) was added directly to the PEDOT:PSS solution (PEDOT:PSS_{ADD}) or (ii) a pre-formed PEDOT:PSS film was immersed in DMSO for 30 minutes (PEDOT:PSS_{IMM}). Both DMSO treated PEDOT:PSS thin films were characterised and compared to untreated PEDOT:PSS (PEDOT:PSS_{UT}) films. A P3HT:PCBM photoactive system with an active area of 0.06 cm^2 was then used to study the effect both treatments had on the resulting OPV device performance. The DMSO treated PEDOT:PSS electrodes were also compared to the more commonly used ITO/PEDOT:PSS_{HTL} electrode.

3.1.1 Transmittance and sheet resistance

The PEDOT:PSS_{UT}, PEDOT:PSS_{ADD} and PEDOT:PSS_{IMM} solutions were spin coated onto glass substrates at 2000 RPM. The R_{sheet} value for the PEDOT:PSS_{UT} electrodes was high at over 200,000 Ω sq^{-1}. Using DMSO, the R_{sheet} decreased to 208 Ω sq^{-1} (standard deviation (σ) = 24 Ω sq^{-1}) and 214 Ω sq^{-1} (σ = 39 Ω sq^{-1}) for PEDOT:PSS_{ADD} and PEDOT:PSS_{IMM} respectively. These values are just one order

of magnitude greater than that of ITO (15 Ω sq^{-1}). Both PEDOT:PSS_{UT} and PEDOT:PSS_{ADD} electrodes produced films with a similar film thickness of 90 nm and 86 nm respectively. However, a 36 % decrease in film thickness was seen for PEDOT:PSS_{IMM} electrodes (58 nm) which was consistent with the 30 % decrease seen by Kim *et. al.* and the 27 – 39 % decrease seen by Kim *et. al.* after immersing PEDOT:PSS films in EG.[114, 115]

Neither DMSO treatment resulted in a significant change in transmittance across the visible region, indicating very little PEDOT was removed, as shown in **Figure 3.1.a**. ITO with a PEDOT:PSS hole transport layer (PEDOT:PSS_{HTL}) is also included for a comparison. The PEDOT:PSS_{HTL} has a film thickness of 37 nm. **Figure 3.1.b** shows the absorption peak at 225 nm attributed to the absorption from the phenyl rings in the PSS.[103] A similar absorption peak is seen for both PEDOT:PSS_{UT} and PEDOT:PSS_{ADD} electrodes, but a large decrease is seen for PEDOT:PSS_{IMM} electrodes. This coupled with the film thickness measurements indicate that immersing a PEDOT:PSS film in DMSO removes a large amount of PSS.

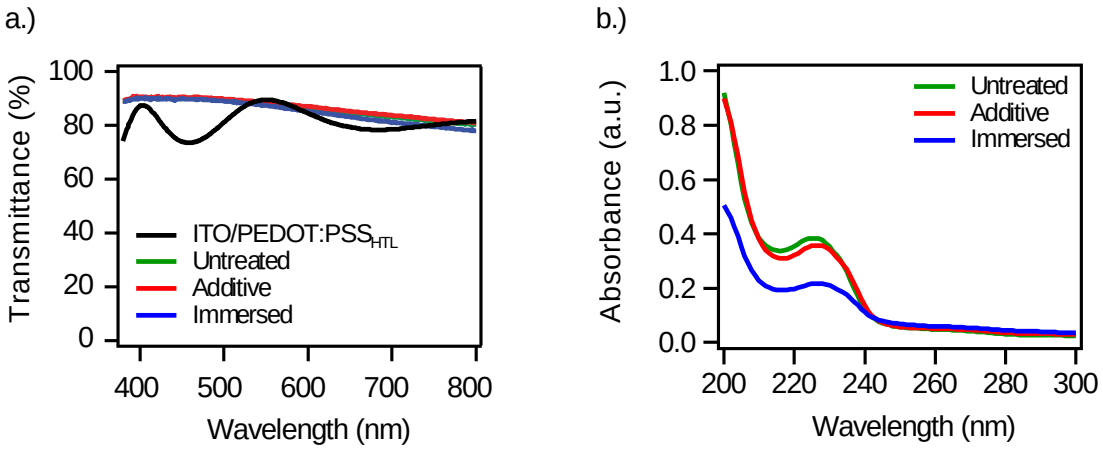

Figure 3.1 – a) Transmission spectra of ITO/PEDOT:PSS$_{HTL}$, PEDOT:PSS$_{UT}$, PEDOT:PSS$_{ADD}$ and PEDOT:PSS$_{IMM}$ electrodes and b) absorbance of the PEDOT:PSS electrodes between 200 – 300 nm. The PEDOT:PSS films were spin coated onto quartz substrates.

3.1.2 XPS

XPS was used to investigate the near surface PSS content in relation to PEDOT for each PEDOT:PSS electrode. The S 2p and O 1s regions for the PEDOT:PSS$_{UT}$ electrodes are shown in **Figure 3.2.a** and **b** respectively. The peaks were deconvolved following previous work by Greczynski *et. al.*[90, 135] The S 2p spectra for PEDOT:PSS$_{UT}$ films shows three main chemical species, two that were assigned to the PSS component (**Figure 3.2.d** and **e**) and one to PEDOT (**Figure 3.2.f**), allowing the near surface PEDOT-to-PSS ratio to be determined. The lower binding energy peaks at 164.0 eV and 165.1 eV correspond to the spin-orbit contributions from the S $2p_{3/2}$ and S $2p_{1/2}$ from the PEDOT. Asymmetric tails are seen on the higher binding energy side of the two PEDOT components due to the cationic charge of the PEDOT:PSS^{+} being delocalised over several adjacent thiophene rings. The broad higher binding energy peak near 168 eV was assigned to the PSS sulphur

atoms and can be split into PSSH and PSS^--Na^+ components. The higher energy spin orbit component (yellow lines) is assigned to the PSSH components with the S $2p_{3/2}$ peak at 169.0 eV and the S $2p_{1/2}$ peak at 170.2 eV. The lower binding energy component corresponds to the PSS^--Na^+ (green lines) with the S $2p_{3/2}$ peak at 168.0 eV and the $S2p_{1/2}$ peak at 169.2 eV. The O 1s spectra (**Figure 3.2.b**), again allows the PEDOT and PSS components to be resolved. The peak at 533.3 eV is due to the oxygen atoms in the dioxyethylene bridge in PEDOT. The two PSSH components can be seen (yellow lines), the major peak at 532.1 eV corresponds to the oxygen atoms in the sulfonic groups and the broader minor peak at 533.4 eV originates from the hydroxyl oxygen atoms. The intensity ratio of 2:1 agrees with the chemical composition of PSSH. The peak due to the PSS^--Na^+ component is seen at 531.6 eV. The other peaks at higher binding energies are assigned as carbon monoxide and residual water contaminants.

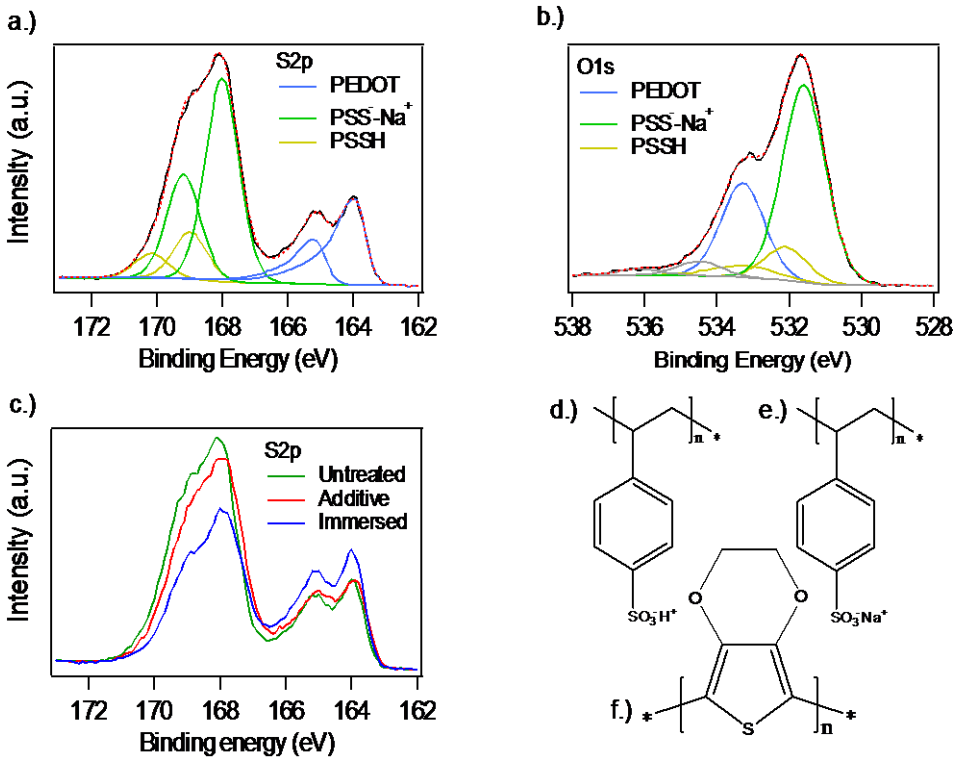

Figure 3.2 – XPS spectra of a) S 2p and b) O 1s spectra of PEDOT:PSS_{UT} electrodes and c) S 2p spectra of PEDOT:PSS_{UT}, PEDOT:PSS_{ADD} and PEDOT:PSS_{IMM} electrodes and the chemical structures of d) PSS^--Na^+, e) PSSH and f) PEDOT.

The PEDOT-to-PSS ratio obtained from the S 2p and the O 1s spectra for the PEDOT:PSS_{UT} electrodes were in good agreement at 1:2.4 and 1:2.6 respectively. The peak deconvolutions were kept constant for both PEDOT:PSS_{ADD} and PEDOT:PSS_{IMM} electrodes, to give average ratios of 1:2.2 and 1:1.5 respectively, as can be seen in **Figure 3.2.c** and **Table 3.1**. This corresponds to average decreases of 12 % and 40 % in the PSS component on the near-surface region compared to PEDOT:PSS_{UT} films for PEDOT:PSS_{ADD} and PEDOT:PSS_{IMM} electrodes respectively. The information depth was estimated to be ~ 8 nm, given the inelastic mean free pathway of 27 Å for S 2p electrons through the material, and the 90º take

off angle (with respect to the surface plane) employed.[136] This complements the UV-Vis spectra (**Figure 3.2.b**), showing that a post-treatment immersion with DMSO results in a larger decrease in the surface PSS content than is seen for PEDOT:PSS_{ADD} electrodes.

Table 3.1 – Relative ratios between chemical species in PEDOT:PSS_{UT}, PEDOT:PSS_{ADD} and PEDOT:PSS_{IMM} electrodes.

	PEDOT-to-PSS ratio	
Electrode	S2p	O1s
PEDOT:PSS_{UT}	1:2.4	1:2.6
PEDOT:PSS_{ADD}	1:2.0	1:2.4
PEDOT:PSS_{IMM}	1:1.2	1:1.7

3.1.3 CAFM

CAFM is a powerful technique which allows for measuring the sample topography while simultaneously probing the local electrical properties. All CAFM here was performed using contact mode. The images were taken using a flexible cantilever with a spring constant of 0.02 N m^{-1} and in attractive contact mode rather than repulsive contact mode. This helped to minimise damage to the relatively soft sample and helped keep the AFM tip on the film surface. However, due to the sensitive nature of the feedback conditions, care is needed to ensure the tip maintains contact with the PEDOT:PSS surface.[128]

Since excess PSS is reported to segregate to the top of PEDOT:PSS$_{UT}$ thin films,[135, 137] CAFM was used to investigate how this segregation effects the homogeneity of conductivity on the PEDOT:PSS electrode surfaces. The PEDOT:PSS$_{UT}$ electrode surface (**Figure 3.3**) predominantly consists of non-conducting regions with randomly scattered conductive grains 12 - 26 nm in diameter, as previously reported.[138-140,] The conductive regions (**Figure 3.3.d**) are assigned to surface regions of PEDOT, with the insulating areas attributed to PSS. The conductive regions appear to be independent from the topography, showing that PEDOT does not follow any topological features, and is randomly distributed during film formation (**Figure 3.3.c**).

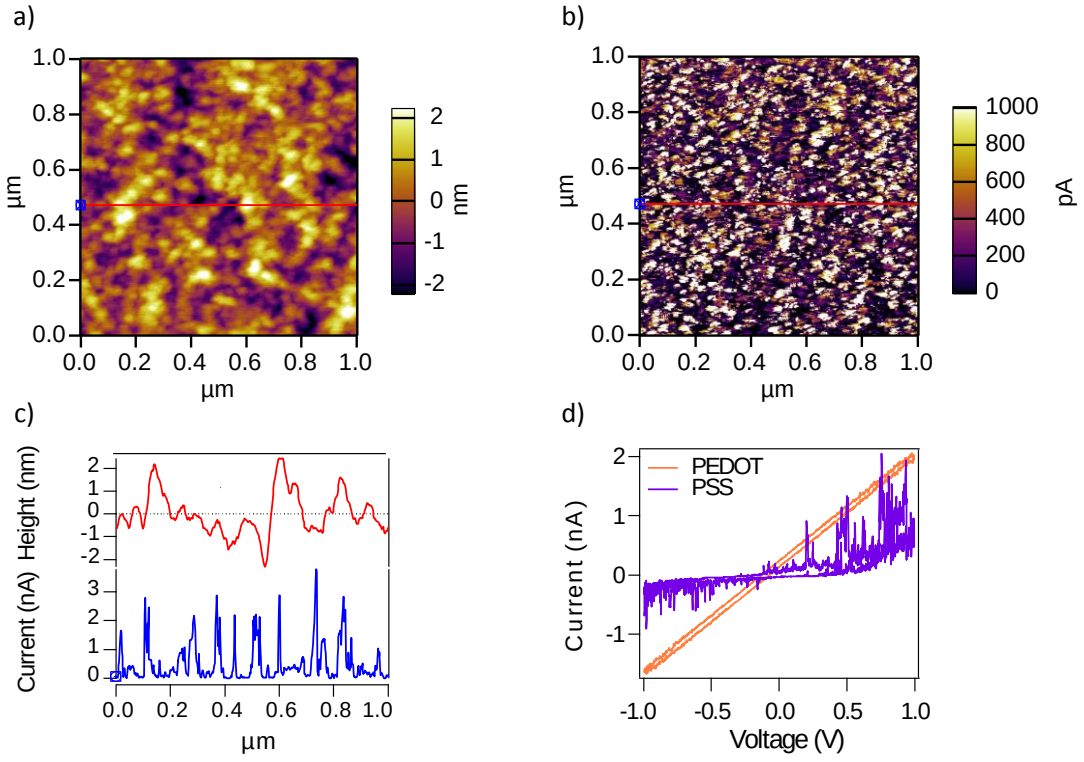

Figure 3.3 – CAFM a) topography and b) current distribution map at +320 mV of PEDOT:PSS$_{UT}$ electrode. The cross section of topography and current distribution maps are shown in c) and d) shows the IV curves of conductive regions (orange) and non-conductive regions (purple).

Figure 3.4 shows representative examples of simultaneously obtained CAFM topography (**Figure 3.4.a - c**), current distribution maps (**d - f**) and histograms (**g – i**) of the PEDOT:PSS_{UT}, PEDOT:PSS_{ADD} and PEDOT:PSS_{IMM} electrodes. All these images of spin coated PEDOT:PSS films were imaged on the same day using the same CAFM tip. PEDOT:PSS_{UT} electrodes have a smoother surface topography with a surface roughness of 0.9 nm compared to PEDOT:PSS_{ADD} and PEDOT:PSS_{IMM}, which both have a slightly larger surface roughness of 1.2 nm. However, a significant difference in the current distribution maps (**Figure 3.4.d – f**) is seen between the PEDOT:PSS electrodes, which is further illustrated by the current distribution histograms (**Figure 3.4.g – i**) for each image.

When compared to PEDOT:PSS_{UT} electrodes, the surface of PEDOT:PSS_{ADD} and PEDOT:PSS_{IMM} electrodes are covered by a significantly higher proportion of conductive regions. The difference in conductivity can be more easily seen from the current distribution histograms. **Figure 3.4.d** and **g** show that the vast majority of the PEDOT:PSS_{UT} surface is non-conductive, with a large peak at 0 nA in the current distribution (**Figure 3.4.g**), with only a small proportion of the electrode surface showing conductive character. For the PEDOT:PSS_{ADD} electrodes (**Figure 3.4.e** and **h**), the current distribution map and histogram shows a distribution of conductivities. The proportion of non-conductive regions is greatly reduced to less than a third of that of PEDOT:PSS_{UT}. A new dominant peak at 0.64 nA can be seen due to the conductive nature of the surface. This peak represents the saturation current of the measurement and does not represent a quantitative value but rather gives a qualitative indication of areas of high conductivity on the film surface. However, a significant part of the electrode surface shows an intermediate

conductive behaviour between the peak at 0 nA and the peak at 0.64 nA, which is not fully insulating, nor as conductive as other regions. The PEDOT:PSS$_{IMM}$ electrodes display a peak at 0.64 nA in the current distribution histogram **Figure 3.4.i**) of a far greater magnitude, with no discernible peak at 0 nA. The current distribution map (**Figure 3.4.f**) also indicates the electrode has the largest coverage of conductive regions. The intermediate behaviour, shown by the PEDOT:PSS$_{ADD}$ electrodes, is not seen for PEDOT:PSS$_{IMM}$ electrodes with the majority of the electrode surface displaying conductive behaviour.

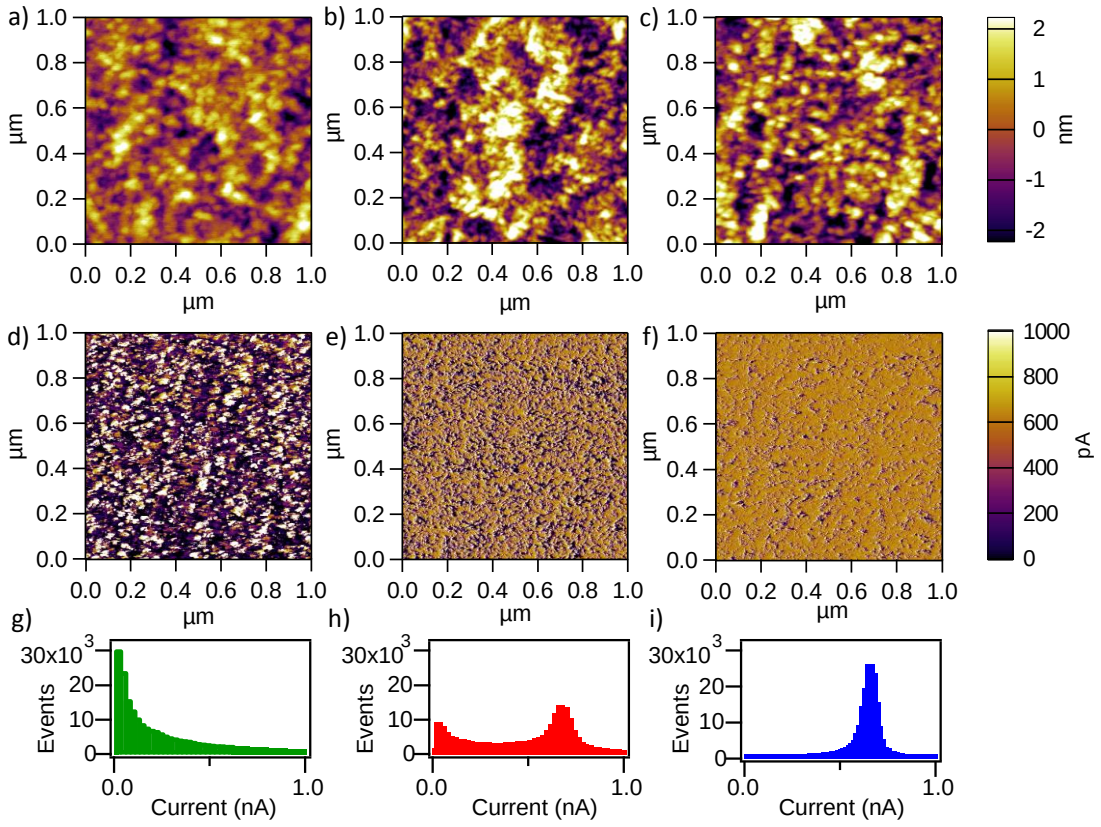

Figure 3.4 – CAFM topography (a – c), current distribution maps at + 320 mV (d – f) and current distribution histograms (g – i) for PEDOT:PSS$_{UT}$ (a, d and g), PEDOT:PSS$_{ADD}$ (b, e and h) and PEDOT:PSS$_{IMM}$ (c, f and i) electrodes.

Similar to observations made by Pingree *et. al.* the conductive pathways are polarity independent indicating both holes and electrons can be transported by the PEDOT:PSS electrode.[138] **Figure 3.5** shows a representative current distribution map of a PEDOT:PSS$_{ADD}$ film where the tip has an applied bias that is increased from -1 V to +1 V throughout the duration of the scan.

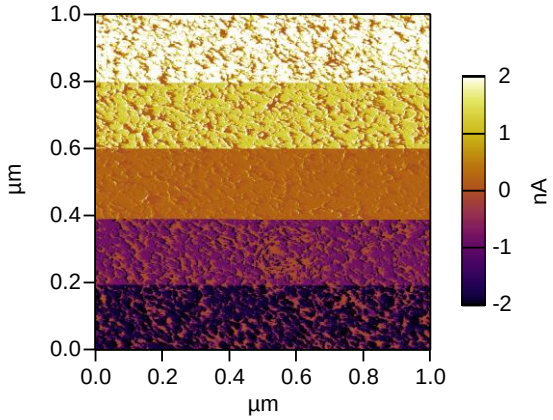

Figure 3.5 – CAFM current distribution map for a change in applied bias from -1 V (top) to +1 V (bottom) for a PEDOT:PSS$_{ADD}$ film.

3.1.4 Surface energy

The work function of the PEDOT:PSS electrodes was measured using Kelvin probe under a nitrogen environment. The work function decreased from 5.2 eV for PEDOT:PSS$_{UT}$ and PEDOT:PSS$_{ADD}$ electrodes to 4.9 eV for PEDOT:PSS$_{IMM}$ electrodes. This decrease in work function is consistent with the removal of PSS from the PEDOT:PSS film surface due to the removal of the surface dipole, as shown previously by Nardas *et.al.*[104]

The change in surface composition also resulted in a change in the surface energy between PEDOT:PSS$_{ADD}$ and PEDOT:PSS$_{IMM}$ electrodes, as shown in **Figure 3.6**.

The PEDOT:PSS_{ADD} electrodes have a more hydrophilic surface with a contact angle of 27 ^{o} whereas PEDOT:PSS_{IMM} electrodes, with a lower concentration of PSS on the surface, have a higher contact angle of 59 ^{o}. The surface energy of the substrate has been shown to affect the segregation of the subsequently spin coated polymer blends, with a lower surface energy substrate favouring the lower surface energy blend component because the free energy is minimised.[141]

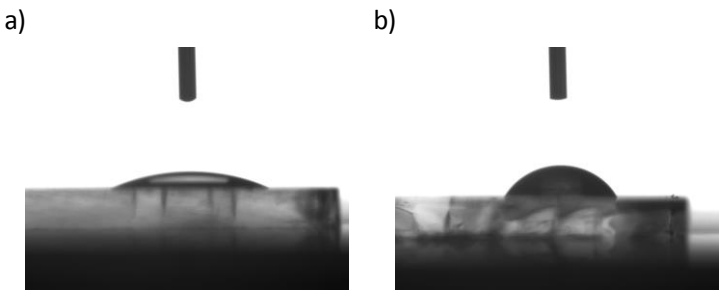

Figure 3.6 – Contact angle images for a) PEDOT:PSS_{ADD} and b) PEDOT:PSS_{IMM} electrodes.

3.1.5 Device comparison

The three PEDOT:PSS electrodes were directly compared to an ITO/PEDOT:PSS_{HTL} reference in OPV devices with the following architecture: electrode/P3HT:PCBM/BCP/Al. This extensively studied BHJ system provides a reliable indication of OPV device performance and the feasibility of using the different PEDOT:PSS electrodes as a replacement for ITO. The film thicknesses of the ITO/PEDOT:PSS_{HTL}, PEDOT:PSS_{UT}, PEDOT:PSS_{ADD} and PEDOT:PSS_{IMM} electrodes were first separately optimised by varying the spin speed during spin coating to give maximum device performance before direct comparison. **Table 3.1** displays the spin speeds and film thicknesses for the optimised electrodes.

Table 3.2 – The spin speeds and film thicknesses of PEDOT:PSS films used as electrodes in P3HT:PCBM devices. The film thickness for ITO/PEDOT:PSS_{HTL} corresponds to the thickness of the PEDOT:PSS_{HTL} layer only.

Electrode	Spin speed (RPM)	Film thickness (nm)
ITO/PEDOT:PSS_{HTL}	3000	37
PEDOT:PSS_{UT}	2000	90
PEDOT:PSS_{ADD}	3000	68
PEDOT:PSS_{IMM}	2000	58

The annealing process was kept the same for all electrodes; after spin coating with the appropriate PEDOT:PSS dispersion the substrates were annealed at 110 ^{o}C for 20 minutes. The films were then allowed to cool before being immersed in DMSO or being transferred into the glovebox. Multiple devices with a 0.06 cm^2 active area were made and tested over a five month period and the averaged J-V curves are shown in **Figure 3.7**.

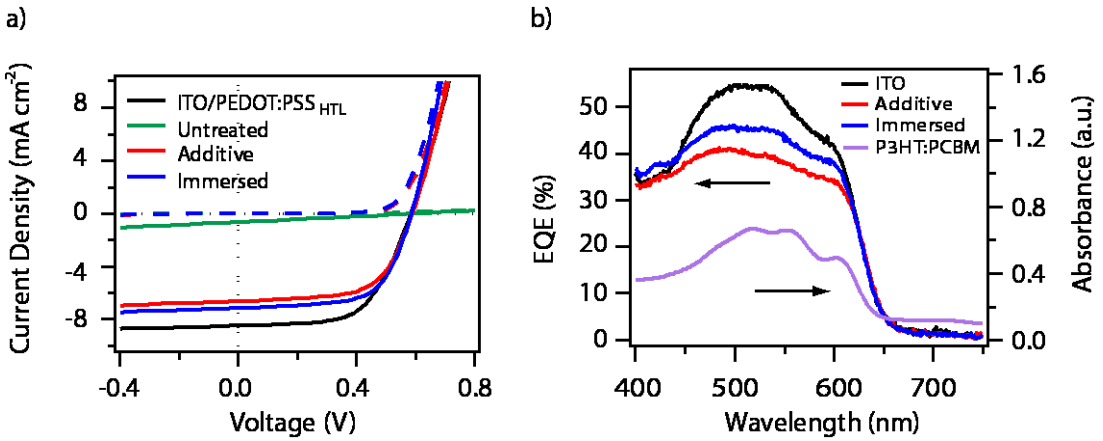

Figure 3.7 – a) Averaged J-V curves under illumination (solid lines) and in the dark (dashed lines) for P3HT:PCBM OPV devices with ITO/PEDOT:PSS$_{HTL}$, PEDOT:PSS$_{UT}$, PEDOT:PSS$_{ADD}$ and PEDOT:PSS$_{IMM}$ electrodes and b) the corresponding EQE spectra (left axis) and P3HT:PCBM absorption (right axis).

The averaged device parameters including the standard deviation are summarised in **Table 3.3**. Devices deposited on to ITO/PEDOT:PSS$_{HTL}$ have a J_{sc} of 8.46 mA cm^{-2}, a V_{oc} of 0.58 V and a *FF* of 0.60, producing a PCE of 3.00 %. Owing to a very high R_{sheet}, PEDOT:PSS$_{UT}$ films acted as poor electrodes producing a PCE of just 0.10 %. In contrast, the lower R_{sheet} of PEDOT:PSS$_{ADD}$ and PEDOT:PSS$_{IMM}$ electrodes allowed for comparable device performance to the ITO/PEDOT:PSS$_{HTL}$ reference, with PEDOT:PSS$_{ADD}$ and PEDOT:PSS$_{IMM}$ electrodes obtaining a PCE of 2.42 % and 2.66 % respectively. Both DMSO treated electrodes produced a similar V_{oc} and *FF* with the main difference in device performance due to the higher J_{sc} obtained for the PEDOT:PSS$_{IMM}$ electrodes. This improvement in J_{sc} can also be seen from the EQE results (**Figure 3.7.b**).

Table 3.3 – Averaged OPV device parameters P3HT:PCBM OPV devices for ITO/PEDOT:PSS_{HTL}, PEDOT:PSS_{ADD} and PEDOT:PSS_{IMM} electrodes. The standard deviation is shown in parentheses. The number of devices made using each electrode is also shown.

Electrode	*N°*	J_{sc} *(mA* cm^{-2}*)*	V_{oc} *(V)*	*FF*	*PCE (%)*
ITO/PEDOT:PSS_{HTL}	17	8.46 (0.59)	0.58 (0.01)	0.60 (0.03)	3.00 (0.21)
PEDOT:PSS_{UT}	6	0.63 (0.13)	0.58 (0.02)	0.27 (0.01)	0.10 (0.02)
PEDOT:PSS_{ADD}	14	6.62 (0.64)	0.59 (0.01)	0.63 (0.03)	2.42 (0.24)
PEDOT:PSS_{IMM}	21	7.15 (0.72)	0.59 (0.01)	0.64 (0.02)	2.66 (0.25)

A spread of the P3HT:PCBM device data using ITO/PEDOT:PSS_{HTL}, PEDOTSS_{ADD} and PEDOT:PSS_{IMM} are displayed as box and whisker plots in **Figure 3.8**. The boxes show the range of the upper and lower quartiles, the horizontal line inside the box represents the median and the purple points represent the mean. The ends of the whiskers represent the maximum and minimum data points excluding outliers. The interquartile range gives an indication of the sample variability. Therefore, from these plots the narrowest interquartile range, and so least variability in PCE, was seen for devices using ITO/PEDOT:PSS_{HTL} as an electrode. Although there is a slight variability in sample J_{sc}, devices using both DMSO treated PEDOT:PSS electrodes have a similar overall variability in PCE.

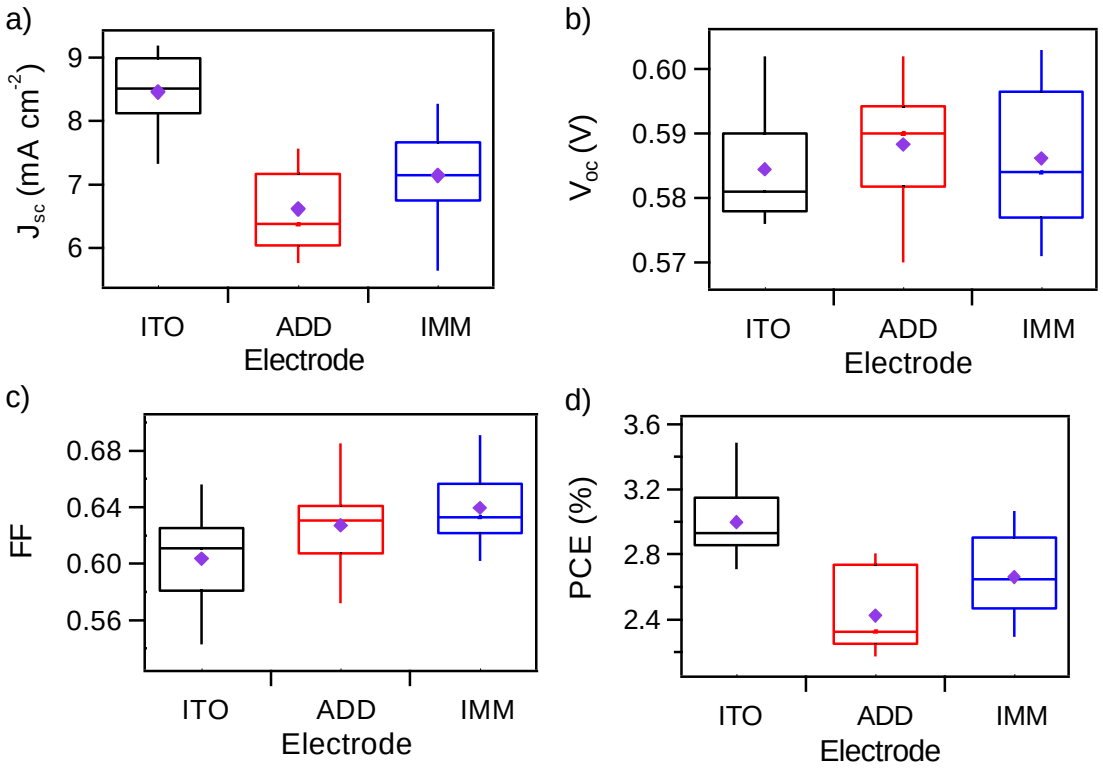

Figure 3.8 – Box and whisker plots of a) J_{sc}, b) V_{oc}, c) *FF* and d) PCE all the P3HT:PCBM OPV devices using ITO/PEDOT:PSS$_{HTL}$, PEDOT:PSS$_{ADD}$ and PEDOT:PSS$_{IMM}$ electrodes.

As there is little change in the P3HT:PCBM film thickness (~ 130 nm), absorbance or morphology (**Figure 3.9**), two possible explanations for this 10 % increase in J_{sc} for PEDOT:PSS$_{IMM}$ over PEDOT:PSS$_{ADD}$ electrodes are proposed. The first is that the PEDOT:PSS$_{IMM}$ electrodes have a lower PSS surface coverage than PEDOT:PSS$_{ADD}$ electrodes. This reduction in the insulating PSS layer could result in a more efficient and homogeneous charge extraction by the PEDOT:PSS$_{IMM}$ electrode. The second explanation is that the increase in J_{sc} could also possibly be due to a change in the P3HT:PCBM blend segregation. It is well known that phase segregation occurs in polymer blends and the lowest surface energy component (in this case P3HT) segregates to the free interface.[142] At the substrate/blend interface,

however, the segregation is partly affected by the surface energy of the substrate. Substrates with a lower surface energy have been shown to favour lower surface energy components allowing minimisation of the free energy.[143, 144] With PEDOT:PSS electrodes, the lower surface energy of PEDOT:PSS_{IMM} electrodes could promote accumulation of P3HT towards the substrate/blend interface. This more favourable phase segregation for this regular P3HT:PCBM device architecture could result in a more efficient charge transport and collection enhancing the J_{sc}.

It is difficult to explain the difference in J_{sc} between devices using ITO/PEDOT:PSS_{HTL} and DMSO treated PEDOT:PSS electrode, a difference in surface roughness of the P3HT:PCBM films is very tentatively proposed. The films formed on PEDOT:PSS_{ADD} and PEDOT:PSS_{IMM} electrodes have a higher surface roughness of 11.1 nm and 13.7 nm respectively (**Figure 3.9**) compared to 2.3 nm on ITO/PEDOT:PSS_{HTL} electrodes. Therefore Al might not sufficiently cover the P3HT:PCBM film. This could result in voids between the P3HT:PCBM and the Al electrode which would not contribute to the J_{sc} due to a decrease in the effective active area of the device. The voids are not isolated but distributed across the entire film surface therefore a difference is not seen in the EQE because there are voids within the EQE spot size.

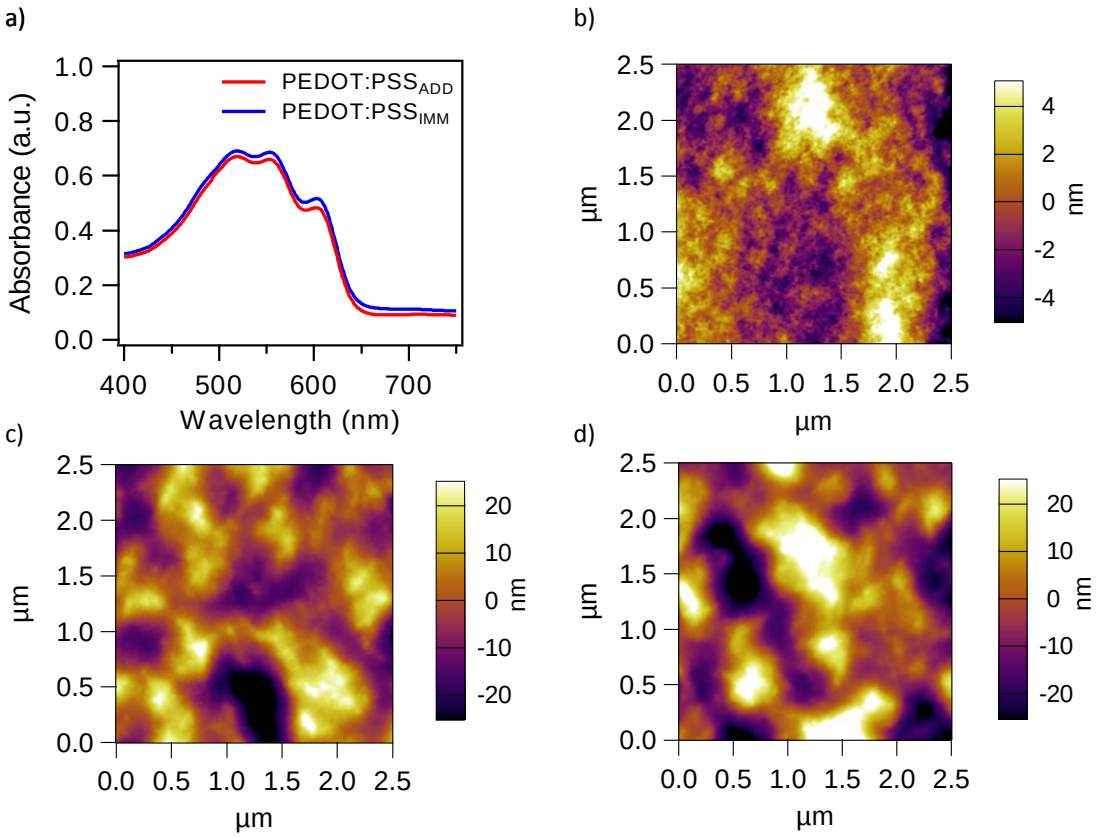

Figure 3.9 – a) UV-Vis absorption spectra of P3HT:PCBM spin coated on PEDOT:PSS$_{ADD}$ and PEDOT:PSS$_{IMM}$ electrodes and AFM topography images of P3HT:PCBM on b) ITO/PEDOT:PSS$_{HTL}$, c) PEDOT:PSS$_{ADD}$ and d) PEDOT:PSS$_{IMM}$ electrodes.

The lack of change in the V_{oc} between PEDOT:PSS$_{ADD}$ and PEDOT:PSS$_{IMM}$ electrodes is explained using the Integer Charge-Transfer (ICT) Model. For both electrodes, the work functions (5.2 eV and 4.9 eV respectively) are larger than the E_{ICT+} of the P3HT (3.9 eV).[145] Under these conditions, the work function of the organic covered electrode remains invariant while the interface dipole changes with substrate work function. Therefore, for both DMSO treated PEDOT:PSS electrodes the highest possible V_{oc} is obtained which is the difference between the E_{ICT+} of P3HT and E_{ICT-} of PCBM and is independent of the electrode work function.

3.1.6 Summary

The conductivity of an intrinsically conducting polymer can be further enhanced by the use of the high boiling point organic solvent DMSO. Two different DMSO treatments - addition and immersion - were explored in relation to the PEDOT and PSS composition on the electrode surface. Both PEDOT:PSS_{ADD} and PEDOT:PSS_{IMM} electrodes produced films with a similar R_{sheet}, but the treatments modified the PEDOT:PSS films in different ways. Immersing PEDOT:PSS films in DMSO removes excess PSS from the film, particularly in the near surface region.[98, 112, 115] The removal of PSS creates a more homogeneous and conductive surface. Adding DMSO to the PEDOT:PSS solution is thought to cause the PEDOT and PSS to rearrange into a more favourable conformation within the film.[104] Studies have suggested that this results in an expanded and more linear PEDOT chain conformation thereby increasing intra and interchain charge carrier mobility or a better three-dimensional network leading to more favourable conduction pathways.[97, 98, 146]

The effect of the different electrode treatments on P3HT:PCBM OPV device performance was also studied and compared to an ITO/PEDOT:PSS_{HTL} reference device. OPV devices fabricated on PEDOT:PSS_{IMM} electrodes out-performed those based on PEDOT:PSS_{ADD} electrodes. The larger PCE obtained on PEDOT:PSS_{IMM} electrodes was mainly due to an increase in J_{sc}. This indicates the potential for PEDOT:PSS electrodes as a possible low cost and roll-to-roll processable electrode for OPV devices, while still obtaining a reasonable OPV device performance. Additionally, it highlights that while treatments may have a similar effect on the

PEDOT:PSS conductivity, subtle differences in the electrode surface may make one treatment more compatible with a photoactive system than another.

3.2 Spray deposited PEDOT:PSS$_{ADD}$ electrodes

Spin coating is commonly used method to fabricate films in the laboratory. Although spin coating results in reproducibly smooth and homogenous films, it is not well suited to the commercial scale up of devices. In this section the use of spray deposition, a technique that is well established in industry and has gained attention in OPV device fabrication, as a method for electrode fabrication is characterised. PEDOT:PSS$_{ADD}$ films were used to allow direct comparison between spin coating and spray deposition. A comparison is made between spin coated and spray deposited PEDOT:PSS$_{ADD}$ electrodes in a CuPc/C_{60} OPV bilayer heterojunction device, with an active area of 0.06 cm^2.

The advantage of using this small molecule system is the ability to simultaneously vacuum deposit the photoactive material onto multiple substrates. Vacuum deposition allows for very reproducible device performance within the batch unlike solution processing where there can be a high degree in variability within the same batch. Using this photoactive system therefore allows for direct comparison between spin coated, spray deposited PEDOT:PSS$_{ADD}$ and ITO electrodes. PEDOT:PSS$_{ADD}$ electrodes were chosen for this solution deposition comparison simply because these electrodes are quicker and easier to process than PEDOT:PSS$_{IMM}$ electrodes.

3.2.1 Topography

The spray deposited PEDOT:PSS$_{ADD}$ electrodes were fabricated by passing multiple heated (60 ^oC) glass substrates consecutively through the PEDOT:PSS$_{ADD}$ spray

flux. The airbrush was held at a constant height of 8 cm above the substrates (**Figure 3.10**).

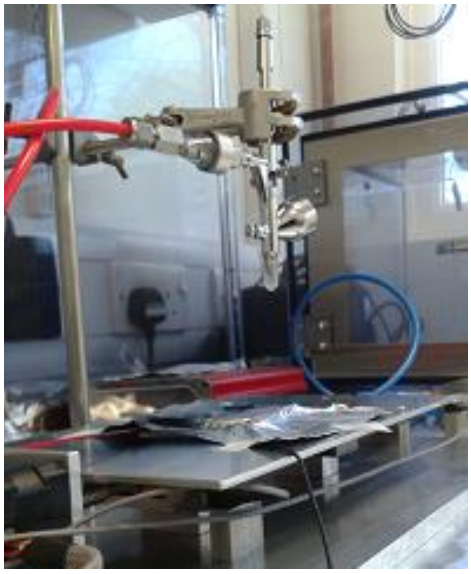

Figure 3.10 – Image of the spray deposition set-up showing a commercially available airbrush clamped above a purpose designed linear translation stage.

Upon impact with the substrate the spray droplets dried, causing a build-up of multiple droplets to produce pin-hole free films on just one pass of the substrates.[147] To study the resulting film topography of the spray deposited electrodes, large area (30 × 30 μm) AFM images were obtained and compared to the surface topography of spin coated PEDOT:PSS_{ADD} electrodes, as shown in **Figure 3.11**. As can be visible seen (**Figure 3.11.c**), the AFM topography image (**Figure 3.11.a**) indicates that the spray deposited electrodes possess a rough surface topography with a root mean square (RMS) roughness of 17 nm, and therefore a much greater variation in film thickness compared to the smoother spin coated films shown in **Figure 3.11.b**,

which have a RMS of 1.8 nm for a 63 nm thick film, with a standard deviation (σ) of 3 nm.

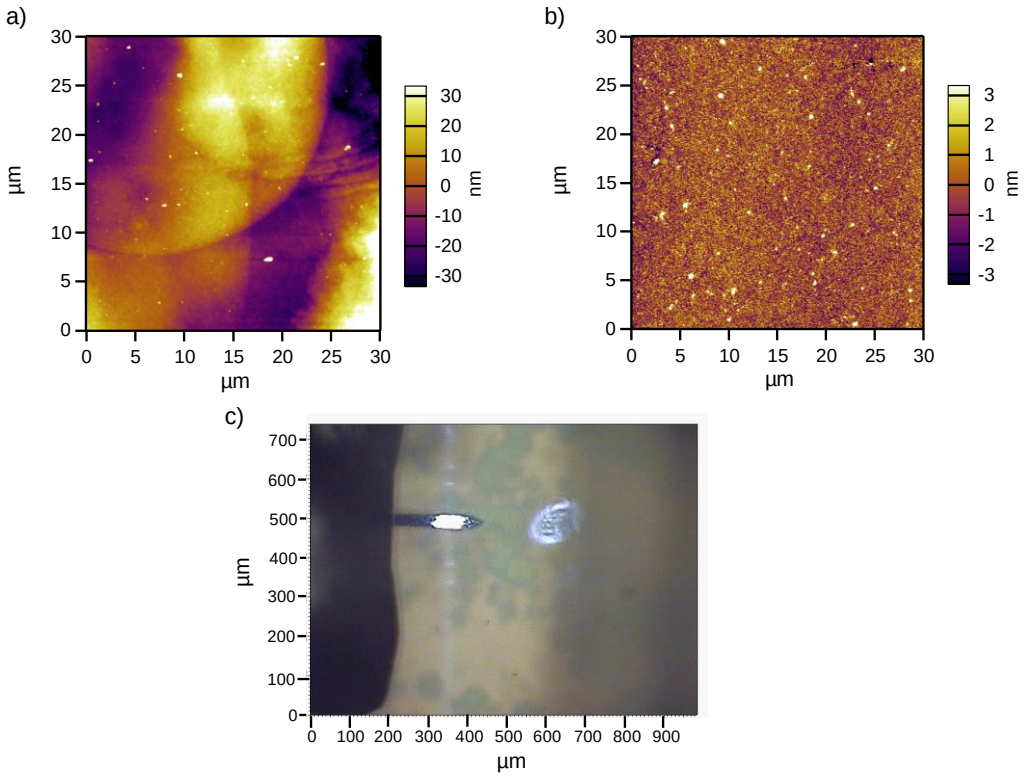

Figure 3.11 – Topography AFM images of a) spray deposited and b) spin coated PEDOT:PSS_{ADD} electrodes and c) in-situ AFM camera image of spray deposited PEDOT:PSS electrode also showing the AFM probe.

3.2.2 Current distribution

CAFM was used to investigate if the increased surface roughness from the spray deposition technique had an influence on the distribution of PEDOT and PSS at the electrode surface. **Figure 3.12** shows representative examples of simultaneously obtained CAFM topography (**Figure 3.12.a - c**) and current maps (**Figure 3.12.d - f**) of the spin coated (**Figure 3.12.a** and **d**) and spray deposited (**Figure 3.12.b**, **c**, **e** and **f**) PEDOT:PSS_{ADD} films. The current distribution histograms further illustrate the

distribution of PSS on the film surface (**Figure 3.12.g – i**). Again, all these images of PEDOT:PSS_{ADD} films were imaged on the same day and using the same CAFM tip. When using either deposition technique, regions of high current, 12 – 26 nm in size are surrounded by insulating material, with no obvious long range ordering. Similarly to spin coated electrodes, these spray deposited PEDOT:PSS_{ADD} electrodes consisted of randomly scattered conductive regions which were assigned as PEDOT domains and the insulating areas as PSS. The conductive grains were independent from topographical features. The average current of each electrode was analysed over a series of 1 × 1 μm area images, with representative images shown in **Figure 3.12**. Spray deposited electrodes display a higher variability in average current compared to the spin coated films, with an average current of 298 pA (σ = 28 pA), compared with a value of 301 pA (σ = 6 pA) for spin coated films. **Figure 3.12.c** and **Figure 3.12.f** shows 1 × 1 μm topography and current images respectively at the edge of a droplet on the sprayed electrode. Here, at the droplet boundary a less conductive region with a width of 50 – 90 nm has formed. The effect of this decrease in conductivity is minimal due to the relative area covered compared to the size of the droplet. This combined with the lack of correlation between current and topography, highlights that although spray deposition leads to far rougher electrodes; the surface in contact with the active layer has a similar PEDOT and PSS distribution as the smoother spin coated films.

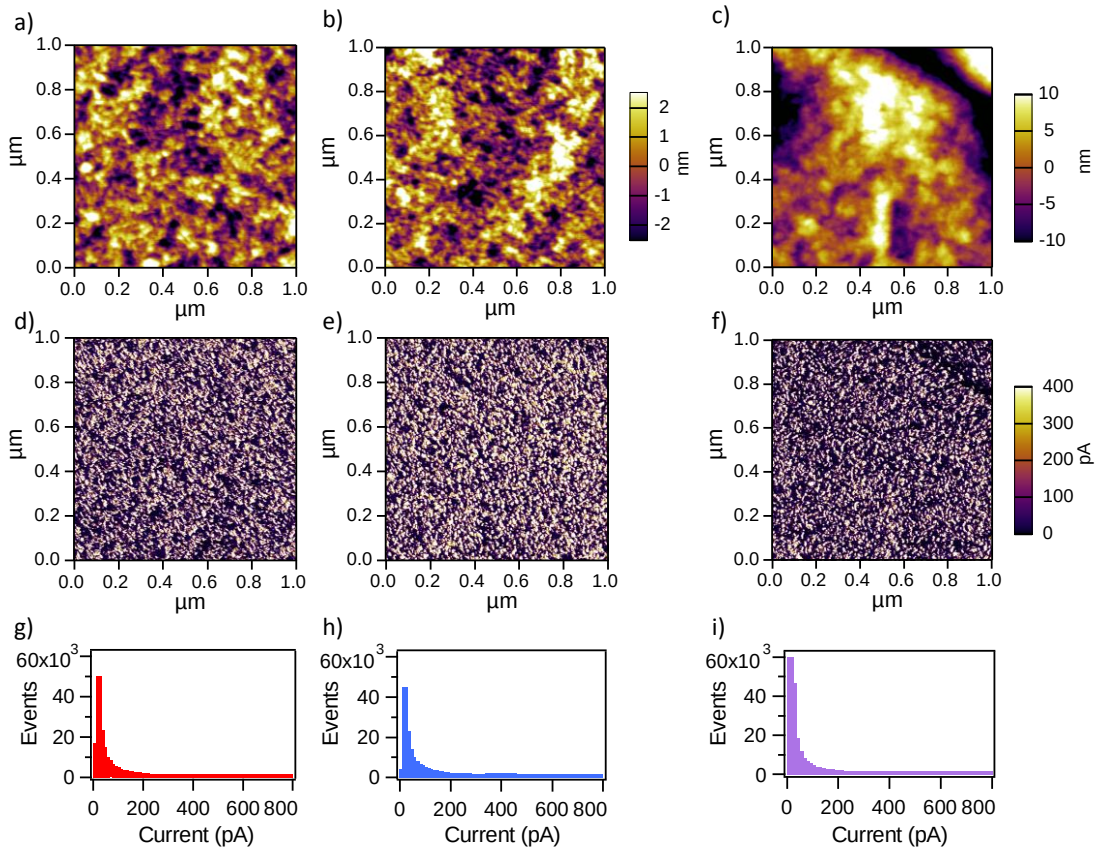

Figure 3.12 – CAFM topography (a – c) and current distribution at +200 mV (d – f) of spin coated (a and d) and spray deposited (b and e) PEDOT:PSS_{ADD} electrodes. The topography and current distribution for a droplet edge (c and f) is also shown.

3.2.3 Transmittance and sheet resistance

In order to be suitable for use as a TCE, the film requires a high degree of transparency across the visible region. The spin coated films prepared here have a transmittance of over 80 % across the entire visible region with a transparency of 85 % at 620 nm, the absorption maximum of CuPc. In comparison, ITO_{bare} has a lower transmittance across most of the visible region, but has an increased transmittance between 525 – 590 nm (**Figure 3.13**). The R_{sheet} of the spin coated films is ~ 200 Ω sq^{-1}, just one order of magnitude greater than that of ITO. As would be expected

with the spray coated electrodes, a favourable increase in transmittance corresponds with an unfavourable increase in R_{sheet}. Two films with different transparencies spray deposited, $Spray_A$ and $Spray_B$, are shown in **Figure 3.11**.

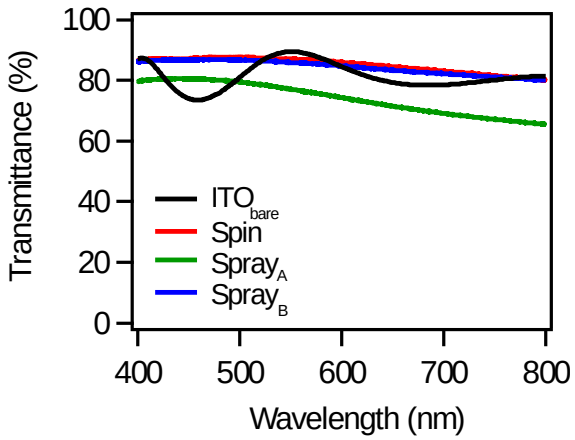

Figure 3.13 – Transmission spectra of ITO_{bare}, spin coated and two spray deposited $PEDOT:PSS_{ADD}$ electrodes. The $PEDOT:PSS_{ADD}$ electrode was spin coated or spray deposited onto glass substrates.

$Spray_A$ has a film thickness of 261 nm, (σ = 81 nm) and so has a much lower transparency (73 % at 620 nm), with a R_{sheet} of 88 Ω sq^{-1}. This is compared to 810 Ω sq^{-1} for the more transparent (84 % at 620 nm) and thinner (76 nm σ = 43 nm) $Spray_B$. The R_{sheet}, film thickness and transmittance are summarised in **Table 3.4**.

Table 3.4 – Summary for the R_{sheet}, film thickness and transmittance (at 620 nm) for spin coated, $Spray_A$ and $Spray_B$ $PEDOT:PSS_{ADD}$ electrodes.

Electrode	R_{sheet} *(Ω sq^{-1})*	*Film thickness (nm)*	*Transmittance (%)*
Spin coated	208	68	85
$Spray_A$	88	261	73
$Spray_B$	810	76	84

3.2.4 Comparison of spin coated and spray deposited electrodes

To investigate the possibility that a potentially high throughput spray deposited $PEDOT:PSS_{ADD}$ could be used as an alternative TCE to ITO in OPV devices, $Spray_A$ and $Spray_B$ electrodes were compared to spin coated $PEDOT:PSS_{ADD}$ and a commercially available ITO electrode. The following device structure was used: electrode/30 nm CuPc/40 nm C_{60}/8 nm BCP/Al. CuPc was chosen as the donor material because of its favourable energy alignment with both $PEDOT:PSS_{ADD}$ and ITO_{bare} which removes the need for a transport layer between the electrode and donor.[55] J-V curves and EQE spectra are shown in **Figure 3.14**.

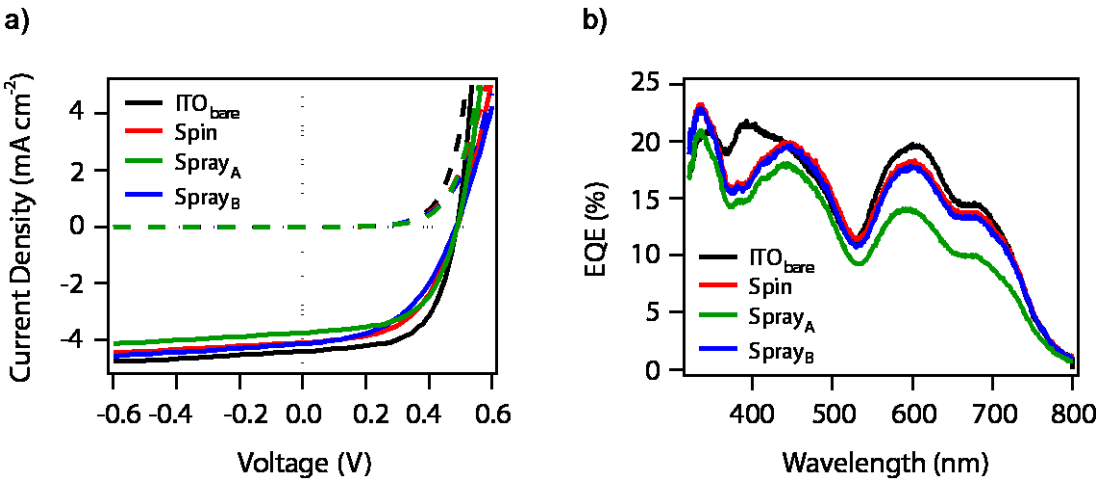

Figure 3.14 – a) J-V curves under 1 sun illumination (solid lines) and in the dark (dashed lines) and b) EQE curves for CuPc/C_{60} OPV devices on ITO_{bare}, spin coated and $Spray_A$ and $Spray_B$ PEDOT:PSS_{ADD} electrodes.

The resulting key device parameters are shown in **Table 3.5**. Devices deposited onto ITO_{bare} had a J_{sc} of 4.40 mA cm^{-2}, a V_{oc} of 0.49 V and a *FF* of 0.61, resulting in a PCE of 1.31 %. Spin coated electrodes produced devices with a J_{sc} of 4.14 mA cm^{-2}, a V_{oc} of 0.49 V and a *FF* of 0.55 to give a PCE of 1.11 %. Due to a lower transmittance (**Figure 3.13**), devices grown on $Spray_A$ electrodes had a lower J_{sc} of 3.75 mA cm^{-2} and a V_{oc} of 0.49 V and a *FF* of 0.57, producing a PCE of 1.08 %. $Spray_B$ electrodes had a similar transmittance to spin coated electrodes and these devices had a similar J_{sc} of 4.13 mA cm^{-2}, a V_{oc} of 0.49 V and a FF of 0.49 producing an overall PCE of 1.01 %. Devices on ITO electrodes achieved a PCE just 15 % greater than spin coated PEDOT:PSS_{ADD} electrodes and 18 % more than $Spray_A$. The increased surface roughness of the spray deposited PEDOT:PSS_{ADD} did not appear to significantly hinder the device performance, with $Spray_A$ electrodes only 3 % lower in PCE than the spin coated electrodes.

Table 3.5 – OPV device parameters for $CuPc/C_{60}$ devices with ITO_{bare}, spin coated and spray deposited electrodes.

Electrode	J_{sc} *(mA cm^{-2})*	V_{oc} *(V)*	*FF*	*PCE (%)*
ITO_{bare}	4.40	0.49	0.61	1.31
Spin coated	4.14	0.49	0.55	1.11
$Spray_A$	3.75	0.49	0.57	1.08
$Spray_B$	4.13	0.49	0.49	1.01

As expected, the thicker (261 nm) and least transparent $PEDOT:PSS_{ADD}$ electrode $Spray_A$, produced the lowest J_{sc}. However, it achieved the highest *FF* of the $PEDOT:PSS_{ADD}$ electrodes, due to possessing the lowest R_{sheet} (88 Ω sq^{-1}). Although the thinner (76 nm) $Spray_B$ devices with an enhanced transmittance gave a higher J_{sc} than $Spray_A$, the substantially higher R_{sheet} (810 Ω sq^{-1}) of $Spray_B$ electrodes resulted in a lower *FF*. This led to devices with a similar PCE to $Spray_A$ devices. This demonstrates that the transparency and R_{sheet} of the spray deposited PEDOT:PSS electrodes can be easily tailored, which directly influences the J_{sc} and *FF* and highlights the potential application of spray deposition in low cost large area OPV device fabrication.

Figure 3.14.b compares the external quantum efficiency (EQE) for the $CuPc/C_{60}$ devices on each electrode. Both materials contribute to the photocurrent in the device as has been shown previously.[22] The high transparency of the ITO electrode

across the visible region provides enhanced current generation across most wavelengths. The EQE peak of 18.8 % at 620 nm is due to contribution from the CuPc donor material. Spectra with a CuPc peak maxima at 620 nm were also obtained for the solution processed PEDOT:PSS_{ADD} electrodes. The spin coated electrode produced an EQE of 16.9 % at 620 nm, compared to 16.5 % and 12.8 % for $Spray_A$ and $Spray_B$ respectively. The overall integrated current for all the devices follows the same trend obtained from the device J_{SC}, discussed above.

3.2.5 Summary

Spray deposited PEDOT:PSS_{ADD} electrodes provide a reasonable overall device performance with just a small loss in comparison to a commercially available ITO electrode. Although spray deposition produces PEDOT:PSS_{ADD} electrodes with a significantly higher surface roughness, the topographical current distribution is similar to the spin coated electrodes. This indicates a similar surface composition of PEDOT and PSS with both fabrication techniques for both fabrication methods. The transparency and R_{sheet} of these spray deposited films can be easily tailored, which directly influences the J_{sc} and the *FF* of the devices. This highlights the potential of spray deposited PEDOT:PSS_{ADD} film as a method for rapidly producing inexpensive ITO-free OPV devices.

3.3 PEDOT:PSS$_{ADD}$ electrodes in larger area devices

This section investigates the effect of increasing the active area of OPV devices using PEDOT:PSS$_{ADD}$ electrodes. SubPc/C_{60} is another D/A heterojunction system that can be used in combination with both ITO and PEDOT:PSS$_{ADD}$ electrodes through the use of MoO_x as an interfacial layer. One of the advantages of using SubPc as a donor material is it has a high IP of 5.6 eV and so devices produce a larger V_{oc} (~ 1.1 V) than other phthalocyanine/C_{60} devices.[70] Similarly to CuPc/C_{60} devices in **Section 4.2**, SubPc can be thermally deposited onto multiple substrates simultaneously. This allows for direct comparison where a change in device performance should be influenced solely by the electrode. MoO_x is commonly used in OPV devices as a hole extracting layer that can also be thermally deposited. It has a high transparency, reasonable conductivity and has been shown to modify the anode to give ohmic contact with high IP donor materials.[55]

3.3.1 Spin coated PEDOT:PSS$_{ADD}$ electrodes

The following device architecture was used in electrode comparison: electrode/5 nm MoO_x/14 nm SubPc/40 nm C_{60}/8 nm BCP/Al, where the active area size was varied. Comparisons were made between the electrodes with the same active area by depositing the photoactive materials on top of the electrodes simultaneously, so any difference in device performance is solely due to the electrode. Devices with different size active areas were not fabricated at the same time; so the difference in device performance may also be due to batch-to-batch variation in addition to the change in electrode. The PEDOT:PSS$_{ADD}$ electrodes were not optimised

independently for this active layer system and active area size, and all were spin coated at 3000 RPM for 60 s producing films with a similar thickness and transmittance profile. **Figure 3.15** shows J-V curves for SubPc/C_{60} devices with an active area of 0.16 cm^2 and 0.30 cm^2 on ITO electrodes and 0.16 cm^2, 0.30 cm^2 and 1.04 cm^{-2} on PEDOT:PSS_{ADD} electrodes.

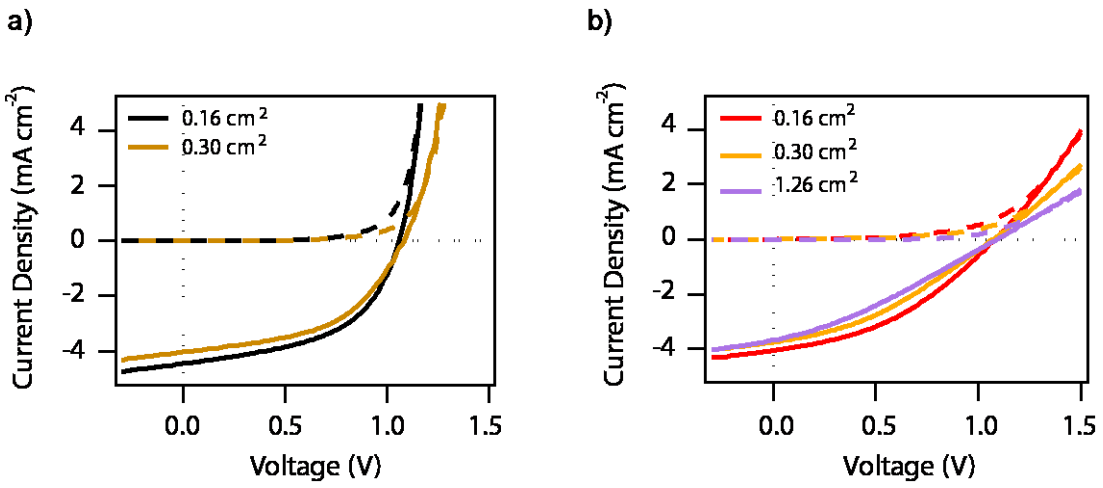

Figure 3.15 – J-V curves under illumination (solid lines) and in the dark (dashed lines) for SubPc/C_{60} OPV devices with a) ITO/MoO_x and b) spin coated PEDOT:PSS_{ADD} electrodes with an active area of 0.16 cm^2, 0.30 cm^2 and 1.04 cm^2.

Table 3.6 displays the key device parameters for SubPc/C_{60} OPV devices with increasing active areas. Devices using an ITO/MoO_x electrode with an active area of 0.16 cm^2 have a J_{sc} of 4.55 mA cm^2, a V_{oc} of 1.06 V and a *FF* of 0.52 producing PCE of 2.46 %. On the larger 0.30 cm^2 ITO/MoO_x electrodes a lower J_{sc} and FF of 4.04 mA cm^{-2} and 0.50 respectively were obtained, and a V_{oc} of 1.08 V, giving a PCE of 2.32 %. Devices deposited on a PEDOT:PSS_{ADD} electrode based devices with an active area of 0.16 cm^2 gave a J_{sc} of 4.05 mA cm^{-2}, V_{oc} of 1.08 V and *FF* of 0.39, producing a PCE of 1.70 %. As the active area was increased up to 0.30 cm^2 and

1.04 cm^2 the PCE decreased to 1.52 % and 1.18 % respectively. This decrease in PCE for devices was predominantly due to the decrease in *FF* and J_{sc}.

Table 3.6 – OPV device parameters for SubPc/C_{60} devices with ITO and spin coated PEDOT:PSS_{ADD} electrodes with an active area of 0.16 cm^2, 0.30 cm^2 and 1.04 cm^2.

Electrode	*Area (cm^2)*	*J_{sc} ($mA\ cm^{-2}$)*	*V_{oc} (V)*	*FF*	*PCE (%)*
ITO	0.16	4.55	1.06	0.52	2.46
ITO	0.30	4.04	1.08	0.50	2.32
PEDOT:PSS_{ADD}	0.16	4.05	1.08	0.39	1.70
PEDOT:PSS_{ADD}	0.30	3.75	1.07	0.36	1.52
PEDOT:PSS_{ADD}	1.04	3.67	1.09	0.31	1.18

As shown in previous reports, increasing the active area of OPV devices for both ITO and PEDOT:PSS_{ADD} electrodes results in a decrease in both the J_{sc} and *FF*.[133, 148, 149] This decrease is attributed to an increase in the series resistance (R_s) of the TCE. As can be seen from the slope of the J-V curves in **Figure 3.15**, for devices using both ITO and PEDOT:PSS_{ADD} electrodes, the R_s increases with increasing active area. The R_s denotes the total resistance of the device and is composed of the active and interfacial layer resistance, the electrode resistances, and any contact and intercontact resistances. The contribution of the photoactive layer to the area-scaled R_s contribution does not increase with increase in active area because the charge

carriers still travel the same perpendicular distance through the interfacial and photoactive layers. Thus any losses related to the resistance of these layers are independent of active area. The Al electrode resistance is considered negligible compared to the ITO electrode and so the TCE resistance is the dominant factor when considering the effect of device area on R_s.[148] Since the anode has a non-negligible R_{sheet}, its contribution to the power loss significantly increases with increasing active area. As the V_{oc} is related to the energy offset between the donor and acceptor or to the work function of the electrodes which both influence the vertical current flow, increasing the current flow laterally should not significantly impact the V_{oc}.

A report by Servaites determined that for an OPV device using an ITO electrode with a PCE of 5.2 % the TCE resistance losses are minor for active areas of under 0.2 cm^2 and become more of a concern for areas above 0.2 cm^2.[133] Since PEDOT:PSS_{ADD} electrodes are less conductive than ITO electrodes increasing active area has a far greater impact on the R_s of these devices. Strategies such as electroplating metal grids on top of ITO and PEDOT:PSS are a possible way to decrease the resistance of the TCE, since the metal grids provide an alternative and lower resistance pathway for the current.[83, 150 151] When using a metal grid, however, care is needed to ensure that the best compromise between shadow and resistive losses is found.[151]

3.3.2 Spray deposited PEDOT:PSS$_{ADD}$ electrodes

The same SubPc/C_{60} device structure was used to investigate spray deposition as a technique to fabricate larger area electrodes. Two 0.30 cm^{-2} spray deposited PEDOT:PSS$_{ADD}$ electrodes were fabricated; the glass substrates where held stationary under the spray flux for either 30 s (Spray$_C$) or 60 s (Spray$_D$). **Figure 3.16** shows the J-V curves for OPV devices using Spray$_C$ and Spray$_D$ electrodes.

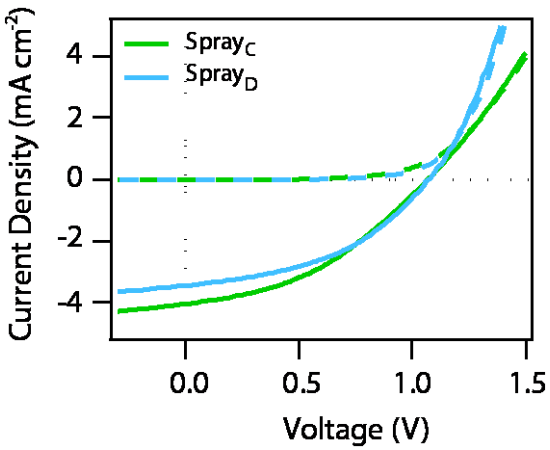

Figure 3.16 – J-V curves under illumination (solid lines) and in the dark (dashed lines) for SubPc/C_{60} OPV devices with spray deposited PEDOT:PSS$_{ADD}$ electrodes with an active area of 0.30 cm^2.

Table 3.7 displays the key device parameters for devices using the PEDOT:PSS$_{ADD}$ spray deposited electrodes. Devices using Spray$_C$ electrodes had a J_{sc} of 4.06 mA cm^{-2}, a V_{oc} of 1.07 V and a *FF* of 0.40 resulting in a PCE of 1.82 %. Devices with Spray$_D$ as an electrode had a 3.52 mA cm^{-2}, V_{oc} 1.07 V and a *FF* of 0.47 producing a PCE 1.88 %. Similarly to **Section 3.2.4**, devices utilising a Spray$_C$ and Spray$_D$ electrodes had a similar PCE, although the J_{sc} and *FF* are quite different. As previously demonstrated, the electrode that was held under the spray flux for a longer period (Spray$_D$) had the lower J_{sc} but higher *FF* due to thicker films having a

decreased transmittance and lower $R_{sheet.}$ Equal sized devices using ITO electrodes (**Table 3.6**) achieved a PCE just ~ 20 % greater than the spray deposited PEDOT:PSS_{ADD} electrode. This was comparable to the percentage difference seen for CuPc/C_{60} devices using the smaller 0.06 cm^2 spray deposited electrodes in **Section 3.2**.

Table 3.7 – OPV device parameters for SubPc/C_{60} devices with ITO, spin coated and spray deposited PEDOT:PSS_{ADD} electrodes with an active area of 0.30 cm^2.

Electrode	J_{sc} *(mA* cm^{-2}*)*	V_{oc} *(V)*	*FF*	*PCE (%)*
$Spray_C$	4.06	1.07	0.40	1.82
$Spray_D$	3.52	1.07	0.47	1.88

3.3.3 Summary

Increasing the active area of OPV devices using both ITO and PEDOT:PSS_{ADD} electrodes resulted in decrease in a PCE due to an increase in R_s. The PCE of devices using PEDOT:PSS_{ADD} electrodes was more affected by increasing the active area due to their lower R_{sheet}. A possible strategy to reduce the impact of larger active areas would be to combine the TCE with a metal grid. A benefit of this approach is that both the PEDOT:PSS and metal grid could be deposited by spray (or print) deposition and this combination could be a potential alternative to ITO electrodes in large area devices. Spray deposition has already been proven as a way of rapidly depositing PEDOT:PSS in an easily controlled manner. The film

thickness and therefore transparency and R_{sheet} are simply controlled through the amount of time the substrate is held under the spray flux which highlight the possibility of using this technique in low cost and large area OPV device fabrication.

3.4 Conclusions

PEDOT:PSS is a conducting polymer which when spin coated onto glass substrates shows high transparency in the visible region and reasonably high conductivity. Despite being classed as conductive, the conductivity of PEDOT:PSS films is much lower than that of ITO. This chapter has focused on using DMSO to improve the conductivity of PEDOT:PSS.

To begin with, two different DMSO treatments – addition and immersion – were explored in relation to the PEDOT and PSS composition on the electrode surface. Both treatments decreased the R_{sheet} of the PEDOT:PSS electrodes by a similar magnitude compared to $PEDOT:PSS_{UT,}$ however the enhancement is a result of different modifications to the film. Immersing a PEDOT:PSS film in DMSO resulted in a large reduction in the amount of PSS seen on the electrode surface, whereas adding DMSO to the PEDOT:PSS dispersion is thought to cause the PSS to rearrange within the film. OPV devices utilising a $PEDOT:PSS_{IMM}$ electrode performed better than those using a $PEDOT:PSS_{ADD}$ electrode. The increase in device performance was mainly due to a 10 % increase in J_{sc}. This indicates that although both DMSO treatments have a similar effect on the PEDOT:PSS film conductivity, the subtle differences in the electrode surface have an effect on the OPV device performance.

One of the advantages of using PEDOT:PSS as an electrode is the potential it provides for high-throughput, low cost processing on large area substrates. Spray deposition is a technique that is capable of being employed in a roll-to-roll process. A CuPc/C_{60} photoactive system was used to allow comparison between PEDOT:PSS_{ADD} deposited by spin coating and spray deposition. Despite the increased surface roughness of these electrodes the device performance was similar to that of the smoother spin coated electrodes.

The PCE for SubPc/C_{60} devices for both ITO and PEDOT:PSS_{ADD} electrodes decreased upon increasing the active area due to an increase in R_{sheet}. However, larger area devices using spray deposited PEDOT:PSS_{ADD} electrodes still displayed as reasonable an efficiency as the smaller area devices. This highlights the potential for spray deposited PEDOT:PSS electrodes as a method for rapidly producing inexpensive ITO-free OPV devices.

Chapter 4. P3HT:PCBM device processing conditions

As OPV devices are touted as a promising cheap, alternative renewable energy source with their ever increasing PCE due to novel photoactive materials and interlayers, a greater focus on their economic and environmental implications is needed. This chapter explores different processing conditions for the P3HT:PCBM photoactive layer. To begin with, P3HT:PCBM devices were fabricated under ambient conditions with the aim of achieving comparable device performance to reference devices that were fabricated under N_2. The methodology developed for the air processed photoactive layer was then used for the rest of the chapter. Next the importance of using an appropriate interfacial layer was addressed along with the benefits of using an inverted device architecture. The final section looks towards using non-halogenated solvents for the P3HT:PCBM solution in both regular and inverted devices.

4.1 Air processing

Ideally, to minimise costs, OPV devices should be entirely processed under ambient conditions as the use of inert environments would further add to the expense. However, devices are typically entirely fabricated in inert atmospheres since oxygen has been reported to induce traps in the P3HT:PCBM active layer, oxidise the metal electrode and adversely affect device performance and stability.[152, 153] This section demonstrates a quick optimisation for developing a methodology for depositing P3HT:PCBM devices in air that give similar device performance to those spin coated under nitrogen. The procedure was developed on ITO electrode based devices, but was also seen to be applicable to devices using PEDOT:PSS_{ADD} and PEDOT:PSS_{IMM} electrodes as well.

4.1.1 Spin coating conditions

P3HT:PCBM dissolved in DCB (P3HT:$PCBM_{DCB}$) was spin coated onto ITO/PEDOT:PSS_{HTL} and PEDOT:PSS_{ADD} electrodes in either a nitrogen filled glove box (N_2) or in a fume cupboard open to air (Air). The same P3HT:$PCBM_{DCB}$ stock solution, made under N_2, was used for all devices made. After spin coating in either atmosphere, the wet P3HT:$PCBM_{DCB}$ films were left uncovered to completely dry and were then annealed at 120 ^{o}C for 20 minutes, all under the same atmosphere that they were originally spin coated in. Once annealed, all devices were transferred into the evaporation system where BCP was thermally evaporated on top of the photoactive layer, followed by Al through a shadow mask. The J-V curves for these devices are shown in **Figure 4.1**.

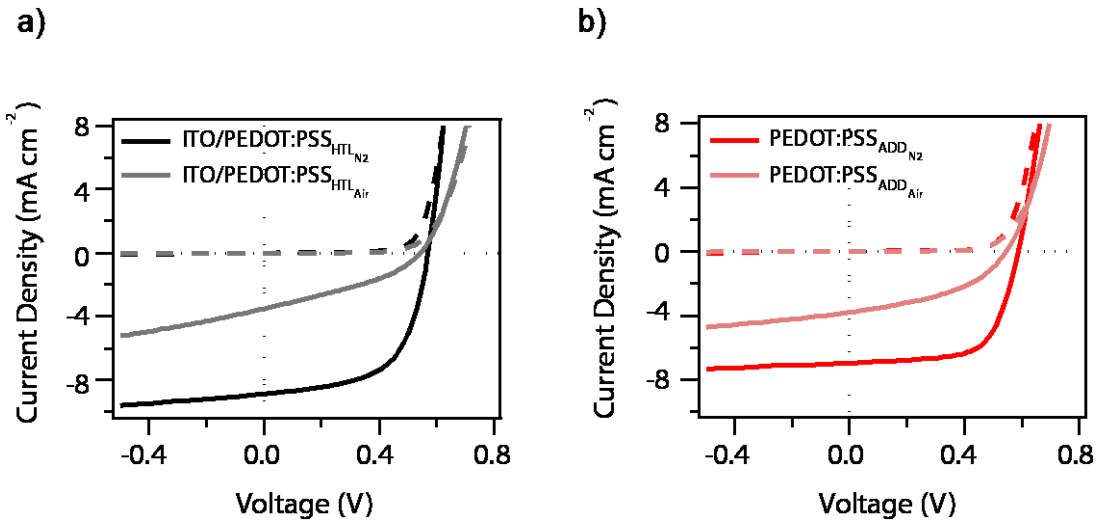

Figure 4.1 – J-V curves under 1 sun illumination (solid lines) and in the dark (dashed lines) for P3HT:PCBM$_{DCB}$ devices entirely processed under nitrogen or air on a) ITO/PEDOT:PSS$_{HTL}$ and b) PEDOT:PSS$_{ADD}$ electrodes.

Table 4.1 displays the key performance parameters for this set of devices. Devices fabricated under a N_2 atmosphere on ITO and PEDOT:PSS$_{ADD}$ electrodes achieved similar parameters to devices shown in **Chapter 3.1.5**. On the ITO electrode, devices produced a J_{sc} of 8.88 mA cm^{-2}, a V_{oc} of 0.57 V and a *FF* of 0.59 resulting in an overall PCE of 2.92 %. When fabricated on a PEDOT:PSS$_{ADD}$ electrode devices gave a J_{sc} of 6.97mA cm^{-2}, a V_{oc} of 0.59 V and a *FF* of 0.66 and an overall PCE of 2.61 %. As might be expected, devices that were completely fabricated in air achieved poor performances. This was most likely due to the prolonged oxygen exposure which has previously been shown to affect OPV device performance.[152, 154] Diffusion of oxygen in to the photoactive layer is thought to induce oxygen traps which increases the rate of recombination and so decreases the charge mobility of P3HT and PCBM.[155] Devices using an ITO electrode had a reduced J_{sc} of 3.51 mA cm^{-2}, a V_{oc} of 0.54V and a *FF* of 0.35 resulting in an overall PCE of 0.65 %. A

similarly poor performance of 0.86 % was seen for devices using PEDOT:PSS_{ADD} electrodes. These had a J_{sc} of 3.80 mA cm^{-2}, a V_{oc} of 0.54 V and a *FF* of 0.42

Table 4.1- OPV device parameters for P3HT:$PCBM_{DCB}$ devices processed under nitrogen or air on ITO/PEDOT:PSS_{HTL} and PEDOT:PSS_{ADD} electrodes.

Electrode	*Atmosphere*	J_{sc} *(mA* cm^{-2}*)*	V_{oc} *(V)*	*FF*	*PCE (%)*
ITO	N_2	8.88	0.57	0.59	2.92
ITO	Air	3.51	0.54	0.35	0.65
PEDOT:PSS_{ADD}	N_2	6.97	0.59	0.66	2.61
PEDOT:PSS_{ADD}	Air	3.80	0.54	0.42	0.86

4.1.2 Post-spin coating conditions

P3HT:$PCBM_{DCB}$ devices that were spin coated and dried in air were seen to dry much faster than those spin coated and dried under N_2, which may have contributed to the poor device performance. Significant work by Li *et. al.* demonstrated that solvent annealing enhanced the absorption and charge transport leading to improved PCE of P3HT:PCBM devices.[45, 156] The slower solvent evaporation rate allowed the P3HT to self-organise into a high degree of order even when mixed as a blend with PCBM. The post-spin coating steps were therefore broken down into stages. Directly after spin coating in air the devices were then left in air to dry uncovered as in **Section 4.1.1** (fast dried) or left to dry more slowly by covering the devices with a petri dish lid (slow dried). Devices spin coated and dried under N_2 were fast dried as

a basic reference. Once all the devices were dry, half of the fast dried and half of the slow dried devices were transferred in the glove box and annealed under N_2 and the other half annealed in air, all at 120 ºC for 20 minutes. Once annealed, all devices were transferred into the evaporation system where BCP and Al were thermally evaporated on top of the photoactive layer. The devices processed under different conditions were compared to devices that were spin coated in N_2, fast dried and annealed under N_2. The J-V curves are shown in **Figure 4.2.a** and a schematic of the process stages is shown in **Figure 4.2.b**.

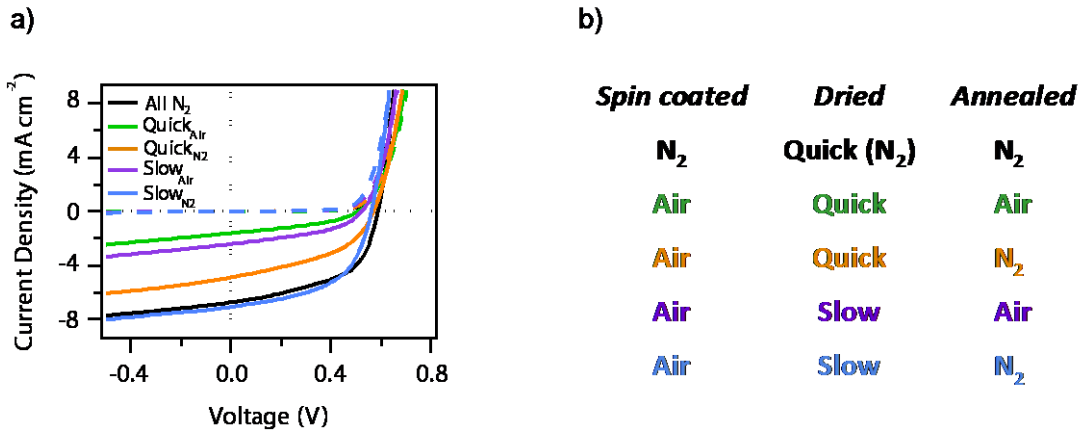

Figure 4.2 – a) J-V curves under 1sun illumination (solid lines) and in the dark (dashed lines) for P3HT:$PCBM_{DCB}$ devices spin coated in air with different drying conditions on an ITO/PEDOT:PSS_{HTL} electrode and b) schematic displaying the different processing conditions.

The key device parameters are displayed in **Table 4.2**. In this set of the devices, the reference device that was completely processed in N_2 did not perform as well as previous batches of P3HT:$PCBM_{DCB}$ devices, but as the same solution was used for all device variations a comparison could still be made between the different processing conditions. The reference devices processed under N_2 had a lower J_{sc} and

FF than usual at 6.74 mA cm^{-2} and 0.53 respectively, and a V_{oc} of 0.59 V giving a lower PCE of 2.06 %. For the devices that were spin coated in air, the devices that were fast dried and annealed in air had the lowest performance, with a J_{sc} of 1.61 mA cm^{-2}, a V_{oc} of 0.51 and a *FF* of 0.38 producing a PCE of 0.31 %. When annealed under N_2, the PCE of the fast dried devices was much higher at 1.22 % due to an increase in all key parameters. While slow drying films and annealing in air does improve the device performance to a *Jsc* of 2.41 mA cm^{-2} resulting in a PCE of 0.53 %, devices that were both slow dried in air and annealed under N_2 had the best performance, with a PCE of 2.11 %. This improvement was mainly due to the expected large increase in J_{sc} and *FF* that slower solvent evaporation has been shown to achieve. Devices that were spin coated in air, covered and subjected to a slower drying time and annealed under N_2 performed comparably to devices fully processed under N_2. It is interesting to note that the overall device performance increases by a factor of four when the only parameter changed is annealing under N_2 rather than air. This was seen regardless of whether the photoactive layers were quick or slow dried. It has been seen that the original mobility can be recovered after oxygen exposure by thermal annealing which has been shown to remove oxygen contamination, and this may have been the cause here. [157-159]

Table 4.2 – OPV device parameters for P3HT:$PCBM_{DCB}$ devices spin coated in air with different drying and annealing conditions on an ITO/PEDOT:PSS_{HTL} electrode.

Spun	*Dried*	*Annealed*	J_{sc} *(mA* cm^{-2}*)*	V_{oc} *(V)*	*FF*	*PCE (%)*
N_2	Quick (N_2)	N_2	6.74	0.59	0.53	2.06
Air	Quick	Air	1.61	0.51	0.38	0.31
Air	Quick	N_2	4.39	0.57	0.44	1.22
Air	Slow	Air	2.41	0.52	0.43	0.53
Air	Slow	N_2	7.08	0.56	0.54	2.11

This study shows P3HT:$PCBM_{DCB}$ devices can be spin coated in air and perform comparably to devices fabricated under a N_2 environment, however, the post-spin coating stages were very important. Slow drying the film was seen to increase both the *Jsc* and the *FF*. The slower evaporation rate due to covering the films during the drying process has been shown to allow the P3HT to self-organise and obtain a high degree of order, even when blended with PCBM. This increased crystallinity enhances the absorption and transportation resulting in a higher PCE.[45, 156]

A possible reason for the lower device performance for devices annealed in air compared to those annealed in N_2 could be due to the presence of oxygen traps in the air annealed P3HT:$PCBM_{DCB}$ films. The presence of oxygen has been shown to increase the rate of recombination of charge carriers in the P3HT:$PCBM_{DCB}$ film,[152,

[158] and annealing above 120 ºC has been reported to promote oxygen desorption.[159] Additionally, Guerrero *et.al.* showed that intentionally introducing oxygen doping to the P3HT:PCBM films after annealing, resulted in a decrease in both J_{sc} and *FF*.[160] So here, devices which were annealed in air were also allowed to cool to room temperature in air; therefore the P3HT:$PCBM_{DCB}$ film may become re-doped with oxygen negatively impacting both the J_{sc} and *FF*. For the rest of this chapter all devices that were spin coated in air were slow dried under a petri dish lid and annealed under N_2 for 20 minutes at 120 ºC.

4.1.3 Solution conditions

Next, the conditions under which the P3HT:$PCBM_{DCB}$ solution is made up were investigated. Two DCB solvents were used; one that was kept under N_2 and the other that was stored in air. The P3HT and PCBM were both stored under N_2. Three solutions were made up. For the first solution, P3HT and PCBM were mixed with DCB that was stored under N_2 and the solution was kept under N_2 until used for spin coating. The second solution consisted of transferring the relevant amounts of P3HT, PCBM and the DCB stored under N_2 out into air and mixing them together under ambient atmosphere. The third and final solution involved transferring P3HT and PCBM into air and these were mixed with the DCB solvent stored in air. Four device variations were made from these three P3HT:$PCBM_{DCB}$ solutions.

Two sets of devices were made up using the first solution. Devices were spin coated in N_2, fast dried and annealed under N_2 (N_2/N_2/N_2) to give a set of reference devices. This solution was also used to spin coat P3HT:$PCBM_{DCB}$ films in air (N_2/N_2/air).

Two other solutions were also spin coated onto ITO/PEDOT:PSS_{HTL} substrates. One was stored under N_2 and mixed and spin coated in air (N_2/air/air). The other was stored, mixed and spin coated in air (air/air/air). After spin coating in air all films were slow dried and annealed in N_2. **Figure 4.3.a** shows a comparison of the J-V curves for the four device variations and **Figure 4.3.b** shows a schematic of the different solution conditions.

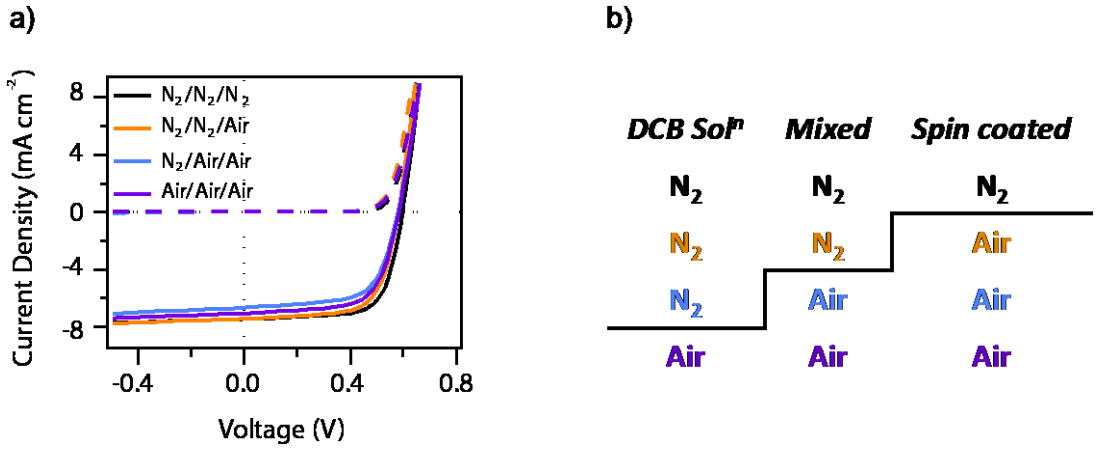

Figure 4.3 – a) J-V curves under 1 sun illumination (solid lines) and in the dark (dashed lines) for P3HT:$PCBM_{DCB}$ devices where the blend solution was processed under different conditions on an ITO/PEDOT:PSS_{HTL} electrode and b) schematic displaying the different processing conditions, with annealing under N_2 for all cells.

The $N_2/N_2/N_2$ devices obtained the best device performance with a J_{sc} of 7.42 mA cm^{-2}, a V_{oc} of 0.60 V and a *FF* of 0.70 resulting in a PCE of 3.11 % (**Table 4.3**). As shown in **Section 4.1.2** spin coating the (same) P3HT:$PCBM_{DCB}$ solution in air (N_2/N_2/air) leads to a slight decrease in device performance to a PCE of 2.91 %. The performance fell to 2.49 % for N_2/air/air devices. The PCE was also lower at 2.70 % for air/air/air devices.

Table 4.3 - OPV device parameters for P3HT:$PCBM_{DCB}$ devices where the blend solution was processed under different conditions on an ITO/PEDOT:PSS_{HTL} electrode.

Processing Sol^n/Mix/Spun	*J_{sc} (mA cm^{-2})*	*V_{oc} (V)*	*FF*	*PCE (%)*
$N_2/N_2/N_2$	7.42	0.60	0.70	3.11
N_2/N_2/air	7.41	0.58	0.67	2.91
N_2/air/air	6.63	0.58	0.65	2.49
Air/air/air	7.02	0.58	0.66	2.70

A decrease in device performance is seen when processing steps are carried out in air, mainly due to a reduction in J_{sc}. However, considering three different P3HT:$PCBM_{DCB}$ solutions were used for this comparison and batch-to-batch variation is expected between P3HT:$PCBM_{DCB}$ devices these results show that changing from a N_2 environment to an ambient atmosphere does not have a large impact on device performance. Not needing to store, mix and deposit the photoactive layer components under an inert environment should help to lower costs for mass production.

4.1.4 Optimised processing conditions

As demonstrated in the previous **Section 4.1 - 3**, spin coating in air, followed by slow drying and annealing under N_2 produced devices with comparable

performances to those completely fabricated in N_2 for ITO/PEDOT:PSS_{HTL} electrode based devices. This methodology was then applied to devices utilising PEDOT:PSS_{ADD} and PEDOT:PSS_{IMM} electrodes. Here, the DCB used was stored under N_2 and the P3HT and PCBM were also mixed under N_2. The same P3HT:$PCBM_{DCB}$ solution was used for devices made up entirely under N_2 and those that were spin coated in air. **Figure 4.4.a** displays the J-V curves for fast dried devices made up in N_2 and **Figure 4.4.b** shows devices using the optimised air fabrication conditions where P3HT:$PCBM_{DCB}$ films were spin coated in air, slow dried and then annealed under N_2.

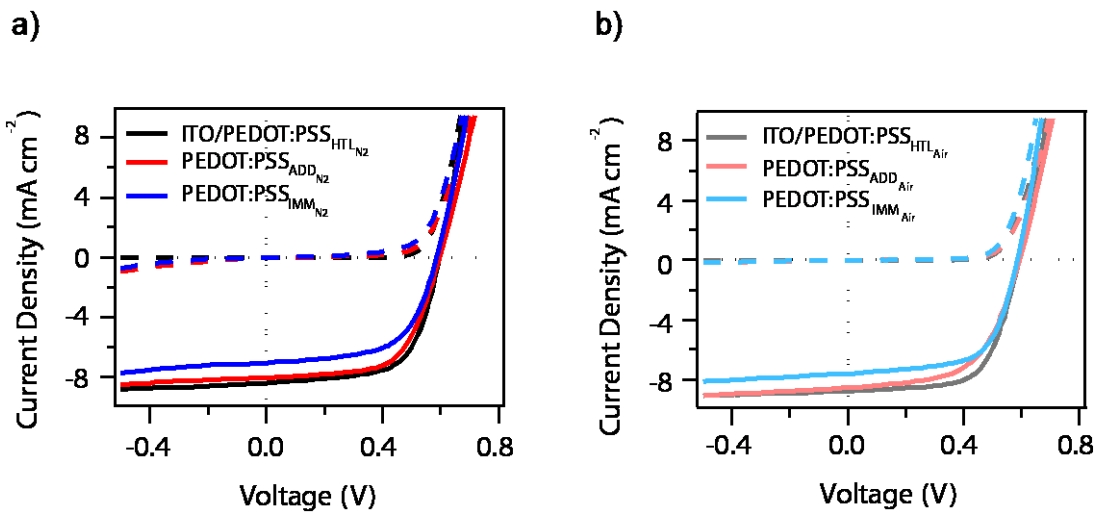

Figure 4.4 – J-V curves under1 sun illumination (solid lines) and in the dark (dashed lines) for P3HT:$PCBM_{DCB}$ devices using ITO/PEDOT:PSS_{HTL}, PEDOT:PSS_{ADD} and PEDOT:PSS_{IMM} fabricated in a) N_2 environment or b) optimised air processing conditions.

Table 4.4 shows the device parameters for P3HT:$PCBM_{DCB}$ devices fabricated under N_2 and in air on the three different electrodes. Devices using the ITO/PEDOT:PSS_{HTL} electrode obtained a similar device performance to that shown

in **Table 3.3.** PEDOT:PSS_{ADD} electrode based devices performed slightly better whereas devices using PEDOT:PSS_{IMM} electrodes had a poorer performance than before. It should be reiterated here that the devices made in **Section 3.1.5** were slow dried under N_2 and multiple devices were averaged over several months. Whereas here, only devices that were grown in the same batch were averaged. This means that the devices shown in this section cannot be truly compared to the ones in the previous chapter. However, (almost all) the device parameters in **Table 4.4** fall within the range shown in **Figure 3.8**.

Devices where the P3HT:$PCBM_{DCB}$ layer was spin coated in air performed comparably to those fabricated entirely under N_2. Interestingly, the J_{sc} for all the devices spin coated in air was higher. This may be due to the slower evaporation rate due to covering the films allowing the P3HT to rearrange to become more ordered. This increased crystallinity enhances absorption and so a larger J_{sc} was achieved.

Table 4.4 – OPV device parameters for P3HT:$PCBM_{DCB}$ devices using optimised air processing conditions on an ITO/PEDOT:PSS_{HTL}, PEDOT:PSS_{ADD} and PEDOT:PSS_{IMM} electrodes.

Electrode	*Atmosphere*	J_{sc} *(mA* cm^{-2}*)*	V_{oc} *(V)*	*FF*	*PCE (%)*
ITO/PEDOT:PSS_{HTL}	N_2	8.40	0.60	0.63	3.01
PEDOT:PSS_{ADD}	N_2	8.04	0.60	0.62	2.82
PEDOT:PSS_{IMM}	N_2	7.07	0.59	0.62	2.37
ITO	Air	8.78	0.59	0.64	3.16
PEDOT:PSS_{ADD}	Air	8.56	0.59	0.59	2.81
PEDOT:PSS_{IMM}	Air	7.60	0.58	0.63	2.60

4.1.5 Summary

This section has demonstrated that P3HT:$PCBM_{DCB}$ OPV devices deposited in air can perform comparably to those completely fabricated under a N_2 atmosphere, provided careful consideration is given to post-spin coating conditions. The post-spin coating conditions required are slow drying under a petri-dish in air followed by annealing at 120 ^{o}C under a N_2 environment. This process was shown to produce optimised performances for regular devices using ITO/PEDOT:PSS_{HTL}, PEDOT:PSS_{ADD} and PEDOT:PSS_{IMM} electrodes. This highlights the possibility of combining the solution processed electrode and photoactive layer deposition in an ambient roll-to-roll process. Being able to deposit the photoactive layer in an

ambient atmosphere should help minimise costs when moving to a large-scale fabrication set-up, since there is no need to house large spray deposition or printing equipment in an inert atmosphere.

4.2 Interfacial layers

This section explores the use of interfacial layers in conjunction with an ambient spin coated P3HT:PCBM photoactive layer. Firstly, the use of PEDOT:PSS_{HTL} and vacuum deposited MoO_x layers are compared using P3HT:$PCBM_{DCB}$ as a model system. This highlights the importance of choosing the appropriate interfacial layer, especially when depositing the photoactive layer under ambient conditions. The benefits of utilising an inverted architecture are then addressed and how this structure negates some of the issues seen in regular device structures is studied.

4.2.1 Hole transporting layers in regular architectures

So far, this chapter has focused on using PEDOT:PSS_{HTL} as an interfacial layer between the ITO electrode and the P3HT:$PCBM_{DCB}$ photoactive layer in regular device architectures. PEDOT:PSS is the most commonly used solution processed material for this role. There are, however, concerns over the electrical inhomogeneity originating from the PSS layer and device instability due to its acidic nature etching the ITO.[94] These issues have led to an interest to find alternative anode interfacial layers. A number of transition metal oxides such as MoO_x, WO_x and V_2O_x can successfully modify the anode interface. [55, 161] These metal oxides can be both solution processed and thermally evaporated to produce highly transparent films with moderate conductivity and favourable energetic alignment for hole extraction compared to ITO_{bare}. Inclusion of a metal oxide hole extracting layer has also been shown to improve device stability.[55]

Figure 4.5 shows the J-V curves of regular P3HT:$PCBM_{DCB}$ devices spin coated under N_2 and ambient atmospheres using either PEDOT:PSS_{HTL} or MoO_x as the anode interfacial layer. The 5 nm MoO_x layer was deposited by thermal evaporation onto pre-cleaned ITO_{bare} and transferred to air just before the P3HT:PCBM deposition. All P3HT:PCBM films were slow dried and then annealed at 120 ^oC under N_2. After annealing 8 nm of BCP was thermally evaporated on top followed by Al through a shadow mask.

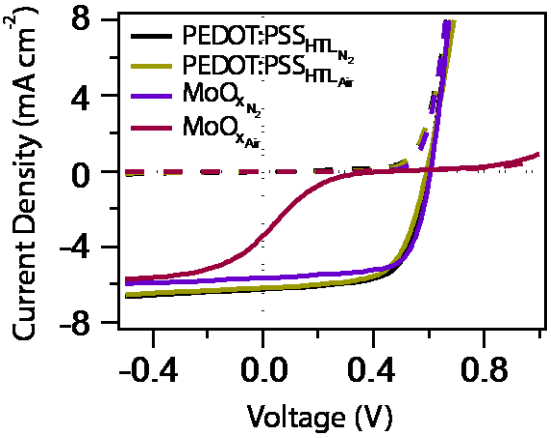

Figure 4.5 – J-V curves under 1 sun illumination (solid lines) and in the dark (dashed lines) of P3HT:$PCBM_{DCB}$ OPV devices spin coated under N_2 and air onto ITO/PEDOT:PSS_{HTL} or ITO/MoO_x.

The key device parameters are displayed in **Table 4.5**. As shown previously in **Section 4.1.4**, spin coating P3HT:$PCBM_{DCB}$ devices onto ITO/PEDOT:PSS_{HTL} display a similar device performance regardless of the atmosphere the photoactive layer is spin coated under. There is a just a slight decrease in the J_{sc} and *FF* when moving from fabricating under a N_2 to air atmosphere leading to a PCE of 2.49 % and 2.36% respectively. Devices fabricated under N_2 on ITO/MoO_x substrates produced a J_{sc} of 5.67 mA cm^{-2}, a V_{oc} of 0.61 V and a *FF* of 0.69, with a PCE of 2.49

%. This was comparable to the ITO/PEDOT:PSS_{HTL} electrode based devices that were also fabricated under a N_2 atmosphere. ITO/MoO_x electrode based devices processed in air, however, display very different J-V characteristics as can be seen by the s-shaped kink in **Figure 4.5**. These devices have a J_{sc} of 3.43mA cm^{-2}, a V_{oc} of 0.46 V and a *FF* of 0.12 resulting in an overall PCE of 0.19 %. These devices exhibit a kink before V_{oc} suggesting a contact issue at the MoO_x interface with the organic donor leading to an imbalance of charges. A decrease was seen in all device parameters and in particular the *FF* due to an increase in R_s. Studies have shown that exposing the MoO_x layer to an ambient environment cause the work function to decrease from 6.8 eV to 5.3 eV due to adsorption of water and other contaminants which appear to have a negative effect on charge transport.[162, 163] This indicates how important the choice of interfacial layer is, especially when fabricating device in an ambient atmosphere.

Table 4.5 – OPV device parameters for P3HT:$PCBM_{DCB}$ devices spin coated under N_2 and ambient atmospheres onto ITO/PEDOT:PSS_{HTL} and ITO/MoO_x electrodes.

Interlayer	*Atmosphere*	J_{sc} *mA* cm^{-2}	V_{oc} *(V)*	*FF*	*PCE (%)*
PEDOT:PSS_{HTL}	N_2	6.26	0.60	0.66	2.49
PEDOT:PSS_{HTL}	Air	6.19	0.59	0.64	2.36
MoO_x	N_2	5.67	0.61	0.69	2.49
MoO_x	Air	3.43	0.46	0.12	0.19

4.2.2 Inverted architectures

The main benefit of OPV devices is considered to be their low-cost potential and this is largely dependent on the high production predicted during manufacturing. Although OPV devices employing a regular device structure have successfully proven themselves under laboratory conditions, they do not meet the requirements for a commercially viable device because factors regarding fabrication upscale are not considered. To obtain the desired production speeds a roll-to-roll process is most likely needed. This would require flexible substrates and a completely solution processed deposition procedure since inclusion of vacuum deposited steps are likely to increase the cost unless very high speeds are achieved. Adopting an inverted architecture allows a greater variety of top contacts to be utilised. Such inverted devices can be manufactured on a large scale and under ambient conditions with various demonstrations highlighting the feasibility of using this architecture.[164-166]

Interfacial layers are important in OPV devices as they are used to tune the work function of the electrodes, and so by choosing the appropriate interfacial layer the charge extraction efficiency and selectivity can be altered. For inverted OPV devices the polarity of the device is reversed compared to those based on the regular device structures. Depositing a low work function n-type metal oxide semiconductor, such as ZnO or TiO_x, onto ITO enables the TCE to act as the electron extracting electrode.

The following inverted device structure was used: ITO/ZnO/P3HT:$PCBM_{DCB}$/MoO_x/Al. A low temperature sol-gel processed ZnO film was used as the electron extracting layer due to its high transparency, low cost,

high electron mobility and favourable energetics for electron extraction. Inserting a thermally evaporated hole extracting layer, such as MoO_x, has been shown to improve the device performance by improving the Ohmic contact between the photoactive layer and the metal electrode.[167]

The ZnO layer was directly spin coated on to pre-cleaned ITO_{bare} electrodes, then allowed to stand at room temperature for two minutes followed by annealing at 200 ^oC in air for an hour. The ZnO films were left to cool to room temperature before P3HT:$PCBM_{DCB}$ was spin coated on top in air, followed by slow drying and subsequent annealing under N_2. After annealing, 10 nm of MoO_x was thermally deposited onto the P3HT:$PCBM_{DCB}$ films followed by Al. **Figure 4.6** shows the J-V curves for these devices.

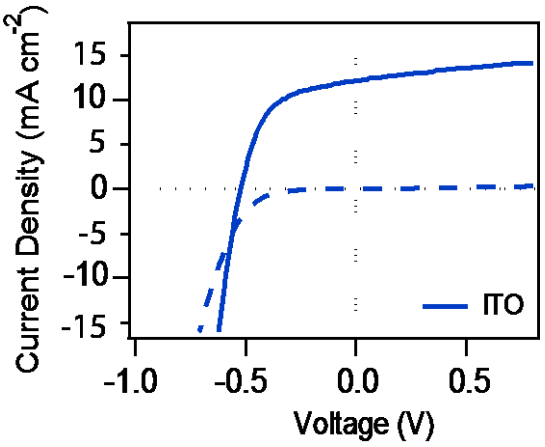

Figure 4.6 – J-V curves under 1 sun illumination (solid lines) and in the dark (dashed lines) of inverted P3HT:$PCBM_{DCB}$ OPV devices spin coated in air onto ITO/ZnO electrodes.

The key device parameters for inverted P3HT:$PCBM_{DCB}$ OPV devices fabricated on ITO/ZnO is displayed in **Table 4.6**. Devices produced a J_{sc} of 12.16 mA cm^{-2}, a V_{oc} of 0.52 V and a *FF* of 0.54 to give an overall PCE of 3.49 %.

Table 4.6 – OPV device parameters for inverted P3HT:$PCBM_{DCB}$ spin coated in air onto ITO/ZnO electrodes.

Electrode	J_{sc} *(mA* cm^{-2}*)*	V_{oc} *(V)*	*FF*	*PCE (%)*
ITO	12.16	0.52	0.54	3.49

The topography of ITO/MoO_x and ITO/ZnO are shown in **Figure 4.7**. Both films are quite smooth with a surface roughness of 2.0 nm and 1.2 nm respectively.

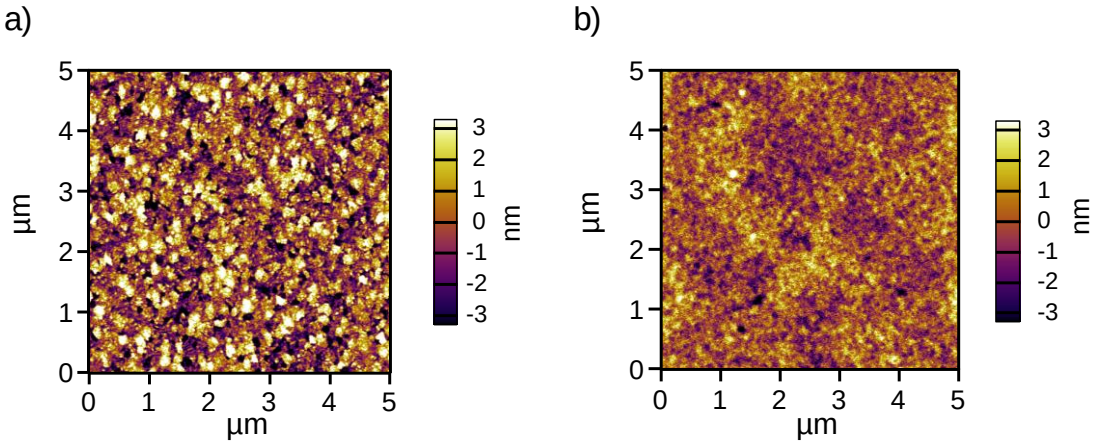

Figure 4.7 – AFM topography images of a) ITO/MoO_x and b) ITO/ZnO films.

4.2.3 Summary

This section has highlighted the importance of selecting an appropriate interfacial layer when processing the photoactive layer under ambient atmosphere. Materials, such as MoO_x, that work well under inert conditions, may hinder device performance when exposed to oxygen and moisture. An inverted device structure was also introduced. The sol-gel processed ZnO electron extracting layer and photoactive layer were deposited under ambient conditions. The resulting device displayed good OPV device behaviour.

4.3 Non-halogenated solvents

Since the aim is ultimately to be able to commercially produce inexpensive and large area roll-to-roll fabricated OPV devices some serious consideration towards the solvent the individual layers are cast from is needed. In general, halogenated solvents such as chlorobenzene (CB) and DCB, are used in polymer OPV devices due to their superior performance over other solvents. Although these are 'good' solvents in terms of achieving the best lab-scale devices, these solvents are not considered to be 'environmentally friendly'. They do not exist in nature, are expensive and energy-intensive to produce and dispose of, and there are serious concerns over their adverse impact on human health and the environment.[168] These concerns essentially rule out these solvents being used for mass production in industrial countries with strict environmental health and safety (EHS) legislation.[169] There is, therefore, an urgent need to find effective solvents to fabricate efficient OPV devices that are suitable for a rapid, ambient and large area commercial process.

Solvent choice and processing conditions play a vital part in obtaining the most effective BHJ device microstructure and at present, halogenated solvents are proven to be good at achieving this. In comparison, non-halogenated solvents produce significantly poorer microstructures and therefore device performance suffers due to their lower solubility for the polymer and fullerene components. [39] Studies have shown methylbenzenes such as toluene and xylene are promising potential alternatives to halogenated solvents. Unlike the energy intensive chlorobenzene production, methylbenzenes are obtained by distillation or solvent extraction from crude oil. They are also biodegradable and the EHS concerns are much lower than those associated with halogens. A major drawback with these solvents, however, is

their poor fullerene derivative solubility which leads to reduced device performance.[170] This section focuses on using non-halogenated solvents as the main solvent for P3HT:PCBM devices and utilises the ambient deposition process developed in **Section 4.1** (all films were spin coated in air, slow dried in air and then annealed under N_2).

4.3.1 Toluene

Toluene is already extensively used in industry (e.g. as a solvent for paint) which alongside its lower toxicity makes it a more preferable solvent for large scale processing. A significant amount of early work with MDMO-PPV:PCBM and P3HT:PCBM was carried out using toluene, until chlorinated solvents such as CB were found to produce smoother films and more efficient devices. The improvement in device performance was proposed to be due to the higher solubility of PCBM in CB.[39]

Both P3HT:$PCBM_{DCB}$ and P3HT:PCBM in toluene (P3HT:$PCBM_{Tol}$) solutions were prepared under N_2 in a similar manner. The P3HT:$PCBM_{DCB}$ solution was made up to a concentration of 20 mg ml^{-1} and the P3HT:$PCBM_{Tol}$ to a 13 mg ml^{-1} (1.5 wt-% of both) in a 1:1 ratio. Both solutions were left to stir at 40 ^oC on a hot plate for 24 hours and allowed to cool to room temperature before filtering with a 0.22 µm pore size PTFE filter. AFM was used to investigate the difference in morphology between P3HT:$PCBM_{DCB}$ and P3HT:PCBM films cast from toluene (P3HT:$PCBM_{Tol}$). **Figure 4.8** shows the major difference in topography between P3HT:$PCBM_{DCB}$ (**Figure 4.8.a**) and P3HT:$PCBM_{Tol}$ (**Figure 4.8.b**) films spin coated onto

ITO/PEDOT:PSS_{HTL}. P3HT:$PCBM_{DCB}$ films have a very smooth and featureless surface with a surface roughness of 2.2 nm (σ = 0.59 nm). A more fibre-like topography is seen on the surface of P3HT:$PCBM_{Tol}$ films. Although this solution was subjected to the same filtering conditions as the P3HT:$PCBM_{DCB}$ solution large crystalline clusters occur repeatedly over the P3HT:$PCBM_{Tol}$ film surface. This large-scale phase segregation results in these films having a have a much greater surface roughness of 53 nm (σ = 39 nm).

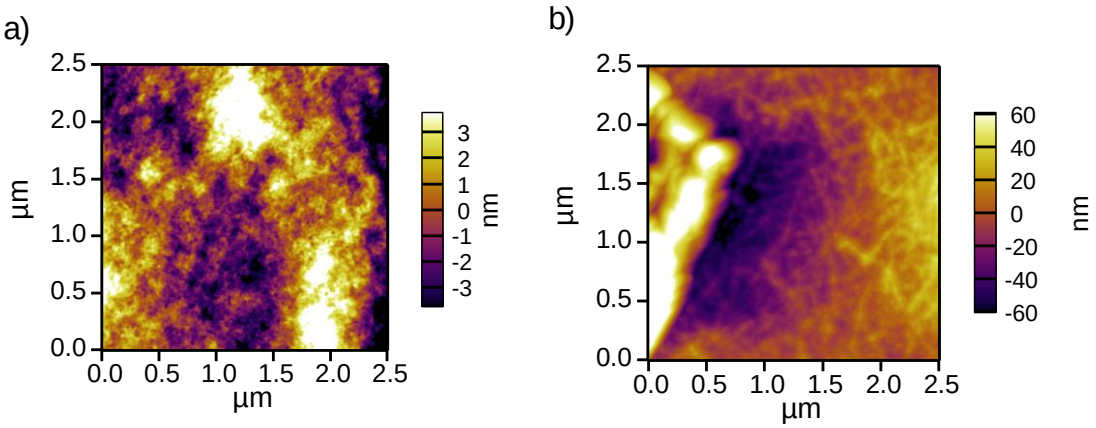

Figure 4.8 – AFM topography images of a) P3HT:$PCBM_{DCB}$ and b)P3HT:$PCBM_{Tol}$ films on ITO/PEDOT:PSS_{HTL} electrodes.

Similarly to toluene-cast MDMO-PPV:PCBM which also showed severe phase segregation, the large features are most likely to be PCBM-rich aggregates embedded in the P3HT.[171] The low solubility of PCBM in toluene is believed to be the cause of this severe phase segregation. These large features are likely to impact device performance as previously shown for MDMO-PPV:PCBM cast from toluene.[39, 171]

The absorbance of P3HT:$PCBM_{DCB}$ and P3HT:$PCBM_{Tol}$ films is shown in **Figure 4.9**. P3HT:$PCBM_{DCB}$ films show a much larger contribution from both P3HT and PCBM than P3HT:$PCBM_{Tol}$ films. P3HT:$PCBM_{DCB}$ films obtain an absorption of 0.56 a.u. at 525 nm compared to 0.37 a.u. for P3HT:PCBM at the same wavelength. The absorption could be lower for P3HT:$PCBM_{Tol}$ films because of the lower P3HT and PCBM solubility in toluene. This means that a significant amount of material had not dissolved and was lost through filtering. This also happened when the solution was left to stir for a prolonged time and even when the solution was heated while being stirred.

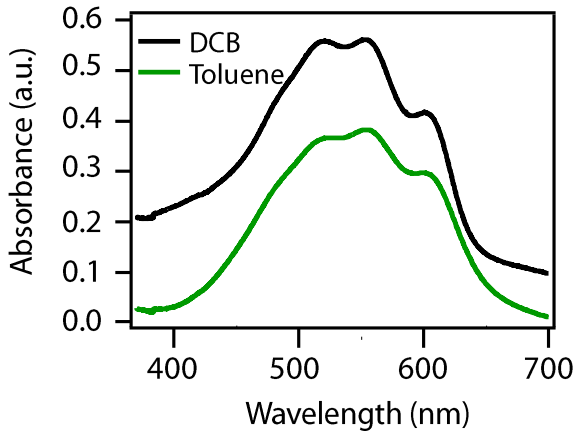

Figure 4.9 – Absorbance spectra of P3HT:$PCBM_{DCB}$ and P3HT:$PCBM_{Tol}$ films on ITO/PEDOT:PSS_{HTL} electrodes.

P3HT:$PCBM_{Tol}$ devices were spin coated (1000 RPM) under N_2 and in air and compared to those using P3HT:$PCBM_{DCB}$. The same P3HT:$PCBM_{DCB}$ and P3HT:$PCBM_{Tol}$ solutions were used for devices spin coated in N_2 and air on ITO/PEDOT:PSS_{HTL} electrodes. **Figure 4.10.a** displays the J-V curves for the devices. The corresponding EQE spectra are also shown (**Figure 4.10.b**).

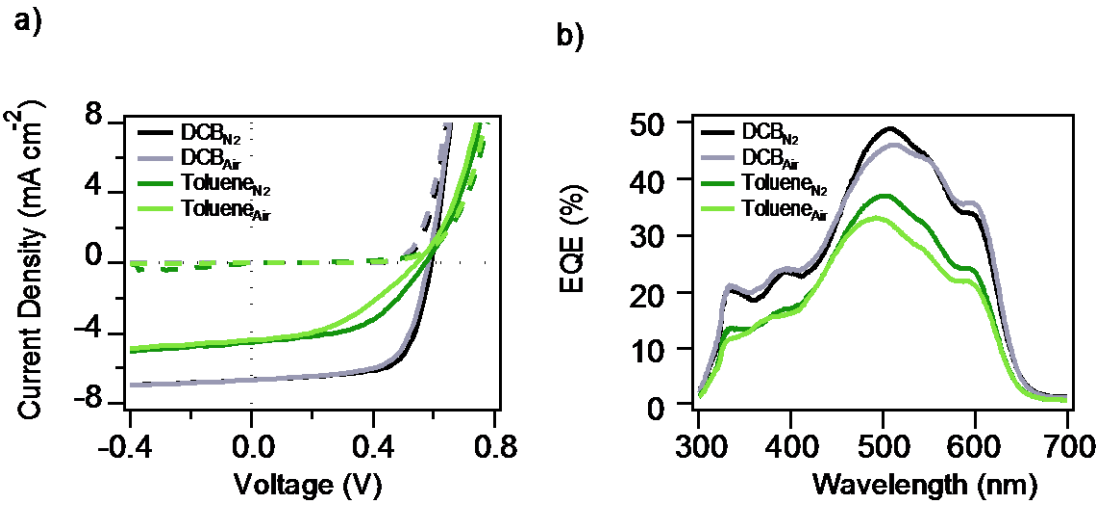

Figure 4.10 – a) J-V curves under 1 sun illumination (solid lines) and in the dark (dashed lines) and b) EQE spectra for P3HT:PCBM$_{DCB}$ and P3HT:PCBM$_{Tol}$ devices processed in N_2 and air.

Using toluene as a solvent for P3HT:PCBM has a huge impact on the device performance (**Table 4.7**), with device PCE less than half that of devices using DCB. Again, as seen in **Chapter 4.1**, P3HT:PCBM$_{DCB}$ devices spin coated under N_2 and air produced very similar device performances with a PCE of 2.66 % and 2.52 % respectively. P3HT:PCBM$_{Tol}$ devices spin coated in N_2 had a J_{sc} of 4.52 mA cm^{-2}, a V_{oc} of 0.57 V and a *FF* of 0.50 resulting in a PCE of 1.29 %. Whereas P3HT:PCBM$_{Tol}$ devices spin coated in air obtained a lower PCE of 1.00 %, with a J_{sc} of 4.34 mA cm^{-2}, a V_{oc} of 0.54 V and a *FF* of 0.42.

Table 4.7 - OPV device parameters for P3HT:PCB_{DCB} and P3HT:$PCBM_{Tol}$ devices spin coated in N_2 or optimised air processing conditions using an ITO/PEDOT:PSS_{HTL} electrode.

Solvent	*Atmosphere*	J_{sc} *(mA cm^{-2})*	V_{oc} *(V)*	*FF*	*PCE (%)*
DCB	N_2	6.68	0.59	0.68	2.66
DCB	Air	6.68	0.58	0.65	2.52
Toluene	N_2	4.52	0.57	0.50	1.29
Toluene	Air	4.34	0.54	0.42	1.00

The main difference in device performance between devices spin coated from DCB and toluene is due to a decrease in J_{sc} for P3HT:$PCBM_{Tol}$ devices. A possible reason for this is the decreased absorption seen for P3HT:$PCBM_{Tol}$ films (**Figure 4.9**). It is possible that P3HT:$PCBM_{Tol}$ films do not wet as well on PEDOT:PSS which could results in thinner films. Previous studies have also shown that using CB instead of toluene resulted in an increase in both J_{sc} and *FF*. [39] This was attributed to a finer grain size in film microstructure. The larger scale phase segregation for toluene cast photoactive layers (**Figure 4.8**) is generally understood to be the main reason for the reduction in J_{sc} when compared to CB or DCB cast films and is usually attributed to the lower solubility of the fullerene in toluene.

4.3.2 Toluene:1-methylnaphthalene

The main drawback of using toluene as a solvent is its poor PCBM solubility, which ultimately limits the device performance. It is therefore important to increase PCBM solubility. Mixing two solvents has been shown to be a popular way to help control the microstructure of polymer:fullerene blends. This method has been shown to improve the device performance of many different polymer:fullerene systems with different solvent combinations.[170, 172] 1-Methylnaphthalene was trialled as an additive in P3HT:$PCBM_{Tol}$ as it has a high fullerene solubility (33 mg ml^{-1}) and it is known to be a good fullerene solvent which is also used as a solvent in fullerene chemical reactions.[173-175] 1-Methylnaphthalene has a higher boiling point (240 ^{o}C) than toluene (110 ^{o}C) and thereby retards the evaporation from the photoactive layer during deposition.

AFM was again used to investigate the effect of adding a small amount of 1-methylnaphthalene to the P3HT:$PCBM_{Tol}$ solution on the topography of the film (P3HT:$PCBM_{TolMeN}$). **Figure 4.11.a-c** shows the AFM topography images of P3HT:PCBM dissolved in toluene with 1 vol-% 1-methylnaphthalene (P3HT:$PCBM_{TolMeN1\%}$), 5 vol-% 1-methylnaphthalene (P3HT:$PCBM_{TolMeN5\%}$), and 9 vol-% 1-methylnaphthalene (P3HT:$PCBM_{TolMeN9\%}$), added to the solution respectively. A change in the film wetting on the ITO/PEDOT:PSS_{HTL} substrates and drying times were seen with increasing 1-methylnaphthalene amounts. As the volume of 1-methylnaphthalene was increased the films did not wet the surface as well and the drying time increased. Again, like with the P3HT:$PCBM_{Tol}$ films, films with 1-methylnaphthalene added have high surface roughness. Large crystalline clusters are distributed across the surface of the P3HT:$PCBM_{TolMeN1\%}$ films resulting

in a surface roughness of 25.9 nm (σ = 20.4 nm). P3HT:PCBM$_{TolMeN5\%}$ films appeared to dry slower than P3HT:PCBM$_{TolMeN1\%}$ films, probably because the films contains a larger amount of the higher boiling point 1-methylnaphthalene solvent. These films had a similar surface roughness to P3HT:PCBM$_{TolMeN1\%}$ films but smaller standard deviation of 26.9 nm (σ = 11.2 nm), however these films had a more homogeneous surface and large crystalline regions were not observed for these films. P3HT:PCBM$_{TolMeN9\%}$ films dried very slowly and were visibly inhomogeneous with areas of the substrate not completely covered. Large crystalline features were again observed as well as some smaller more needle like features, producing in a surface roughness of 49.6 nm (σ = 40.2 nm). **Figure 4.11.d** shows the absorbance spectra for the three P3HT:PCBM$_{TolMeN}$ films. A similar absorbance spectra to P3HT:PCBM$_{DCB}$ and P3HT:PCBM$_{Tol}$ films is seen for these films (**Figure 4.9**). P3HT:PCBM$_{TolMeN5\%}$ films have the highest absorbance of 0.57 a.u. at 525 nm and the partial P3HT:PCBM$_{TolMeN9\%}$ film has the lowest absorbance of 0.33 a.u.

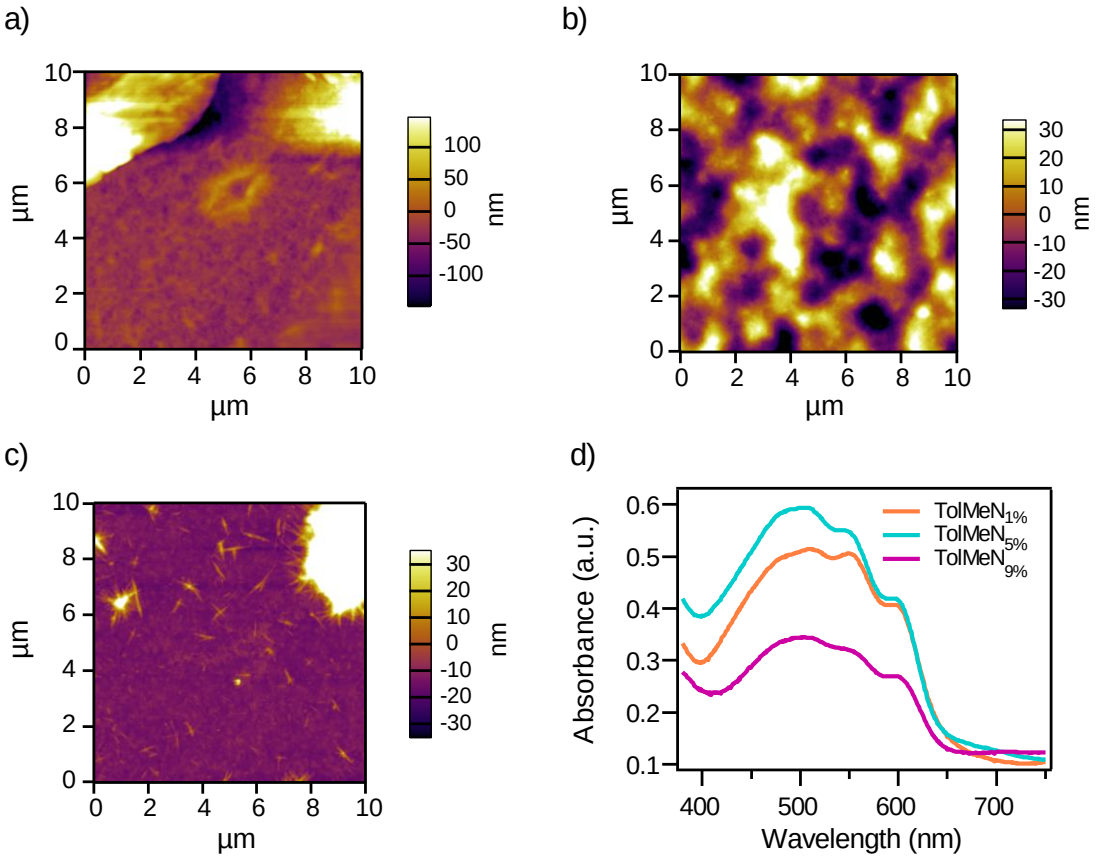

Figure 4.11 - AFM topography images of a) P3HT:PCBM$_{TolMeN1\%}$, b) P3HT:PCBM$_{TolMeN5\%}$ and c) P3HT:PCBM$_{TolMeN9\%}$ films on ITO/PEDOT:PSS$_{HT}$ and d) the absorbance spectra of P3HT:PCBM$_{TolMeN}$ films. All PEDOT:PSS$_{TolMeN}$ films were spin coated onto ITO/PEDOT:PSS$_{HTL}$ electrodes.

P3HT:PCBM$_{TolMeN}$ films were spin coated (1000 RPM) onto ITO/PEDOT:PSS$_{HTL}$ substrates in air, followed by slow drying and then annealing in N_2. The J-V curves for these devices are shown in **Figure 4.12.a** and the EQE spectra in **Figure 4.12.b**.

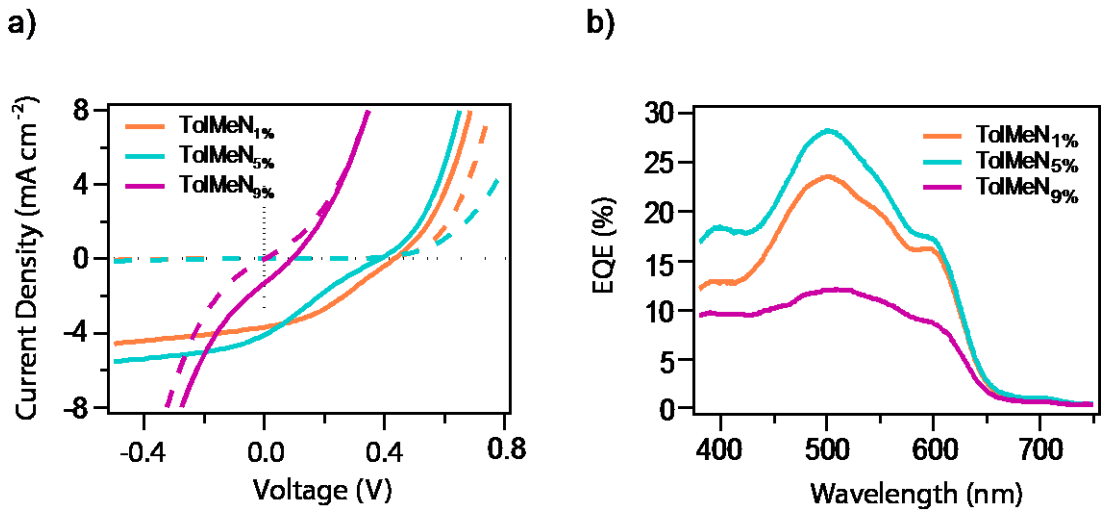

Figure 4.12 – a) J-V curves under 1 sun illumination (solid lines) and in the dark (dashed lines) and b) EQE spectra for P3HT:PCBM$_{TolMeN}$ OPV devices.

P3HT:PCBM$_{TolMeN}$ devices display very different device performances (**Table 4.8**) compared to P3HT:PCBM$_{Tol}$ devices (**Table 4.7**), with a reduction in all device parameters and a visible kink in the light curve before V_{oc}. P3HT:PCBM$_{TolMeN1\%}$ devices produced a J_{sc} of 3.68 mA cm^{-2}, a V_{oc} of 0.43 V and a *FF* of 0.35 to give an overall PCE of 0.54 %, just under half that obtained for P3HT:PCBM$_{Tol}$ devices (**Table 4.8**). As might be expected from the absorbance spectra, P3HT:PCBM$_{TolMeN5\%}$ devices produced the largest J_{sc} of 4.10 mA cm^{-2}, but had a lower V_{oc} of 0.38 V and lower *FF* of 0.23 resulting in a *FF* of 0.36 %. P3HT:PCBM$_{TolMeN9\%}$ devices, which produced poor quality films, obtained the lowest PCE of 0.03 %, with a J_{sc} of 1.31 mA cm^{-2}, a V_{oc} of 0.09 and a *FF* of 0.27.

S-shape kinks in J-V curves have been seen before for P3HT:PCBM active layers.[176-179] There is not, however, a single cause for these non-ideal J-V characteristics. Among the suggested causes are bulk effects such as an imbalance of the electron

and hole mobilities, energetic offsets at electrode interfaces and vertical phase distribution which has been shown to have an effect in some cases but not in others. In the case here, a s-shape kink is seen for P3HT:$PCBM_{TolMeN}$ but not P3HT:$PCBM_{Tol}$ devices. It is possible that the addition of 1-methylnaphthalene causes a change in the P3HT and PCBM vertical phase distribution. The fullerene component is more soluble in 1-methylnaphthalene and so the PCBM could be driven to the bottom of the film, away from the cathode.[180] If more PCBM is found at the ITO/PEDOT:PSS_{HTL} interface there could be a greater barrier to hole extraction since holes are mainly transported thought the P3HT phase. If holes cannot be extracted as easily as electrons, a significant space-charge develops within the photoactive layer and could lead to s-shaped kinks in the J-V curve.[177, 181, 182]

Table 4.8 – OPV device parameters for P3HT:$PCBM_{TolMeN}$ devices using an ITO/PEDOT:PSS_{HTL} electrode.

Solution	J_{sc} *(mA* cm^{-2}*)*	V_{oc} *(V)*	*FF*	*PCE (%)*
$TolMeN_{1\%}$	3.68	0.43	0.35	0.54
$TolMeN_{5\%}$	4.10	0.38	0.23	0.36
$TolMeN_{9\%}$	1.31	0.09	0.27	0.03

4.3.3 Summary

This section has shown that P3HT:PCBM films cast from toluene have a higher surface roughness and a more unfavourable microstructure than those cast from

DCB. The unfavourable microstructure and poor absorption of P3HT:$PCBM_{Tol}$ films are attributed to the reduced device performance compared to DCB cast devices.

Adding a small amount of 1-methylnaphthalene to the toluene solution did not visibly improve the solubility and a large amount of material was still lost through filtering. The P3HT:$PCBM_{TolMeN}$ films were still very rough, although the surface roughness was lower than P3HT:$PCBM_{Tol}$ films. A further decrease in device performance was seen along with non-ideal device behaviour. It is possible that there is an energetic barrier at the photoactive layer/electrode interface which leads to inefficient charge extraction.

4.4 Non-halogenated solvents in inverted devices

As previously mentioned (**Section 4.2.2**) there are several advantages to using an inverted architecture, especially when considering the practicalities of a commercial process. This section firstly compares the device performance of several non-halogenated solvents for P3HT:PCBM photoactive layers in inverted architectures. The section finishes by looking at replacing the vacuum deposited MoO_x hole extracting layer with a solution processed PEDOT:PSS layer in a further step towards a fully solution processed OPV device. All devices followed the ambient deposition process developed in **Section 4.1**, so all P3HT:PCBM photoactive layers were spin coated in air, slow dried and then transferred into the glovebox for annealing under N_2.

4.4.1 Solvent comparison

A larger amount of 1-methylnaphthalene was mixed with toluene to give a mixture consisting of 70 % toluene:30 % 1-methylnaphthalene ($TolMeN_{30\%}$) (optimised in other work). **Figure 4.13** shows the AFM topography images of the resulting $P3HT:PCBM_{TolMeN30\%}$ films on ITO/ZnO substrates. The $P3HT:PCBM_{TolMeN30\%}$ films had a surface roughness of 14 nm and no large aggregates were observed.

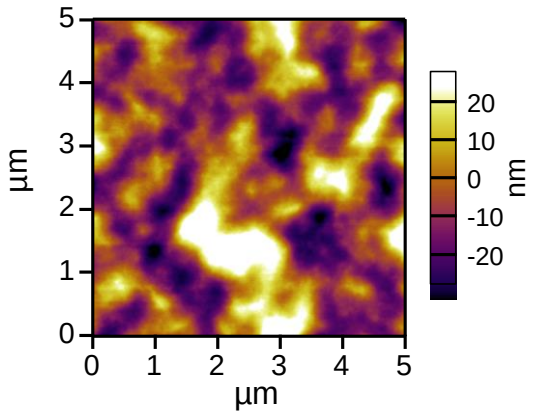

Figure 4.13 – AFM topography image of P3HT:PCBM$_{TolMeN30\%}$ films on ITO/ZnO substrates.

The device performance of inverted P3HT:PCBM devices spin coated (1600 RPM) from different solvents are shown in **Figure 4.14**. The solvents used were DCB, toluene (Tol), 70% tolunene:30 % 1-methylnaphthalene (TolMeN$_{30\%}$) and 1-methylnaphthalene (MeN) all with following device structure: ITO/ZnO/P3HT:PCBM$_{solvent}$/MoO$_x$/Al.

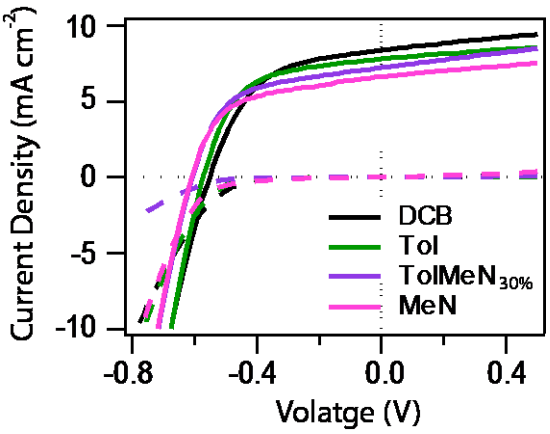

Figure 4.14 – J-V curves under 1 sun illumination (solid lines) and in the dark (dashed lines) of inverted P3HT:PCBM devices using different solvents on ITO/ZnO electrodes.

The key device parameters are displayed in **Table 4.9**. Devices using a halogenated solvents photoactive layer, P3HT:$PCBM_{DCB}$, obtained a J_{sc} of 8.35 mA cm^{-2}, a V_{oc} of 0.55 V and a *FF* of 0.52 resulting in a PCE of 2.52 %. Devices using non-halogenated solvents produced comparable device performance, with P3HT:$PCBM_{Tol}$ devices producing a PCE of 2.65 % with a J_{sc} of 7.77 mA cm^{-2}, a V_{oc} of 0.57 V and a *FF* of 0.57. P3HT:$PCBM_{TolMeN}$ devices produced a J_{sc} of 7.21 mA cm^{-2}, a V_{oc} of 0.61 V and a *FF* of 0.56 giving a PCE of 2.55 %. Devices with 1-methylnaphthalene as the solvent, P3HT:$PCBM_{MeN}$ had a J_{sc} of 6.61 mA cm^{-2}, a V_{oc} of 0.61 V and a *FF* of 0.56 giving a PCE of 2.36 %.

Upon changing from a halogenated to non-halogenated solvents the V_{oc} increases from 0.55 V for DCB to 0.57 V for toluene and 0.61 V for toluene:1-methylnaphthalene and 1-methylnaphthalene. A possible reason for this increase in V_{oc} is attributed to the change in the film morphology that is seen with different solvents (**Figure 4.8** and **Figure 4.11**). Annealing studies show that improving the crystallinity of the P3HT phase increases the hole mobility and so results in an increase in J_{sc}.[183] This improved crystallinity also causes a decrease in the V_{oc} of the P3HT:PCBM devices.[44, 184, 185] In the case here, it is possible that the P3HT phases are less crystalline when changing from DCB to a non-halogenated solvent, particularly those incorporating 1-methylnaphthalene as a (co)solvent, leading to a slightly larger V_{oc}.

Table 4.9 – OPV device parameters for inverted P3HT:PCBM devices using different solvents.

Solvent	J_{sc} *(mA cm^{-2})*	V_{oc} *(V)*	*FF*	*PCE (%)*
DCB	8.35	0.55	0.52	2.52
Tol	7.77	0.57	0.57	2.65
$TolMeN_{70\%}$	7.21	0.61	0.56	2.55
MeN	6.61	0.61	0.56	2.36

4.4.2 Development towards fully solution processed OPV devices

So far the top electrode and hole extracting layer have been deposited by thermal evaporation. When looking to move towards large volume production, the top interfacial layer and electrode ideally should also be solution processed as well.

As well as being used as a hole transport layer in regular architecture devices, PEDOT:PSS has also been used as a interfacial layer in inverted structures. However, additives have to be added to the PEDOT:PSS solution in order to improve the wettability of this layer on the polymer:fullerene blend.[186-188] Improvements in the material properties during the manufacturing process of PEDOT:PSS (Clevios HTL Solar, $PEDOT:PSS_{Solar}$) has seen it emerge as an effective interfacial layer between the photoactive layer and Al top electrode without the need for further treatment (**Figure 4.15**). $P3HT:PCBM_{DCB}$ was used as the

photoactive layer which was spin coated onto ITO/ZnO electrodes. The devices had the following structure: ITO/ZnO/P3HT:PCBM$_{DCB}$/PEDOT:PSS$_{Solar}$/Al.

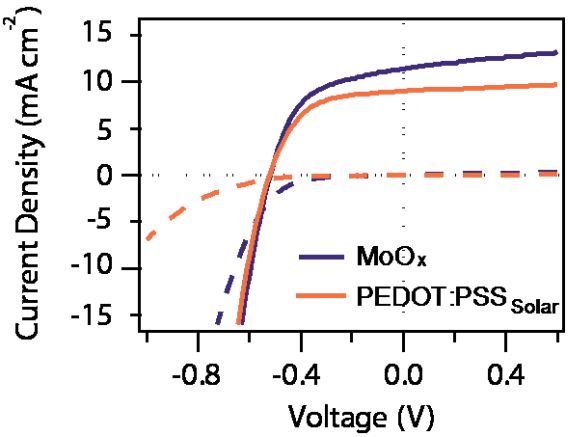

Figure 4.15 – J-V curves under 1 sun illumination (solid lines) and in the dark (dashed lines) of inverted P3HT:PCBM$_{DCB}$ devices on ITO/ZnO electrodes. Either MoO$_x$ or PEDOT:PSS$_{Solar}$ as an interfacial layer.

The key devices parameters are shown in **Table 4.10**. Devices utilising a MoO$_x$ interfacial layer produced a J_{sc} of 11.46 mA cm^{-2}, a V_{oc} of 0.52 V and a *FF* of 0.55 resulting in a PCE of 3.06 %. Those devices using a PEDOT:PSS$_{Solar}$ hole transporting layer had a lower PCE of 2.45 % with a J_{sc} of 9.03 mA cm^{-2}, V_{oc} of 0.52 V and a *FF* of 0.56. The difference in device performance is due to the lower J_{sc} obtained by devices using PEDOT:PSS$_{Solar}$, most likely due to the thicker and less transparent PEDOT:PSS$_{Solar}$ layer. With further processing optimisation of the PEDOT:PSS$_{Solar}$ layer the J_{sc} could be further improved. The V_{oc} obtained for both sets of devices are comparable to what was achieved in **Section 4.2.2** and the *FF* for both anode interfacial materials is also similar.

Table 4.10 – OPV device parameters for inverted P3HT:PCBM devices comparing different anode interfacial layers.

Interlayer	J_{sc} *(mA cm^{-2})*	V_{oc} *(V)*	*FF*	*PCE (%)*
MoO_x	11.46	0.52	0.55	3.06
PEDOT:PSS_{Solar}	9.03	0.52	0.56	2.45

4.4.3 Summary

This section has highlighted the feasibility of casting the photoactive P3HT:PCBM layer out of non-halogenated solvents. Inverted P3HT:PCBM devices using different non-halogenated solvents were seen to produce PCEs comparable to those using DCB as the solvent. P3HT:$PCBM_{Tol}$ devices were even seen to have a higher PCE than P3HT:$PCBM_{DCB}$ devices in the inverted architecture unlike, the poor performance seen for regular architecture devices using P3HT:$PCBM_{Tol}$ in **Section 4.3.1**.

In a step to move towards a fully solution processed device, the MoO_x hole extraction layer was replaced by PEDOT:PSS_{Solar} in inverted structures. These P3HT:$PCBM_{DCB}$ devices showed promising device performance and with further optimisation the decreased J_{sc} can most likely be improved.

4.4 Conclusions

With OPV devices attracting significant attention as a promising cheap and alternative renewable energy source; attention is needed as to how this low-cost potential will be reached. In order to meet the rapid production speeds required a predominantly ambient atmosphere is favourable with the majority of the individual layers being solution processed from environmentally friendly solvents via a roll-to-roll process. The beginning of this chapter addressed the possibility of fabricating a P3HT:$PCBM_{DCB}$ device entirely under ambient conditions. In air a huge decrease in the device performance was seen, largely due to reductions in J_{sc} and FF. Careful consideration of the post-spin coating conditions enabled the device performance of the air deposited devices to reach that of those spin coated under N_2. However, it was discovered that annealing had to be carried out under N_2.

A comparison of PEDOT:PSS_{HTL} and MoO_x interfacial layers as the hole extracting layer in regular devices highlighted the importance of selecting the appropriate material for the processing environment. A reduction in device performance was seen for regular devices using a MoO_x hole extracting layer. This was attributed to poor charge extraction due to exposing the layer to air. Inverted devices using an ambient processed ZnO electron extracting layer and MoO_x hole transporting layer (not exposed to air) displayed good OPV performance.

Replacing the DCB casting solvent with toluene resulted in decreased device performance in regular architecture devices. The decrease was attributed to the low absorption and poorer fullerene solubility in toluene. This led to severe phase segregation and large aggregate formation which has been reported to hinder charge

generation and increase recombination. To improve the fullerene solubility 1-methylnaphthalene was used as an additive in the toluene parent solvent. The device performance decreased with this addition and the formation of a kink suggested there was a problem with charge extraction.

Inverted OPV devices have shown promise to lending themselves to possible large scale fabrication as they can be processed in air from non-halogenated solvents and show favourable device performance compared to DCB based devices. Finally, the use of PEDOT:PSS_{Solar} as a hole transporting layer for inverted devices was compared to those using thermally evaporated MoO_x. The main difference in device performance was due to a lower J_{sc} seen for those using the thicker PEDOT:PSS_{Solar} layer, future work should allow this layer to be further optimised and so improve device performance. The next step would be to investigate the use of Ag inks (either as a full layer or grid) or even PEDOT:PSS_{ADD} as a top electrode to produce a fully solution processed OPV device.

Chapter 5. Conclusions and future work

OPV devices are attracting significant attention due to their perceived capability to become a low cost sustainable power source. The ability to solution process layers is a significant advantage over existing inorganic devices. Progress in recent years has led to a continual increase in device efficiencies and material stability. However other steps such as material and processing cost still need further attention before OPV devices can become commercially competitive with existing renewable energy technologies. This section draws some final conclusions and discusses possible avenues to take this work further.

This thesis was split into two parts. The first considered the use of PEDOT:PSS as an alternative to the more commonly used ITO electrode. Two different treatments were used to improve the conductivity of PEDOT:PSS thin film and two different deposition techniques were investigated. The second part looked at different processing conditions for P3HT:PCBM devices. The effect of processing the photoactive and interfacial layers under an ambient environment was studied. The use of non-halogenated solvents in both regular and inverted architectures then followed.

5.1 PEDOT:PSS as an alternative electrode to ITO

Chapter 3 discussed the possibility of using a solution processable TCE, PEDOT:PSS, instead of ITO. The ability to solution process the TCE would be a major advantage for OPV devices and would provide the potential for cost effective fabrication via a roll-to roll process.

5.1.1 Spin coated PEDOT:PSS electrodes

The conductivity of PEDOT:PSS thin films was enhanced by the use of two different DMSO treatments, with a similar improvement in R_{sheet} seen for both methods. Several different characterisation techniques were used to allow further insight into the effect DMSO had on the PEDOT:PSS electrode. Immersing PEDOT:PSS films in DMSO removed excess PSS from the near surface region of the film leading to a more homogeneous and conductive surface. Adding DMSO to the PEDOT:PSS solution is thought to result in the PEDOT and PSS rearranging into a more favourable conformation.

A well characterised photoactive system, P3HT:PCBM BHJ, was then used to study the effect both treatments had on the resulting OPV device performance. OPV devices using PEDOT:PSS_{IMM} electrodes slightly out performed those using PEDOT:PSS_{ADD} electrodes mainly due to an increased J_{sc}. This promising device performance for DMSO treated PEDOT:PSS, electrodes combined with their lower cost, indicate the possibility of using PEDOT:PSS as an alternative TCE in roll-to-roll processed OPV devices. It also highlighted that small differences in the

electrode surface may make certain treatments more favourable than others for different photoactive systems.

5.1.2 Spray deposited PEDOT:PSS electrodes

PEDOT:PSS_{ADD} electrodes were then used to compare two different solution processing techniques. PEDOT:PSS_{ADD} electrodes were chosen due to the ease and speed at which they could be fabricated. Spray deposited PEDOT:PSS electrodes had a significantly higher surface roughness than spin coated electrodes, however a similar distribution in topographical current distribution was seen. This indicated a similar distribution of PEDOT and PSS on the electrode surface.

Spray deposited PEDOT:PSS_{ADD} electrodes in CuPc/C_{60} bilayer devices produced a comparable PCE to those utilising a spin coated electrode, even with the increased surface roughness. A reasonable PCE was also obtained when compared to devices using an ITO electrode. The transparency and R_{sheet} of the spray deposited PEDOT:PSS_{ADD} electrodes could be easily tailored, which directly influenced the device parameters. This emphasises the potential for spray deposition as a low-cost method for rapid fabrication of PEDOT:PSS_{ADD} electrodes.

5.1.3 PEDOT:PSS electrodes in larger active area devices

Next, both spin coated and spray deposited PEDOT:PSS_{ADD} electrodes were used in SubPc/C_{60} bilayer devices with an increased active area. For both ITO and (spin coated and spray deposited) PEDOT:PSS_{ADD} electrodes increasing the active area

resulted in an increase in $R_{s,}$ and therefore a decrease in PCE. The lower R_{sheet} of the PEDOT:PSS electrodes led to these being more affected by the increase in active area than the ITO electrodes. Again, spray deposition proved to be a useful deposition technique where the film characteristics were easily tailored, highlighting its potential application in large area inexpensive OPV device fabrication.

5.2 P3HT:PCBM device processing conditions

Chapter 4 looked at some of the processing conditions involved in fabricating P3HT:PCBM devices. The ability to fabricate layers in air, including the photoactive layer, would be a significant advantage as this would help decrease manufacturing costs. The use of non-halogenated solvents would lower costs further as expensive disposal methods are not required. Additionally, the health and environmental implications of non-halogenated solvents are less severe.

5.2.1 Air processing

The P3HT:PCBM photoactive layer, spin coated on to ITO, was entirely fabricated in air, including the drying and annealing steps. This resulted in poor device performance which was probably a result of oxygen diffusing into the photoactive layer resulting in oxygen trap sites. Moving the annealing stage into an inert atmosphere considerably increased the device performance, as did allowing the photoactive layer to dry slowly. Spin coating the photoactive layer in air, slow drying in air before transferring the film into a N_2 filled glovebox followed by annealing under N_2 resulted in devices with a comparable efficiency to those where the photoactive layer was fabricated entirely under N_2. These processing conditions were also applicable to P3HT:PCBM devices using PEDOT:PSS_{ADD} and PEDOT:PSS_{IMM} electrodes. This suggests it could be possible to combine the electrode and photoactive layer in a roll-to-roll process under an ambient atmosphere. The optimised air processed method for P3HT:PCBM photoactive layer deposition was then used for the rest of the chapter.

5.2.2 Device architecture

Processing the photoactive layer in air also requires careful interfacial layer selection. The performance of devices utilising a regular architecture was severely hampered when P3HT:PCBM was spin coated on to a MoO_x electron extracting layer in air. This was possibly a result of adsorption of contaminants which reduced charge transport.

An inverted device architecture is thought to be more applicable for a roll-to-roll process as it should be possible to solution process all layers, including the top electrode. A ZnO layer, spin coated in air, was used as the electron extracting layer and the P3HT:PCBM photoactive layer was also subsequently spin coated in air. MoO_x was used as the hole extracting layer and was not exposed to air. The resulting devices gave a high PCE. This emphasised the importance of choosing an appropriate interfacial layer when fabricating devices under an ambient atmosphere.

5.2.3 Non-halogenated solvents

Although halogenated solvents result in high efficiency devices, they are not considered environmentally friendly and are not suitable for use in a mass production process. P3HT:PCBM photoactive layers spin cast out of toluene had a much higher surface roughness than those cast from DCB and devices had a lower PCE. This was attributed to the lower solubility of PCBM in toluene. This was thought to cause a larger phase segregation and a change in the transport properties of the P3HT:$PCBM_{Tol}$ films.

A small amount of 1-methylnaphthalene (1 vol-%, 3 vol-% and 5 vol-%) was combined with the primary toluene solvent to try and improve the PCBM solubility. Again, all P3HT:$PCBM_{TolMeN}$ films had a higher surface roughness than those spin cast out of DCB. The performance for P3HT:$PCBM_{TolMeN}$ devices was quite poor and non-ideal J-V characteristics were observed which were not seen for P3HT:$PCBM_{Tol}$ devices. This is possibly due to the addition of 1-methylnaphthalene changing the vertical phase distribution of the P3HT and PCBM. If a greater amount of PCBM is found at the ITO/PEDOT:PSS_{HTL} interface there could be a larger barrier for hole extraction.

Non-halogenated solvents were then compared to DCB in an inverted architecture using ZnO and MoO_x as the electron and hole extracting layer respectively. Since the addition of a small amount of 1-methylnaphthalene to the toluene solution did not appear to improve the solubility, a larger amount (30 vol-%) was tried. Both P3HT:$PCBM_{Tol}$ and P3HT:$PCBM_{TolMeN30\%}$ devices obtained a comparable PCE to devices spin cast from DCB. This highlighted that processing OPV devices in an ambient atmosphere and from more environmentally solvents can obtain comparable efficiency to those using halogenated solvents. However, careful consideration is needed for each fabrication step, as well as the use of appropriate interlayers and device architecture.

In a further step towards fabricating the entire OPV device from solution under ambient atmosphere, the MoO_x hole extracting layer was replaced with a PEDOT:PSS_{Solar} hole transporting layer. Devices utilising the PEDOT:PSS_{Solar} layer displayed a promising device performance, which with further optimisation of the layer could be improved.

5.3 Future work

The work in this thesis presents an additional step towards fully solution processed OPV devices. In order for OPV devices to reach their full potential further efforts investigating alternative low-cost materials and processing conditions needs to be continued.

The majority of the material cost of an OPV device is largely attributed to the ITO electrode. In order to reduce the cost alternative materials have been considered in recent years. The work presented in **Chapter 3** emphasises the viability of using PEDOT:PSS as a replacement with both PEDOT:PSS_{ADD} and PEDOT:PSS_{IMM} electrodes displaying promising device performance. The main difference in device performance was due to an increased J_{sc} for PEDOT:PSS_{IMM} electrodes. The use of secondary Ion Mass Spectrometry (SIMS) could potentially be a useful technique to study any change in phase segregation of the P3HT:PCBM photoactive layer. Although PEDOT:PSS electrodes were seen to result in reasonable overall device performance, the PCE decreased with increasing active area. Combining a PEDOT:PSS electrode with a metal grid could be a way to reduce the increase in R_s.

A methodology for processing the P3HT:PCBM photoactive layer in air was developed in **Chapter 4**. This chapter also highlighted that non-halogenated solvents can be used to spin cast inverted P3HT:PCBM devices with comparable device performance to those using DCB. These both have the potential to further lower the processing costs of OPV devices. A natural step to advance this work further would be to combine the use of PEDOT:PSS as an electrode in inverted devices using non-halogenated solvents. Spray depositing each layer simultaneously

onto multiple substrates would additionally decrease manufacturing time. With some further considerations the ultimate aim of producing low-cost, environmentally friendly, flexible OPV devices that can be fabricated under an ambient atmosphere using a roll-to-roll process could be achievable.

References

1. BP Energy Outlook 2035, www.bp.com.
2. Climate Change 2014: Mitigation of Climate Change, Summary for Policymarkers, www.ipcc.ch.
3. BP Statistical Review of World Energy 2013, www.bp.com.
4. Climate Change 2014: Mitigation of Climate Change, Working Group III, www.ipcc.ch.
5. World Energy Outlook 2013, www.iea.org.
6. N. S. Lewis and D. G. Nocera, *Proceedings of the National Academy of Sciences*, 2006, 103, 15729-15735.
7. 2012 Renewable Energy Data Book, www.nrel.gov.
8. Recent Facts about Photovoltaics in Germany, www.ise.fraunhofer.
9. E. Becquerel, *Comptes Rendus*, 1839, 9, 561-567.
10. R. Ohl, U.S. Patent No. 2402662, 1946.
11. D. M. Chapin, C. S. Fuller and G. L. Pearson, *Journal of Applied Physics*, 1954, 25, 676-677.
12. Vanguard, A History, www.nasa.gov.
13. M. A. Green, K. Emery, Y. Hishikawa, W. Warta and E. D. Dunlop, *Progress in Photovoltaics: Research and Applications*, 2014, 22, 701-710.
14. J. F. Geisz and D. J. Friedman, *Semiconductor Science and Technology*, 2002, 17, 769.
15. T. M. Razykov, C. S. Ferekides, D. Morel, E. Stefanakos, H. S. Ullal and H. M. Upadhyaya, *Solar Energy*, 2011, 85, 1580-1608.
16. http://www.nrel.gov/ncpv/images/efficiency_chart.jpg, 28/07/2014.
17. H. Kallmann and M. Pope, *The Journal of Chemical Physics*, 1959, 30, 585-586.
18. G. A. Chamberlain, *Solar Cells*, 1983, 8, 47-83.
19. C. W. Tang, *Applied Physics Letters*, 1986, 48, 183-185.
20. H. W. Kroto, J. R. Heath, S. C. O'Brien, R. F. Curl and R. E. Smalley, *Nature*, 1985, 318, 162-163.
21. P. Peumans and S. R. Forrest, *Applied Physics Letters*, 2001, 79, 126.
22. N. Beaumont, S. W. Cho, P. Sullivan, D. Newby, K. E. Smith and T. S. Jones, *Advanced Functional Materials*, 2012, 22, 561-566.
23. P. Sullivan and T. S. Jones, *Organic Electronics*, 2008, 9, 656-660.
24. V. Steinmann, N. M. Kronenberg, M. R. Lenze, S. M. Graf, D. Hertel, K. Meerholz, H. Bürckstümmer, E. V. Tulyakova and F. Würthner, *Advanced Energy Materials*, 2011, 1, 888-893.
25. R. F. Bailey-Salzman, B. P. Rand and S. R. Forrest, *Applied Physics Letters*, 2007, 91, 013508.
26. M. Hiramoto, M. Suezaki and M. Yokoyama, *Chemistry Letters*, 1990, 19, 327-330.
27. Heliatek Press Release 16/01/2013, www.heliatek.com.
28. M. Hiramoto, H. Fujiwara and M. Yokoyama, *Applied Physics Letters*, 1991, 58, 1062-1064.

29. M. Hiramoto, H. Fujiwara and M. Yokoyama, *Journal of Applied Physics*, 1992, 72, 3781-3787.
30. G. Yu, J. Gao, J. C. Hummelen, F. Wudl and A. J. Heeger, *Science*, 1995, 270, 1789-1791.
31. J. J. M. Halls, C. A. Walsh, N. C. Greenham, E. A. Marseglia, R. H. Friend, S. C. Moratti and A. B. Holmes, *Nature*, 1995, 376, 498-500.
32. C.-C. Chen, W.-H. Chang, K. Yoshimura, K. Ohya, J. You, J. Gao, Z. Hong and Y. Yang, *Advanced Materials*, 2014, DOI: 10.1002/adma.201402072, n/a-n/a.
33. Mitsubishi Chemical Holdings Achievements, 07/2012, http://www.mitsubishichem-hd.co.jp.
34. C. J. Brabec, M. Heeney, I. McCulloch and J. Nelson, *Chemical Society Reviews*, 2011, 40, 1185-1199.
35. G. P. Nicholson and F. A. Castro, *Nanotechnology*, 2010, 21, 492001.
36. D. M. DeLongchamp, R. J. Kline and A. Herzing, *Energy & Environmental Science*, 2012, 5, 5980-5993.
37. C. Y. Yang and A. J. Heeger, *Synthetic Metals*, 1996, 83, 85-88.
38. J. C. Hummelen, B. W. Knight, F. LePeq, F. Wudl, J. Yao and C. L. Wilkins, *The Journal of Organic Chemistry*, 1995, 60, 532-538.
39. S. E. Shaheen, C. J. Brabec, N. S. Sariciftci, F. Padinger, T. Fromherz and J. C. Hummelen, *Applied Physics Letters*, 2001, 78, 841-843.
40. F. Padinger, R. S. Rittberger and N. S. Sariciftci, *Advanced Functional Materials*, 2003, 13, 85-88.
41. W. Ma, C. Yang, X. Gong, K. Lee and A. J. Heeger, *Advanced Functional Materials*, 2005, 15, 1617-1622.
42. Y. Kim, S. A. Choulis, J. Nelson, D. D. C. Bradley, S. Cook and J. R. Durrant, *J Mater Sci*, 2005, 40, 1371-1376.
43. D. Chirvase, J. Parisi, J. C. Hummelen and V. Dyakonov, *Nanotechnology*, 2004, 15, 1317.
44. M. Reyes-Reyes, K. Kim and D. L. Carroll, *Applied Physics Letters*, 2005, 87, 083506.
45. G. Li, V. Shrotriya, J. Huang, Y. Yao, T. Moriarty, K. Emery and Y. Yang, *Nat Mater*, 2005, 4, 864-868.
46. J. Peet, J. Y. Kim, N. E. Coates, W. L. Ma, D. Moses, A. J. Heeger and G. C. Bazan, *Nature Materials*, 2007, 6, 497.
47. J. K. Lee, W. L. Ma, C. J. Brabec, J. Yuen, J. S. Moon, J. Y. Kim, K. Lee, G. C. Bazan and A. J. Heeger, *Journal of the American Chemical Society*, 2008, 130, 3619-3623.
48. T.-Y. Chu, J. Lu, S. Beaupré, Y. Zhang, J.-R. Pouliot, S. Wakim, J. Zhou, M. Leclerc, Z. Li, J. Ding and Y. Tao, *Journal of the American Chemical Society*, 2011, 133, 4250-4253.
49. P. Atkins, *Shriver and Atkins' Inorganic Chemistry*, OUP Oxford, 2010.
50. P. Peumans, A. Yakimov and S. R. Forrest, *Journal of Applied Physics*, 2003, 93, 3693-3723.
51. P. E. Shaw, A. Ruseckas and I. D. W. Samuel, *Advanced Materials*, 2008, 20, 3516-3520.
52. T. Stübinger and W. Brütting, *Journal of Applied Physics*, 2001, 90, 3632-3641.

53. P. Heremans, D. Cheyns and B. P. Rand, *Accounts of Chemical Research*, 2009, 42, 1740-1747.
54. S. Khodabakhsh, B. M. Sanderson, J. Nelson and T. S. Jones, *Advanced Functional Materials*, 2006, 16, 95-100.
55. I. Hancox, P. Sullivan, K. V. Chauhan, N. Beaumont, L. A. Rochford, R. A. Hatton and T. S. Jones, *Organic Electronics*, 2010, 11, 2019-2025.
56. Y. Kim, A. M. Ballantyne, J. Nelson and D. D. C. Bradley, *Organic Electronics*, 2009, 10, 205-209.
57. M. Sato and H. Morii, *Polymer Communications*, 1991, 32, 42.
58. I. Osaka and R. D. McCullough, *Accounts of Chemical Research*, 2008, 41, 1202-1214.
59. P. J. Brown, D. S. Thomas, A. Köhler, J. S. Wilson, J.-S. Kim, C. M. Ramsdale, H. Sirringhaus and R. H. Friend, *Physical Review B*, 2003, 67, 064203.
60. Y. Kim, S. Cook, S. M. Tuladhar, S. A. Choulis, J. Nelson, J. R. Durrant, D. D. C. Bradley, M. Giles, I. McCulloch, C.-S. Ha and M. Ree, *Nat Mater*, 2006, 5, 197-203.
61. H. Sirringhaus, P. J. Brown, R. H. Friend, M. M. Nielsen, K. Bechgaard, B. M. W. Langeveld-Voss, A. J. H. Spiering, R. A. J. Janssen, E. W. Meijer, P. Herwig and D. M. de Leeuw, *Nature*, 1999, 401, 685-688.
62. H. Sirringhaus, N. Tessler and R. H. Friend, *Science*, 1998, 280, 1741-1744.
63. H. Hoppe and N. S. Sariciftci, *Journal of Materials Research*, 2004, 19, 1924-1945.
64. W. C. Tsoi, S. J. Spencer, L. Yang, A. M. Ballantyne, P. G. Nicholson, A. Turnbull, A. G. Shard, C. E. Murphy, D. D. C. Bradley, J. Nelson and J.-S. Kim, *Macromolecules*, 2011, 44, 2944-2952.
65. H.-L. Yip and A. K. Y. Jen, *Energy & Environmental Science*, 2012, 5, 5994 - 6011.
66. P. Gregory, *Journal of Porphyrins and Phthalocyanines*, 2000, 4, 432-437.
67. G. de la Torre, C. G. Claessens and T. Torres, *Chemical Communications*, 2007, DOI: 10.1039/B614234F, 2000-2015.
68. P. Sullivan, T. S. Jones, A. J. Ferguson and S. Heutz, *Applied Physics Letters*, 2007, 91, 233114.
69. O. Berger, W. J. Fischer, B. Adolphi, S. Tierbach, V. Melev and J. Schreiber, *Journal of Materials Science: Materials in Electronics*, 2000, 11, 331-346.
70. K. L. Mutolo, E. I. Mayo, B. P. Rand, S. R. Forrest and M. E. Thompson, *Journal of the American Chemical Society*, 2006, 128, 8108-8109.
71. S. W. Cho, L. F. J. Piper, A. DeMasi, A. R. H. Preston, K. E. Smith, K. V. Chauhan, P. Sullivan, R. A. Hatton and T. S. Jones, *The Journal of Physical Chemistry C*, 2010, 114, 1928-1933.
72. B. P. Rand, J. Xue, S. Uchida and S. R. Forrest, *Journal of Applied Physics*, 2005, 98, 124902.
73. A. Meller and A. Ossko, *Monatshefte für Chemie*, 1972, 103, 150-155.
74. C. G. Claessens, D. González-Rodríguez and T. Torres, *Chemical Reviews*, 2002, 102, 835-854.
75. A. Hamed, Y. Y. Sun, Y. K. Tao, R. L. Meng and P. H. Hor, *Physical Review B*, 1993, 47, 10873-10880.

76. Y. Kim, M. Shin, I. Lee, H. Kim and S. Heutz, *Applied Physics Letters*, 2008, 92, 093306.
77. M. T. Rispens, A. Meetsma, R. Rittberger, C. J. Brabec, N. S. Sariciftci and J. C. Hummelen, *Chemical Communications*, 2003, DOI: 10.1039/B305988J, 2116-2118.
78. J. Y. Kim, K. Lee, E. C. Nelson, D. Moses, T.-Q. Nguyen, M. Dante and A. J. Heeger, *Science*, 2007, 317, 222-225.
79. B. Azzopardi, C. J. M. Emmott, A. Urbina, F. C. Krebs, J. Mutale and J. Nelson, *Energy & Environmental Science*, 2011, 4, 3741-3753.
80. J. Wu, H. A. Becerril, Z. Bao, Z. Liu, Y. Chen and P. Peumans, *Applied Physics Letters*, 2008, 92, 263302.
81. M. W. Rowell, M. A. Topinka, M. D. McGehee, H.-J. Prall, G. Dennler, N. S. Sariciftci, L. Hu and G. Gruner, *Applied Physics Letters*, 2006, 88, 233506.
82. H. M. Stec and R. A. Hatton, *ACS Applied Materials & Interfaces*, 2012, 4, 6013-6020.
83. T. Aernouts, P. Vanlaeke, W. Geens, J. Poortmans, P. Heremans, S. Borghs, R. Mertens, R. Andriessen and L. Leenders, *Thin Solid Films*, 2004, 451–452, 22-25.
84. D.-S. Leem, A. Edwards, M. Faist, J. Nelson, D. D. C. Bradley and J. C. de Mello, *Advanced Materials*, 2011, 23, 4371-4375.
85. S. Kirchmeyer and K. Reuter, *Journal of Materials Chemistry*, 2005, 15, 2077-2088.
86. A. C. Arias, L. S. Roman, T. Kugler, R. Toniolo, M. S. Meruvia and I. A. Hümmelgen, *Thin Solid Films*, 2000, 371, 201-206.
87. F. Nüesch, L. J. Rothberg, E. W. Forsythe, Q. T. Le and Y. Gao, *Applied Physics Letters*, 1999, 74, 880-882.
88. H. Gommans, B. Verreet, B. P. Rand, R. Muller, J. Poortmans, P. Heremans and J. Genoe, *Advanced Functional Materials*, 2008, 18, 3686-3691.
89. US5300575 (Bayer AG).
90. G. Greczynski, T. Kugler, M. Keil, W. Osikowicz, M. Fahlman and W. R. Salaneck, *Journal of Electron Spectroscopy and Related Phenomena*, 2001, 121, 1-17.
91. J. Hwang, F. Amy and A. Kahn, *Organic Electronics*, 2006, 7, 387-396.
92. A. N. Aleshin, S. R. Williams and A. J. Heeger, *Synthetic Metals*, 1998, 94, 173-177.
93. A. M. Nardes, M. Kemerink, R. A. J. Janssen, J. A. M. Bastiaansen, N. M. M. Kiggen, B. M. W. Langeveld, A. J. J. M. van Breemen and M. M. de Kok, *Advanced Materials*, 2007, 19, 1196-1200.
94. M. P. d. Jong, L. J. v. IJzendoorn and M. J. A. d. Voigt, *Applied Physics Letters*, 2000, 77, 2255-2257.
95. E. Voroshazi, B. Verreet, A. Buri, R. Müller, D. Di Nuzzo and P. Heremans, *Organic Electronics*, 2011, 12, 736-744.
96. J. Y. Kim, J. H. Jung, D. E. Lee and J. Joo, *Synthetic Metals*, 2002, 126, 311-316.
97. J. Ouyang, C. W. Chu, F. C. Chen, Q. Xu and Y. Yang, *Advanced Functional Materials*, 2005, 15, 203-208.

98. X. Crispin, F. L. E. Jakobsson, A. Crispin, P. C. M. Grim, P. Andersson, A. Volodin, C. van Haesendonck, M. Van der Auweraer, W. R. Salaneck and M. Berggren, *Chemistry of Materials*, 2006, 18, 4354-4360.
99. S.-I. Na, G. Wang, S.-S. Kim, T.-W. Kim, S.-H. Oh, B.-K. Yu, T. Lee and D.-Y. Kim, *Journal of Materials Chemistry*, 2009, 19, 9045-9053.
100. I. Cruz-Cruz, M. Reyes-Reyes, M. A. Aguilar-Frutis, A. G. Rodriguez and R. López-Sandoval, *Synthetic Metals*, 2010, 160, 1501-1506.
101. D. J. Lipomi, J. A. Lee, M. Vosgueritchian, B. C. K. Tee, J. A. Bolander and Z. Bao, *Chemistry of Materials*, 2011, 24, 373-382.
102. M. Vosgueritchian, D. J. Lipomi and Z. Bao, *Advanced Functional Materials*, 2012, 22, 421-428.
103. L. A. A. Pettersson, S. Ghosh and O. Inganäs, *Organic Electronics*, 2002, 3, 143-148.
104. A. M. Nardes, M. Kemerink, M. M. de Kok, E. Vinken, K. Maturova and R. A. J. Janssen, *Organic Electronics*, 2008, 9, 727-734.
105. S. K. M. Jönsson, J. Birgerson, X. Crispin, G. Greczynski, W. Osikowicz, A. W. Denier van der Gon, W. R. Salaneck and M. Fahlman, *Synthetic Metals*, 2003, 139, 1-10.
106. S. Timpanaro, M. Kemerink, F. J. Touwslager, M. M. De Kok and S. Schrader, *Chemical Physics Letters*, 2004, 394, 339-343.
107. A. M. Nardes, R. A. J. Janssen and M. Kemerink, *Advanced Functional Materials*, 2008, 18, 865-871.
108. C. Badre, L. Marquant, A. M. Alsayed and L. A. Hough, *Advanced Functional Materials*, 2012, 22, 2723-2727.
109. Y. Xia, K. Sun and J. Ouyang, *Energy & Environmental Science*, 2012, 5, 5325-5332.
110. Y. Xia and J. Ouyang, *Organic Electronics*, 2012, 13, 1785-1792.
111. Y. Xia and J. Ouyang, *Journal of Materials Chemistry*, 2011, 21, 4927-4936.
112. D. Alemu, H.-Y. Wei, K.-C. Ho and C.-W. Chu, *Energy & Environmental Science*, 2012.
113. Y. H. Kim, C. Sachse, M. L. Machala, C. May, L. Müller-Meskamp and K. Leo, *Advanced Functional Materials*, 2011, 21, 1076-1081.
114. Y. H. Kim, C. Sachse, M. Hermenau, K. Fehse, M. Riede, L. Muller-Meskamp and K. Leo, *Applied Physics Letters*, 2011, 99, 113305.
115. N. Kim, B. H. Lee, D. Choi, G. Kim, H. Kim, J.-R. Kim, J. Lee, Y. H. Kahng and K. Lee, *Physical Review Letters*, 2012, 109, 106405.
116. Y. Xia, K. Sun and J. Ouyang, *Advanced Materials*, 2012, 24, 2436-2440.
117. N. Kim, S. Kee, S. H. Lee, B. H. Lee, Y. H. Kahng, Y.-R. Jo, B.-J. Kim and K. Lee, *Advanced Materials*, 2014, 26, 2268-2272.
118. C. Donley, D. Dunphy, D. Paine, C. Carter, K. Nebesny, P. Lee, D. Alloway and N. R. Armstrong, *Langmuir*, 2001, 18, 450-457.
119. Heraeus group, www.heraeus-clevios.com.
120. K. Norrman, A. Ghanbari-Siahkali and N. B. Larsen, *Annual Reports Section "C" (Physical Chemistry)*, 2005, 101, 174-201.
121. F. C. Krebs, *Solar Energy Materials and Solar Cells*, 2009, 93, 394-412.
122. C. Girotto, D. Moia, B. P. Rand and P. Heremans, *Advanced Functional Materials*, 2011, 21, 64-72.

123. R. Green, A. Morfa, A. J. Ferguson, N. Kopidakis, G. Rumbles and S. E. Shaheen, *Applied Physics Letters*, 2008, 92, 033301.
124. G. Susanna, L. Salamandra, T. M. Brown, A. Di Carlo, F. Brunetti and A. Reale, *Solar Energy Materials and Solar Cells*, 2011, 95, 1775-1778.
125. P. Nga Phuong, E. Boellaard, J. N. Burghartz and P. M. Sarro, *Journal of Microelectromechanical Systems*, 2004, 13, 491-499.
126. J. Li, J. Xiao, Y. Huang and H. H. Lou, *AIChE Journal*, 2007, 53, 2841-2857.
127. Iwata, www.iwata-medea.com.
128. A. H. Rice, R. Giridharagopal, S. X. Zheng, F. S. Ohuchi, D. S. Ginger and C. K. Luscombe, *ACS Nano*, 2011, 5, 3132-3140.
129. E. Y. Bormashenko, *Wetting of Real Surfaces*, De Gruyter, Berlin, 2013.
130. D. K. Owens and R. C. Wendt, *Journal of Applied Polymer Science*, 1969, 13, 1741-1747.
131. F. M. Fowkes and M. A. Mostafa, *Industrial & Engineering Chemistry Product Research and Development*, 1978, 17, 3-7.
132. C. J. Van Oss, R. J. Good and M. K. Chaudhury, *Langmuir*, 1988, 4, 884-891.
133. J. D. Servaites, S. Yeganeh, T. J. Marks and M. A. Ratner, *Advanced Functional Materials*, 2010, 20, 97-104.
134. J. D. Servaites, M. A. Ratner and T. J. Marks, *Energy & Environmental Science*, 2011, 4, 4410-4422.
135. G. Greczynski, T. Kugler and W. R. Salaneck, *Thin Solid Films*, 1999, 354, 129-135.
136. T.-W. Lee and Y. Chung, *Advanced Functional Materials*, 2008, 18, 2246-2252.
137. X. Crispin, S. Marciniak, W. Osikowicz, G. Zotti, A. W. D. van der Gon, F. Louwet, M. Fahlman, L. Groenendaal, F. De Schryver and W. R. Salaneck, *Journal of Polymer Science Part B: Polymer Physics*, 2003, 41, 2561-2583.
138. L. S. C. Pingree, B. A. MacLeod and D. S. Ginger, *The Journal of Physical Chemistry C*, 2008, 112, 7922-7927.
139. X.-D. Dang, M. Dante and T.-Q. Nguyen, *Applied Physics Letters*, 2008, 93, 241911.
140. N. K. Unsworth, I. Hancox, C. Argent Dearden, T. Howells, P. Sullivan, R. S. Lilley, J. Sharp and T. S. Jones, *Applied Physics Letters*, 2013, 103, 173304.
141. D. S. Germack, C. K. Chan, B. H. Hamadani, L. J. Richter, D. A. Fischer, D. J. Gundlach and D. M. DeLongchamp, *Applied Physics Letters*, 2009, 94, 233303.
142. C. M. Björström, S. Nilsson, A. Bernasik, A. Budkowski, M. Andersson, K. O. Magnusson and E. Moons, *Applied Surface Science*, 2007, 253, 3906-3912.
143. D. H. K. Pan and W. M. Prest, *Journal of Applied Physics*, 1985, 58, 2861-2870.
144. X. Wang, T. Ederth and O. Inganäs, *Langmuir*, 2006, 22, 9287-9294.
145. Z. Xu, L.-M. Chen, M.-H. Chen, G. Li and Y. Yang, *Applied Physics Letters*, 2009, 95, 013301.

146. J. Ouyang, Q. Xu, C.-W. Chu, Y. Yang, G. Li and J. Shinar, *Polymer*, 2004, 45, 8443-8450.
147. Y. Byung-Kwan, V. Doojin, J. Jang, S.-I. Na, S.-S. Kim, K. Mi-Kyoung and D.-Y. Kim, *Selected Topics in Quantum Electronics, IEEE Journal of*, 2010, 16, 1838-1846.
148. A. K. Pandey, J. M. Nunzi, B. Ratier and A. Moliton, *Physics Letters A*, 2008, 372, 1333-1336.
149. Y. Jun-Seok, Y. Jin-Mun, K. Seok-Soon, K. Dong-Yu, K. Junkyung and N. Seok-In, *Semiconductor Science and Technology*, 2011, 26, 034010.
150. S. Choi, W. J. Potscavage and B. Kippelen, *Journal of Applied Physics*, 2009, 106, 054507.
151. K. Tvingstedt and O. Inganäs, *Advanced Materials*, 2007, 19, 2893-2897.
152. S. Wu, J. Li, Q. Tai and F. Yan, *The Journal of Physical Chemistry C*, 2010, 114, 21873-21877.
153. F. C. Krebs and K. Norrman, *Progress in Photovoltaics: Research and Applications*, 2007, 15, 697-712.
154. V. Chellappan, G. M. Ng, M. J. Tan, W.-P. Goh and F. Zhu, *Applied Physics Letters*, 2009, 95, 263305.
155. J. Schafferhans, A. Baumann, C. Deibel and V. Dyakonov, *Applied Physics Letters*, 2008, 93, 093303.
156. G. Li, Y. Yao, H. Yang, V. Shrotriya, G. Yang and Y. Yang, *Advanced Functional Materials*, 2007, 17, 1636-1644.
157. C. P. Jarrett, K. Pichler, R. Newbould and R. H. Friend, *Synthetic Metals*, 1996, 77, 35-38.
158. A. Tapponnier, I. Biaggio and P. Günter, *Applied Physics Letters*, 2005, 86, 112114.
159. B. A. Mattis, P. C. Chang and V. Subramanian, *Synthetic Metals*, 2006, 156, 1241-1248.
160. A. Guerrero, P. P. Boix, L. F. Marchesi, T. Ripolles-Sanchis, E. C. Pereira and G. Garcia-Belmonte, *Solar Energy Materials and Solar Cells*, 2012, 100, 185-191.
161. I. Hancox, L. A. Rochford, D. Clare, M. Walker, J. J. Mudd, P. Sullivan, S. Schumann, C. F. McConville and T. S. Jones, *The Journal of Physical Chemistry C*, 2012, 117, 49-57.
162. Irfan, H. Ding, Y. Gao, C. Small, D. Y. Kim, J. Subbiah and F. So, *Applied Physics Letters*, 2010, 96, 243307.
163. J. Meyer, A. Shu, M. Kröger and A. Kahn, *Applied Physics Letters*, 2010, 96, 133308.
164. F. C. Krebs, M. Jørgensen, K. Norrman, O. Hagemann, J. Alstrup, T. D. Nielsen, J. Fyenbo, K. Larsen and J. Kristensen, *Solar Energy Materials and Solar Cells*, 2009, 93, 422-441.
165. F. C. Krebs, T. D. Nielsen, J. Fyenbo, M. Wadstrom and M. S. Pedersen, *Energy & Environmental Science*, 2010, 3, 512-525.
166. F. C. Krebs, T. Tromholt and M. Jorgensen, *Nanoscale*, 2010, 2, 873-886.
167. C. Tao, S. Ruan, X. Zhang, G. Xie, L. Shen, X. Kong, W. Dong, C. Liu and W. Chen, *Applied Physics Letters*, 2008, 93, 193307.

168. T. R. Andersen, T. T. Larsen-Olsen, B. Andreasen, A. P. L. Böttiger, J. E. Carlé, M. Helgesen, E. Bundgaard, K. Norrman, J. W. Andreasen, M. Jørgensen and F. C. Krebs, *ACS Nano*, 2011, 5, 4188-4196.
169. I. Burgués-Ceballos, F. Machui, J. Min, T. Ameri, M. M. Voigt, Y. N. Luponosov, S. A. Ponomarenko, P. D. Lacharmoise, M. Campoy-Quiles and C. J. Brabec, *Advanced Functional Materials*, 2014, 24, 1449-1457.
170. C.-C. Chueh, K. Yao, A. Yip, C.-Y. Chang, Y.-X. Xu, K.-S. Chen, C.-Z. Li, F. Huang, Y. Chen, W.-C. Chen and A. K. Y. Jen, *Energy & Environmental Science*, 2013, 6, 3241-3248.
171. H. Hoppe, M. Niggemann, C. Winder, J. Kraut, R. Hiesgen, A. Hinsch, D. Meissner and N. S. Sariciftci, *Advanced Functional Materials*, 2004, 14, 1005-1011.
172. K.-S. Chen, H.-L. Yip, C. W. Schlenker, D. S. Ginger and A. K. Y. Jen, *Organic Electronics*, 2012, 13, 2870-2870.
173. K. N. Semenov, N. A. Charykov, V. A. Keskinov, A. K. Piartman, A. A. Blokhin and A. A. Kopyrin, *Journal of Chemical & Engineering Data*, 2009, 55, 13-36.
174. C.-Z. Li, Y. Matsuo, T. Niinomi, Y. Sato and E. Nakamura, *Chemical Communications*, 2010, 46, 8582-8584.
175. R. S. Ruoff, D. S. Tse, R. Malhotra and D. C. Lorents, *The Journal of Physical Chemistry*, 1993, 97, 3379-3383.
176. M. Glatthaar, M. Riede, N. Keegan, K. Sylvester-Hvid, B. Zimmermann, M. Niggemann, A. Hinsch and A. Gombert, *Solar Energy Materials and Solar Cells*, 2007, 91, 390-393.
177. B. Tremolet de Villers, C. J. Tassone, S. H. Tolbert and B. J. Schwartz, *The Journal of Physical Chemistry C*, 2009, 113, 18978-18982.
178. D. Gupta, M. Bag and K. S. Narayan, *Applied Physics Letters*, 2008, 92, 093301.
179. A. Wagenpfahl, D. Rauh, M. Binder, C. Deibel and V. Dyakonov, *Physical Review B*, 2010, 82, 115306.
180. P. A. Troshin, H. Hoppe, J. Renz, M. Egginger, J. Y. Mayorova, A. E. Goryachev, A. S. Peregudov, R. N. Lyubovskaya, G. Gobsch, N. S. Sariciftci and V. F. Razumov, *Advanced Functional Materials*, 2009, 19, 779-788.
181. B. J. Tremolet de Villers, R. C. I. MacKenzie, J. J. Jasieniak, N. D. Treat and M. L. Chabinyc, *Advanced Energy Materials*, 2014, 4, 1301290.
182. H. Wang, M. Shah, V. Ganesan, M. L. Chabinyc and Y.-L. Loo, *Advanced Energy Materials*, 2012, 2, 1447-1455.
183. V. D. Mihailetchi, H. X. Xie, B. de Boer, L. J. A. Koster and P. W. M. Blom, *Advanced Functional Materials*, 2006, 16, 699-708.
184. K. Vandewal, A. Gadisa, W. D. Oosterbaan, S. Bertho, F. Banishoeib, I. Van Severen, L. Lutsen, T. J. Cleij, D. Vanderzande and J. V. Manca, *Advanced Functional Materials*, 2008, 18, 2064-2070.
185. P. Vanlaeke, A. Swinnen, I. Haeldermans, G. Vanhoyland, T. Aernouts, D. Cheyns, C. Deibel, J. D'Haen, P. Heremans, J. Poortmans and J. V. Manca, *Solar Energy Materials and Solar Cells*, 2006, 90, 2150-2158.
186. S. Wilken, T. Hoffmann, E. von Hauff, H. Borchert and J. Parisi, *Solar Energy Materials and Solar Cells*, 2012, 96, 141-147.

187. D. Baierl, B. Fabel, P. Lugli and G. Scarpa, *Organic Electronics*, 2011, 12, 1669-1673.
188. F. C. Krebs, *Organic Electronics*, 2009, 10, 761-768.